Fermi National Accelerator Laboratory

FERMILAB-FN-627

Beam-beam Interaction Effects in the Fermilab Collider

Donna Marie Siergiej

B.S., Eisenhower College of the Rochester Institute of Technology, 1981
M.S., University of New Mexico, 1986

DISSERTATION

Submitted in Partial Fulfillment of the
Requirements for the Degree of

Doctor of Philosophy in Physics

The University of New Mexico
Albuquerque, New Mexico

March 1995

Operated by Universities Research Association Inc. under Contract No. DE-AC02-76CHO3000 with the United States Department of Energy

Disclaimer

This report was prepared as an account of work sponsored by an agency of the United States Government. Neither the United States Government nor any agency thereof, nor any of their employees, makes any warranty, express or implied, or assumes any legal liability or responsibility for the accuracy, completeness, or usefulness of any information, apparatus, product, or process disclosed, or represents that its use would not infringe privately owned rights. Reference herein to any specific commercial product, process, or service by trade name, trademark, manufacturer, or otherwise, does not necessarily constitute or imply its endorsement, recommendation, or favoring by the United States Government or any agency thereof. The views and opinions of authors expressed herein do not necessarily state or reflect those of the United States Government or any agency thereof.

BEAM-BEAM INTERACTION EFFECTS IN THE FERMILAB COLLIDER

BY

DONNA MARIE SIERGIEJ

B.S., Eisenhower College of the Rochester Institute of Technology, 1981

M.S., University of New Mexico, 1986

DISSERTATION

Submitted in Partial Fulfillment of the
Requirements for the Degree of

Doctor Of Philosophy in Physics

The University of New Mexico
Albuquerque, New Mexico

March 1995

*This work has been supported by Fermi National Accelerator Laboratory under the Joint University-Fermilab Doctoral Program in Accelerator Physics. Fermilab is operated by the Universities Research Association under contract with the United States Department of Energy.

For my parents,
Walter and Eileen Siergiej

ACKNOWLEDGEMENTS

I extend my gratitude to Robert Joshel, whose friendship and encouragement inspired me to complete this work.

I would like to thank the director of Fermi National Accelerator Laboratory, John Peoples, for giving me the opportunity to study beam-beam interaction effects in the Tevatron Collider. I also thank my academic advisor at the University of New Mexico, David Wolfe, for his guidance and support.

In the course of my graduate research program, I have had the fortune of working with three research advisors, each of whom contributed in part to my learning the tools of the trade. I thank Glenn Goderre, Rol Johnson and Edl Schamiloglu for the valuable time I spent working with them. I also thank Glenn Goderre for his comments and suggestions during the writing of this dissertation.

I am grateful to Leo Michelotti and Steve Peggs for helping me gain an understanding of the beam-beam interaction. I would also like to thank Werner Herr for his assistance in developing a beam-beam simulation of the Tevatron during my visit to CERN.

There are many people in the Accelerator Division at Fermilab whom have helped me in a steady manner. Most importantly, I wish to acknowledge the Operations Staff for their selfless help during my beam studies in the Tevatron. I was constantly impressed by their willingness and enthusiasm to work on any projects or problems which would arise. My discussions with Peter Bagley, Jerry Annala, Mike Martens and Norman Gelfand of the Tevatron group always proved helpful. Linda Spentzouris and Francois Ostiguy were both colleagues and friends during my stay at Fermilab, and I thank them for their valuable advice and assistance.

I would especially like to thank David Finley for his active interest in this work and for sharing his methods of scientific inquiry.

BEAM-BEAM INTERACTION EFFECTS IN THE FERMILAB COLLIDER

BY

DONNA MARIE SIERGIEJ

ABSTRACT OF DISSERTATION

Submitted in Partial Fulfillment of the
Requirements for the Degree of

Doctor Of Philosophy in Physics

The University of New Mexico
Albuquerque, New Mexico

March 1995

BEAM-BEAM INTERACTION EFFECTS IN THE FERMILAB COLLIDER

DONNA MARIE SIERGIEJ

Ph.D., Physics, University of New Mexico, 1995

Fermi National Accelerator Laboratory's Collider is the first collider to implement a helical orbit separation scheme for colliding protons and antiprotons. Six antiproton bunches collide head-on with six proton bunches at the two high energy physics detector locations in the ring. The orbits are separated in both the horizontal and vertical planes at all other collision points.

A study of the dependence of the beam-beam interaction on transverse beam separation is presented. Beam-beam experiments in the Collider determined that the beam-beam interaction is the predominant nonlinear force which drives seventh order resonances in the Collider. These odd-ordered resonances were observed to cause large particle losses in the presence of a transverse beam separation or crossing angle at an interaction point. This observation led to a method of "helical orbit tuning" using electrostatic separators and resulted in a 5% increase in the luminosity during Collider Run IA. Independant tuning of beam separation and crossing angle at head-on collision points now provides a luminosity enhancement in routine Collider operations.

Beam-beam experiments were compared with beam-beam simulations to produce an understanding of colliding beam behavior when two particle distributions collide with a transverse beam separation. An experimental measure of particle losses due to resonant excitation at different beam separations showed good agreement with beam-beam simulation results. This comparative agreement extends across a range of beam separations and particle tunes.

This investigation lays a foundation for using beam-beam simulations as a predictive tool for defining minimum beam separation criteria for stable Collider operation.

Contents

1 INTRODUCTION 1

2 PARTICLE MOTION IN AN ACCELERATOR 4

2.1 Relevant Accelerator Physics Parameters 4

2.2 Resonant Motion due to Magnetic Field Errors 18

2.3 The Tevatron as a Collider 21

2.4 Accelerator Parameters during Collider Runs IA and IB 23

3 THE BEAM-BEAM INTERACTION 28

3.1 The Beam-beam Force 28

3.2 A Hamiltonian Analysis 30

The Unperturbed Hamiltonian 32

The Resonant Hamiltonian 33

3.3 The Beam-beam Tune Shift 34

3.4 Amplitude of a Resonance 38

3.5 Beam-beam Simulations 42

4 EXPERIMENTAL METHODS OF MEASUREMENT 47

4.1 Measurement of the Tune 47

4.2 Background Losses 48

4.3 Luminosity 50

4.4 Bunch Intensities and Longitudinal Bunch Length 51

4.5 Transverse Beam Sigma and Beam Emittance 53

The Flying Wires 53
The SVX at CDF 55

5 BEAM-BEAM EXPERIMENTS IN THE TEVATRON 57
5.1 ORBIT CONTROL AT AN INTERACTION POINT 57
Four-Bumps using the Separators 58
Luminosity vs. Separation and Crossing Angle 60
5.2 IDENTIFYING BEAM-BEAM DRIVEN RESONANCES 69
Proton Losses during Tune Scans 71
5.3 INVESTIGATING BEAM-BEAM DRIVEN RESONANCES AS A FUNCTION OF BEAM SEPARATION 74
Collider Run IA - A Beam-beam Experiment and Problems with the Measurement 76
Collider Run IB - Measurement of Particle Losses as a Function of Transverse Beam Separation 78
5.4 COMPARISON WITH A BEAM-BEAM MODEL 85
Definition of a Lost Particle 88
Definition of Maximum % Smear 90
Simulations of a 1x1 Store in the Tevatron 92

6 CONCLUSIONS 109

7 APPENDICES 111

A ORBIT CONTROL OF BEAM SEPARATION AND CROSSING ANGLE AT AN INTERACTION POINT 112

B LUMINOSITY AS A FUNCTION OF SEPARATION AND CROSSING ANGLE 117

C A HISTORICAL REVIEW OF THE USE OF ELECTROSTATIC SEPARATORS IN COLLIDERS 121

BIBLIOGRAPHY 124

List of Tables

2.1 Tevatron Accelerator Parameters in Collider Run IA and IB 24

2.2 Tevatron Lattice Parameters in Collider Run IA and IB 25

5.1 Normalized emittance and longitudinal bunch length used in a calculation of transverse overlap 65

5.2 Comparison of transverse overlap measurements 66

5.3 Measured proton tune in Collider Run IB beam-beam experiment 79

5.4 Bunch intensities in Collider Run IB beam-beam experiment 83

5.5 Resonant tunes in a vertical tune scan simulation 98

A.1 Separator lattice parameters in Collider Run IA 116

List of Figures

2.1 Layout of Fermilab's accelerators 5
2.2 Coordinate system to define a particle's closed orbit. 6
2.3 Phase space transformation of a linear one-dimensional turn-by-turn map 11
2.4 Phase plot of a linear one-dimensional turn-by-turn map with a constant gradient error 14
2.5 Resonance lines in tune space 15
2.6 Horizontal and vertical beta function at the CDF interaction region 22
2.7 Beta wave in a section of the Tevatron in Collider Run IA 26

3.1 Angular deflection due the beam-beam interaction 30
3.2 Horizontal and vertical tune shift due to beam-beam detuning 36
3.3 Beam-beam tune footprint for one head-on collision in the Tevatron Collider 38
3.4 Absolute value of the amplitude of a beam-beam driven resonance for head-on collisions 40
3.5 Amplitude of a beam-beam driven resonance for head-on collisions 40
3.6 Absolute value of the amplitude of a beam-beam driven resonance for a beam separation of 2σ. 41
3.7 Amplitude of a beam-beam driven resonance for a beam separation of 2σ . 41
3.8 Amplitude of a beam-beam driven resonance of $7th$ order for different horizontal separations 42
3.9 Beam-beam simulation calculation of tune shift in the presence of a non-zero horizontal separation 46

4.1 Tune spectrum measured from horizontal Schottky plates in the Tevatron . 47
4.2 A sketch of one half of the CDF detector 49
4.3 Transverse view of a Bunched Beam Counter at CDF. 50

4.4 The Resistive Wall Monitor in the Tevatron. 51
4.5 The Sampled Bunch Display 52
4.6 Sketch of a flying wire assembly. 53
4.7 Flying Wire transverse profiles of a proton and antiproton bunch as measured by the flying wires 54
4.8 The SVX detector at CDF. 56

5.1 Sketch of the location of the separators in the Tevatron 58
5.2 A model's prediction of beam positions in the Tevatron due to a crossing angle bump at B0. 59
5.3 An orbit difference between two measured orbits in the Tevatron: a "four-bump on" minus a "four-bump off" orbit. 59
5.4 A model's prediction of orbit displacements at the BPMs in the Tevatron due to a separation bump at B0 61
5.5 Sketch of the variation of transverse sigma of two colliding bunches in longitudinal space 62
5.6 A MINUIT fit of measured luminosity vs. vertical beam separation at B0 . 63
5.7 A MINUIT fit of measured luminosity vs. horizontal beam separation at B0 64
5.8 Primary vertex data as measured by the SVX at the B0 interaction point . 67
5.9 Three dimensional view of SVX primary vertex data 67
5.10 A MINUIT fit of measured luminosity vs. horizontal crossing angle at B0 68
5.11 Map of experimental tune scans in tune space 70
5.12 Comparison of measured background losses at the B0 and D0 interaction regions during a tune scan 71
5.13 Proton losses measured at B0 while crossing the 5th and 8th order resonances 72
5.14 Proton losses measured at B0 while crossing the 7th order resonance . . . 73
5.15 Background Losses as a function of vertical proton tune for three tune scans during Collider Run IA 75
5.16 Particle losses during a change of tune 77
5.17 Proton tune settings where particle losses were measured during the beam-beam experiment of Collider Run IB 78
5.18 A close-up of Figure 5.17 79

5.19 Antiproton background losses at B0 when the proton tune is near the 7th, 9th and 11th order resonances of Figure 5.18 81
5.20 Proton background losses at B0 when the proton tune is near the 7th, 9th and 11th order resonances of Figure 5.18 82
5.21 Tune diagram marking the measured proton tune settings of the beam-beam experiment and the base tune of particles which are unperturbed by the beam-beam interaction. 83
5.22 Antiproton losses and lifetimes at different beam separations 86
5.23 Proton losses and lifetimes at different beam separations 87
5.24 Effect of different amplitude limits on simulated particle losses in a vertical tune scan 89
5.25 Observed resonances in a simulated vertical tune scan 91
5.26 Effect of the beam-beam interaction on one-dimensional motion in phase space 92
5.27 Maximum horizontal and vertical % smear in a simulated vertical tune scan 93
5.28 Antiproton beam-beam tune footprints of Measurement 1 96
5.29 Antiproton beam-beam tune footprints of Measurement 2 97
5.30 Simulated particle losses for Measurement 1 and Measurement 2 99
5.31 Simulated maximum % smear for Measurement 1 and Measurement 2 . . 100
5.32 Comparison of measured particle losses to simulated particle losses for Measurement 2 101
5.33 Antiproton beam-beam tune footprints of Measurement 3 103
5.34 Simulated particle losses for Measurement 3 104
5.35 Comparison of measured particle losses to simulated particle losses for Measurement 3 105
5.36 Simulated maximum % smear for Measurement 3 107
5.37 Antiproton beam-beam tune footprints of Measurement 4 108

A.1 Schematic of a four-bump 113

B.1 Schematic of two bunches colliding with a crossing angle 120

Chapter 1

INTRODUCTION

The goal of accelerator physics in hadron colliders is to provide a large number of interactions of colliding particles at a large center of mass energy (TeV range). Collisions of particles at such high energies allow high energy physicists to look for interactions which will further their understanding of the strong force and the elementary particles subjected to this force.

The number of interactions per second of two colliding distributions of particles is defined as

$$R = \mathcal{L}\,\sigma_{\text{tot}} \tag{1.1}$$

where $\mathcal{L}$ is the luminosity and σ_{tot} is the total nuclear cross section. The total nuclear cross section is the cross sectional area of collisions, given in units of square cm. Luminosity is the number of interactions per square cm per second.

In order to provide a large number of interactions, an accelerator physicist works at optimizing the luminosity. It will be shown in this work that the luminosity of two colliding particle distributions of equal transverse size is

$$\mathcal{L} = \frac{N_1 N_2 f_{rev}}{4\pi\sigma^2} F(z). \tag{1.2}$$

The particle distributions are assumed to be Gaussian distributions with a standard deviation given by σ. The revolution frequency is f_{rev} and $F(z)$ is a factor taking into account the longitudinal distribution of the bunches. The number of particles in the two colliding distributions are given by N_1 and N_2, respectively.

A particle distribution is confined and accelerated in a synchrotron with an externally

applied RF field, which bunches particles into discrete time-dependent distributions. If there are multiple bunches colliding in an accelerator, the total luminosity is

$$\mathcal{L}_{total} = \mathcal{L}B \tag{1.3}$$

where B denotes the number of bunches.

The beam-beam interaction is the electromagnetic interaction a particle experiences as it travels past an opposing particle distribution. Two colliding bunches in a synchrotron will experience a beam-beam interaction at two points in the ring. Multiple bunches in a synchrotron will increase the number of beam-beam interaction points.

The beam-beam interaction between colliding particles has been a dominant factor in limiting the integrated luminosity in a colliding beam storage ring. Efforts to curb measureable luminosity limitations due to the beam-beam interaction seem to have led quite naturally to an implementation of beam separation schemes in storage rings. Particles of opposite charge were separated in the VEPP-2 electron-positron storage ring at Novosibirsk as early as 1967.[1]

In the first Collider Run (1988-1989) of Fermilab's hadron collider known as the Tevatron, the principle limitation on the luminosity was due to the beam-beam interaction. The Collider had reached its "beam-beam limit"; that is, one could not increase the luminosity by decreasing the beam size or by increasing the number of protons per bunch.[2] In fact, it was necessary to dilute the phase space density of the protons in order to maintain antiproton stability. In order to decrease beam-beam effects at unwanted collision points, a method of separating colliding bunches at certain locations in the ring was developed. This became necessary in order to progress to a higher luminosity.

A helical orbit separation scheme was first implemented in the Collider in Collider Run IA (1992-1993). Six antiproton bunches and six proton bunches were separated at every beam-beam collision point except for the two crossing points at the high energy physics detector locations. Colliding beams moved in helical orbits with beam separation present in both the horizontal and vertical planes. The achievable luminosity of $1.6 \times 10^{30}\text{cm}^{-2}$ sec^{-1} without beam separation increased to luminosities of $5.4 \times 10^{30}\text{cm}^{-2}$ sec^{-1} in routine operations during Collider Run IA.[3]

This dissertation presents a study of the dependence of the beam-beam interaction on transverse beam separation. A method of tuning the helical orbit in order to optimize the luminosity is discussed. Experiments performed in the Tevatron Collider measured particle losses as a function of beam separation. A comparison is made between experimentally

measured losses and the dynamics of a particle's motion in a simulation code which models the beam-beam interaction. Particle losses in a real accelerator are related to losses as defined in the model. The similarities along with the discrepancies between the measurements and the beam-beam simulation are discussed. Observations are made concerning the predictive power of a beam-beam model.

Chapter 2 contains a brief description of relevant accelerator physics parameters used throughout this work. A Hamiltonian analysis of the beam-beam interaction is discussed in Chapter 3, along with an introduction of the beam-beam simulaton code. Chapter 4 describes various devices in the Tevatron which were used as measuring tools in beam-beam experiments. Chapter 5 presents the results of beam-beam experiments in the Tevatron and compares the experimental results to beam-beam simulations. Chapter 6 concludes the beam-beam study with a summary of the results.

Chapter 2

PARTICLE MOTION IN AN ACCELERATOR

A particle accelerator uses combinations of focusing and defocusing magnetic elements to define a stable orbit for accelerating particles. This system of strong focusing is known as an alternating gradient system.[4] Particle motion under the influence of an alternating gradient system in the Tevatron Collider is the subject of this chapter.

A reader's knowledge of accelerator physics terminology is not assumed, so accelerator physics concepts relevant to this work are defined. Section 2.1 provides a brief description of the dynamics of a single particle's motion. The fundamentals of particle motion in the presence of magnetic field errors is discussed in Section 2.2.

This dissertation presents beam-beam experiments performed in Fermilab's Tevatron during a Collider Run (Collider Run IA and Collider Run IB). Section 2.3 is intended to introduce the reader to the Tevatron as it is used during a Collider Run. Section 2.4 lists the operational accelerator physics parameters relevant to the beam-beam experiments.

2.1 RELEVANT ACCELERATOR PHYSICS PARAMETERS

The Fermilab Tevatron has the distinction of being the highest energy collider in existence, currently colliding proton and antiprotons at a center of mass energy of 1800 GeV. The ability to constrain such high energy particles in a 1 km radius ring is due to the bending and focusing capabilities of the superconducting magnets.[5] The Tevatron was the first accelerator to make use of superconducting magnets.[6] All of the dipole, quadrupole and correction magnets are cooled to 4.6 degrees Kelvin, enabling maximum electric current to flow through coils with minimal resistance.

An overview of the Fermilab accelerator complex is shown in Figure 2.1.[7] The Tevatron is divided into six sectors called arcs which are connected by six long straight sections.

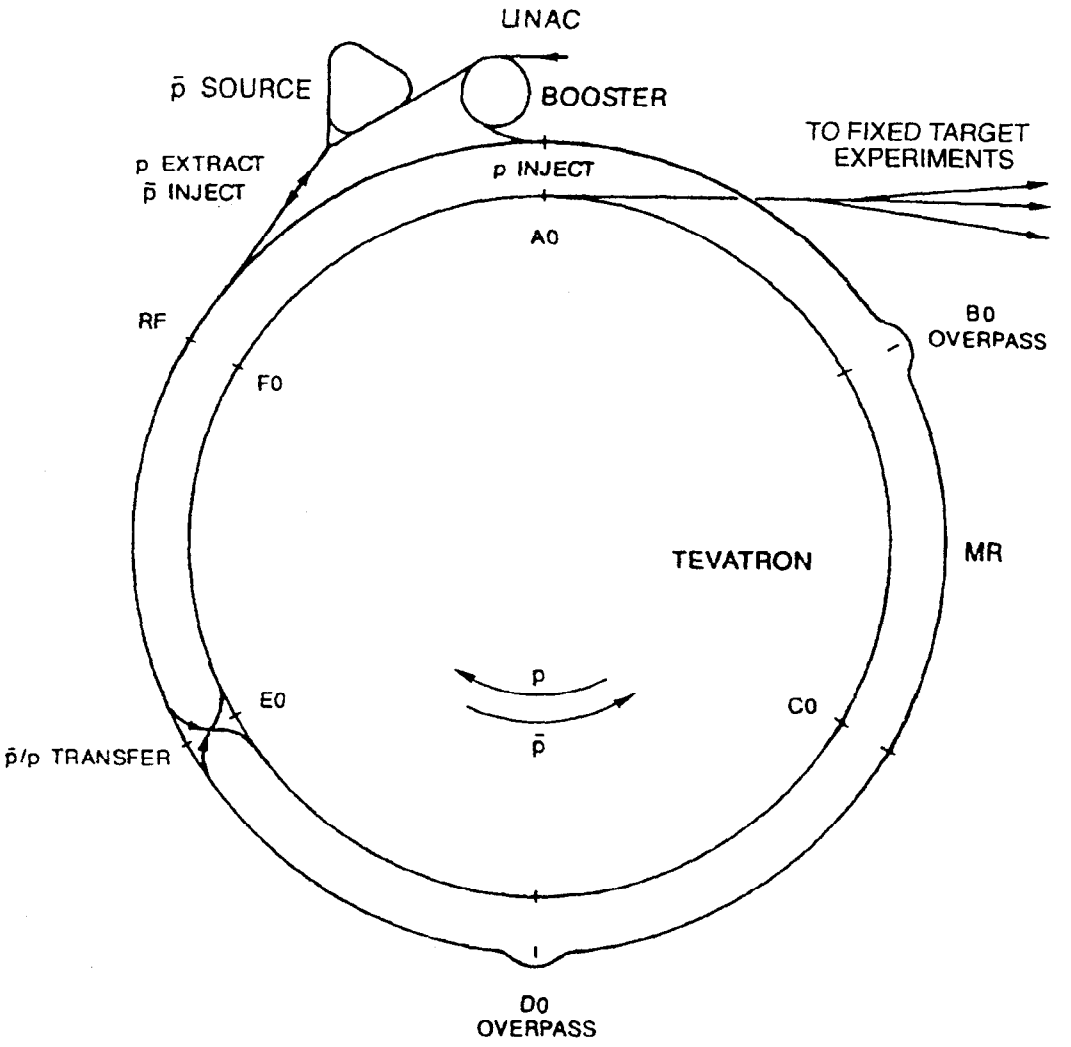

Figure 2.1: Layout of Fermilab's accelerators. The relative size of the accelerators is approximately to scale except that the Tevatron is actually built below the Main Ring. The radius of the Main Ring and Tevatron is 1 km. High energy physics detectors are located at the B0 and D0 straight sections.

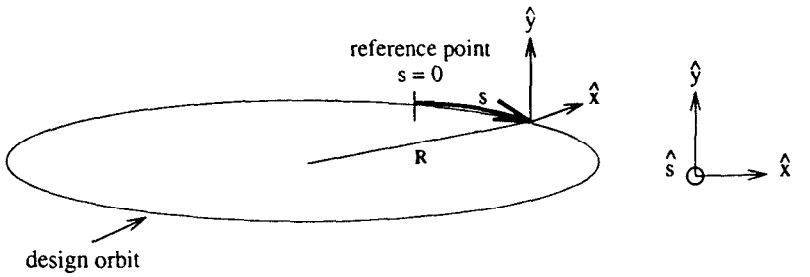

Figure 2.2: Coordinate system to define a particle's closed orbit.

The arcs are composed of a repeating sequence of "cells". The configuration of magnets in a cell is determined by the principles of an alternate-gradient focusing scheme. A typical half-cell in the Tevatron consists of four dipole magnets, a quadrupole and magnetic correction elements. The detailed description of the way in which dipoles, quadrupoles, drift sections and all of the correction elements are placed in the ring is called the accelerator "lattice".

The constant magnetic field of the dipole magnets in the arcs of the Tevatron guides a charged particle along an approximately circular orbit. If the particle travels through the center of the quadrupoles and correction elements, consequently being guided only by the dipole field, the particle's trajectory is said to follow the design orbit of the accelerator. Any particle whose path deviates slightly from the design orbit is focused onto a closed orbit by quadrupole magnets.

It is convenient to define a reference frame to describe a particle's closed orbit as shown in Figure 2.2. The $\hat{x}$ and $\hat{y}$ directions describe the horizontal and vertical deviations of the particle's motion from the design orbit. The $\hat{s}$ direction is the curvilinear coordinate indicating the direction tangential to the particle's forward motion. At high energies, the azimuthal location s is represented in the time domain as $s = ct$, c being the speed of light. The coordinate system is a right-handed coordinate system, so the positive sense of $\hat{x}$ points in the radially outward direction and $\hat{y}$ points in the vertically upward direction.

A quadrupole magnet produces a magnetic field which changes linearly in both transverse dimensions; $B_x = \frac{\partial B_x}{\partial y} y$ and $B_y = \frac{\partial B_y}{\partial x} x$. An approximation which is made in a high energy accelerator is a thin lens approximation: a particle travelling through a quadrupole will experience a negligible change in its position and experience only a small change in the transverse components of its momentum. In this approximation, a particle travelling through a short quadrupole of length L receives a small-amplitude kick which is given by

$$\Delta x' = -\frac{L}{|B\rho|} B_x \qquad \Delta y' = \frac{L}{|B\rho|} B_y. \tag{2.1}$$

The prime denotes a differentiation with respect to the longitudinal coordinate s; $x' \equiv dx/ds$. The constant dipole field guiding the particle in a circular orbit is given by B and the dipole bend radius is ρ. The quantity $|B\rho|$ is the momentum per unit charge of a particle ($|B\rho| = p/e$) and is called the magnetic rigidity. The quadrupole kick is focusing in the horizontal plane and it is defocusing in the vertical plane. It is possible to produce a net focusing system using a sequence of quadrupoles in which a quadrupole which is defocusing in a given plane is followed by a quadrupole which focuses in that plane. Such a system of alternating focusing and defocusing quadrupoles, along with the drift spaces in between the quadrupoles, form the basic elements of an alternating gradient system.[4]

The Lorentz force, $e\vec{v} \times \vec{B}$, describes the motion of a particle in the presence of the dipole magnets, quadrupole magnets and drift sections of a synchrotron. The equation of motion derived from this force is known as Hill's equation. In one dimension, Hill's equation is[4]

$$\frac{\partial^2 x}{\partial s^2} + K(s)x = 0. \tag{2.2}$$

The deviation of a particle's motion from its closed orbit is given by $x(s)$. The quadrupole strength is $K(s)$, where

$$K(s) = \pm\frac{1}{B\rho}B'(s). \tag{2.3}$$

The magnetic field at the azimuthal point s is $B(s)$. The gradient of the quadrupole field, $B' = \partial B_y/\partial x = \partial B_x/\partial y$, is equal in both transverse planes as described by Maxwell's expression for the curl of B in free space, $\nabla \times \vec{B} = 0$. Note that $K(s)$ is zero in a drift section and is also zero in a dipole if one neglects magnetic field errors. In a circular accelerator, the quadrupole strength is periodic with the circumference of the accelerator. It also alternates in sign depending upon whether the quadrupole is focusing or defocusing in a given plane.

In general, K(s) may be taken as a constant for each magnetic element in the ring. At 1 TeV, a standard focusing quadrupole in the Tevatron operates with a magnetic field gradient of 76 T/m, yielding a quadrupole strength of 0.02277 m^{-2}. The linear motion of a particle through each element in the ring can be solved for analytically in Hill's equation if the initial position and angle of the particle are known. Let the initial position and angle of a particle be x_1 and x_1' and its final position and angle after traversing a magnetic element of length L

be x_2 and x_2'. The motion of the particle through the magnetic element is described by

$$\begin{pmatrix} x_2 \\ x_2' \end{pmatrix} = M_{12} \begin{pmatrix} x_1 \\ x_1' \end{pmatrix} \tag{2.4}$$

where M_{12} is a linear transfer matrix. The linear transfer matrices for quadrupoles ($K \neq 0$), drift sections ($K = 0$) and dipoles ($K = 0$) of length L are listed here.

$$K = 0: \quad M_{12} = \begin{pmatrix} 1 & L \\ 0 & 1 \end{pmatrix} \tag{2.5}$$

$$K \neq 0: \quad M_{12} = \begin{pmatrix} \cos(L\sqrt{K}) & \frac{1}{\sqrt{K}}\sin(L\sqrt{K}) \\ -\sqrt{K}\sin(L\sqrt{K}) & \cos(L\sqrt{K}) \end{pmatrix} \tag{2.6}$$

The focusing scheme used in accelerators is comparable to a combination of thin lenses in an optical system. In other words, the length of a quadrupole is much smaller than its focal length. Using the thin lens approximation, the length of the quadrupole in the linear transfer matrix of Equation 2.6 is assumed to go to zero as the quantity $\sqrt{K}\ L$ remains finite. The transfer matrix of a focusing quadrupole under the thin lens approximation is

$$M_{12} = \begin{pmatrix} 1 & 0 \\ -\frac{1}{f} & 1 \end{pmatrix}, \tag{2.7}$$

where $f = (KL)^{-1}$. The transfer matrix of a focusing quadrupole is none other than that of a thin optical focusing lens with focal length f. As shown previously, the same quadrupole will be defocusing in the other transverse plane of motion. A defocusing transfer matrix is equivalent to the focusing transfer matrix described above with the sign of f reversed, corresponding to a thin defocusing lens in an optical system. A standard quadrupole of length 1.678 meters in the Tevatron has a focal length of 26.1 meters. Thus the longitudinal distance between focusing and defocusing quadrupoles in the Tevatron is approximately 26 meters to provide net focusing in both transverse planes of motion.

Accelerator Lattice Parameters

If a particle traverses a series of n elements having transfer matrices M_1,M_2,M_3 up to M_n, the motion through the elements is described by a single linear transfer matrix:

$$M_{12} = M_1 M_2 M_3 .... M_n. \tag{2.8}$$

This method of solution is useful in the design of a ring, but it is cumbersome to use in describing the general nature of particle trajectories. A much more convenient solution of Hill's equation is given by the general solution for x(s):

$$x(s) = A\sqrt{\beta(s)}\cos\left(\psi(s) + \delta\right). \tag{2.9}$$

The functions $\beta(s)$ and $\psi(s)$ are predetermined functions of s while A and δ are constants which determine a particular particle trajectory. Note that Hill's equation is the equation of motion of a harmonic oscillator with a periodic spring constant which depends upon distance. As would be expected, its solution resembles that of a harmonic oscillator except that the amplitude of oscillation is no longer constant but varies with distance.

A better understanding of the beta function, $\beta(s)$, and the phase advance of a particle, $\psi(s)$, is obtained by substituting x(s) into Hill's equation. Two differential equations become apparent,

$$\frac{\partial}{\partial s}(\beta\psi') = 0, \tag{2.10}$$

and

$$2\beta''\beta - (\beta')^2 - 4\beta^2(\psi')^2 + 4\beta^2 K(s) = 0. \tag{2.11}$$

As Equation 2.11 indicates, if the focusing strength $K(s)$ is known, a solution for the beta function, $\beta(s)$, is found numerically. The beta function thus represents an alternative description of the magnetic focusing structure of the accelerator. It is a powerful representation in that it bypasses the necessity to always map a particle through all of the individual magnetic elements in the ring. The focusing properties of the entire ring are represented by the beta function in each transverse plane.

Equation 2.10 gives the phase advance of a particle's motion. A particle's phase advance from a location s_1 in the ring to a location s_2 is

$$\Delta\psi = \int_{s_1}^{s_2} \frac{ds}{\beta(s)}. \tag{2.12}$$

The phase advance of a particle does not change with a constant frequency like that of a harmonic oscillator. It increases as a function of the beta function or, equivalently, as a function of quadrupole strengths. The phase advance of a particle is defined in both the horizontal and vertical planes. In a given transverse plane, the beta function in the arcs of the Tevatron is approximately 100 meters at the location of a focusing quadrupole and is approximately

30 meters at the location of a defocusing quadrupole. A particle's horizontal phase advances more rapidly at the location of a defocusing quadrupole.

The parameters $\beta(s)$ and $\psi(s)$ are conventionally called accelerator lattice parameters or Twiss parameters. Twiss parameters were used by Courant and Snyder to define a linear transfer matrix which mapped a particle's motion through any number of magnetic elements in an accelerator.[4] This linear transfer matrix represents a particle's complete traversal in one plane from a location s_1 to a location s_2. As in Equation 2.8, the transfer matrix is given by

$$M_{12} = \begin{pmatrix} \sqrt{\frac{\beta_2}{\beta_1}}(\cos\Delta\psi + \alpha_1 \sin\Delta\psi) & \sqrt{\beta_2\beta_1}\sin\Delta\psi \\ -\frac{1+\alpha_1\alpha_2}{\sqrt{\beta_1\beta_2}}\sin\Delta\psi + \frac{\alpha_1-\alpha_2}{\sqrt{\beta_1\beta_2}}\cos\Delta\psi & \sqrt{\frac{\beta_1}{\beta_2}}(\cos\Delta\psi - \alpha_2\sin\Delta\psi) \end{pmatrix}. \tag{2.13}$$

The parameter $\alpha(s) = -\frac{1}{2}(\partial\beta/\partial s)$ is an accelerator lattice parameter which describes the slope of the beta function.

The Tune of a Particle

The periodicity of the beta function with the circumference of the ring dictates that a particle will advance in phase by the same amount upon each revolution of the ring. This quantity is written as $2\pi Q$, where

$$Q = \frac{1}{2\pi}\oint \frac{1}{\beta(s)} ds. \tag{2.14}$$

The parameter Q is known as a particle's tune. The complete integral signifies that the integration is over one complete revolution of the ring. Inasmuch as the beta function is defined in two transverse planes, the tune of a particle is defined in two transverse planes. A particle's tune is an important quantity in accelerator physics and particularly in this work, so it will be discussed in some detail in this chapter and in later chapters.

Consider observing a particle's motion at only one azimuthal location in the ring. A particle's position and phase at one observation point can be mapped in terms of an integer turn number by equating the turn number t with the azimuthal coordinate s as $t \equiv s/2\pi R$. A particle's trajectory from turn $t-1$ to turn t is described by

$$\begin{pmatrix} x_2 \\ x_2' \end{pmatrix}_t = M \begin{pmatrix} x_1 \\ x_1' \end{pmatrix}_{t-1}. \tag{2.15}$$

The phase advance of a particle from turn $t-1$ to turn t is $\Delta\psi = 2\pi Q$. Referring to Equation 2.13, the one-turn transfer matrix M is constructed;

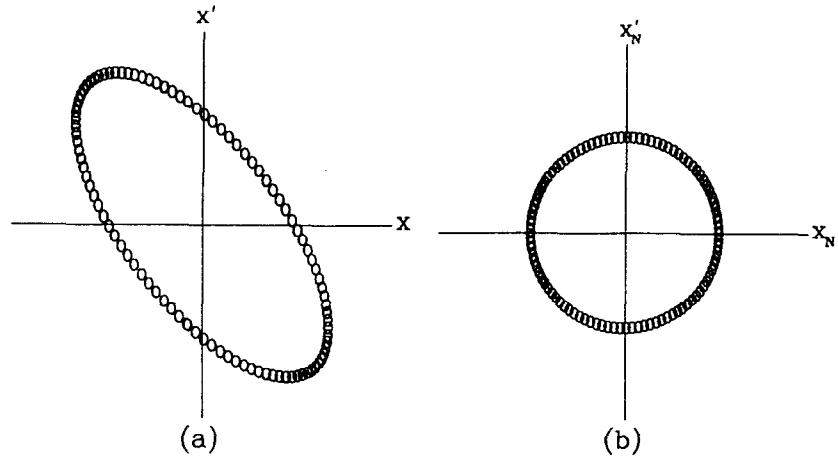

Figure 2.3: The phase space transformation of 100 turns of a linear one-dimensional turn-by-turn map from (x, x') coordinates to normalized (x_N, x'_N) coordinates.

$$M = \begin{pmatrix} \cos 2\pi Q + \alpha \sin 2\pi Q & \beta \sin 2\pi Q \\ -\frac{1+\alpha^2}{\beta} \sin 2\pi Q & \cos 2\pi Q - \alpha \sin 2\pi Q \end{pmatrix}. \tag{2.16}$$

The lattice parameters α and β are calculated using knowledge of the one-turn map, M.

Transverse Beam Emittance

A plot of a particle's position and phase at one location in the ring over the course of many turns is shown in Figure 2.3a. The particle's trajectory maps out an ellipse in the phase space coordinates (x, x'). The area of the ellipse is equal to πA^2, where A is a constant. This area is a constant of the motion, similar to the total energy of a harmonic oscillator. After calculating the derivative of x(s) with respect to s using Equation 2.9, the constant of the motion is found to satisfy

$$\frac{x^2 + (\beta x' + \alpha x)^2}{\beta} = A^2. \tag{2.17}$$

This equation points to a useful transformation from the (x, x') coordinate system to a normalized coordinate system (x_N, x'_N), where

$$\begin{aligned} x_N &= \frac{1}{\sqrt{\beta}} x \\ x'_N &= \frac{\alpha}{\sqrt{\beta}} x + \sqrt{\beta} x'. \end{aligned} \tag{2.18}$$

Since β and x are in units of meters, the normalized coordinates are in units of square root of a meter. This transformation is referred to as a Courant-Snyder transformation.[4] It is

based on the Floquet theory which ensures the existence of a periodic coordinate system which removes time dependence from the linear system.[8] By making this transformation, M now becomes a simple rotation matrix. As shown in Figure 2.3b, the motion of a particle over many turns traces out a circle in normalized phase space coordinates. Just as in the elliptical mapping, the area of the circle in phase space remains constant and equal to πA^2. In accelerator physics, this constant of the motion is known as the transverse emittance of a single particle.

Formally, transverse beam emittance is defined in terms of a distribution of particles. Transverse beam emittance is defined as the area of phase space in which a prescribed fraction of particles reside. With a measurement of the beam distribution in physical space at one location in the ring, the emittance enables calculation of the beam size at other azimuthal locations.

In the Tevatron, a valid approximation is to assume that a particle distribution in both the transverse and longitudinal dimensions is a Gaussian distribution, that is,

$$N(x) = \frac{N_0}{\sqrt{2\pi\sigma}}\, e^{-\frac{x^2}{2\sigma^2}} \tag{2.19}$$

in one dimension. The parameter $N(x)$ denotes the number of particles at a transverse position x. The total number of particles in the distribution is N_0. The rms beam size in physical space is given by σ. The beam emittance, ϵ, for a Gaussian distribution is

$$\epsilon = -\frac{2\pi\sigma^2}{\beta}\ln(1-f), \tag{2.20}$$

where the beta function and σ are defined at the same azimuthal location.[16] The units of emittance are *mm-mrad*. The fraction of particles contained within a given beam emittance is f. Determination of the fraction of particles to include in a definition of a beam size is somewhat arbitrary, hence different accelerator organizations choose different values of f. Fermilab chooses to include 95% of the particle distribution in phase space, yielding a beam emittance of

$$\epsilon = \frac{6\pi\sigma^2}{\beta}. \tag{2.21}$$

Since beam emittance is a constant of the motion, the value of σ^2/β remains constant in each transverse plane of motion around the entire ring. Thus, as Equation 2.9 indicates, an appropriately scaled beta function represents an envelope of the physical boundary that a beam distribution may encompass as it traverses the ring.

Beam emittance as defined above may not remain constant as the energy of the beam changes though. Liouville's theorem defines the phase space area which remains invariant over all particle energies.[11] In order to define this invariant, a transformation from (x, x') coordinates to the conjugate variables (x, p_x) is required. The variable p_x is the transverse component of the particle's momentum defined in one degree of freedom. The phase space area in terms of (x, p_x) coordinates is

$$\oint dp_x dx = mc\,(\gamma\beta)_{rel} \oint dx' dx = mc\,(\gamma\beta)_{rel}\,\epsilon. \tag{2.22}$$

Normalized emittance is given by

$$\epsilon_N = \frac{1}{mc} \oint dp_x dx = (\beta\gamma)_{rel}\,\epsilon. \tag{2.23}$$

Note that the subscript notation on the parameters β and γ indicate that these quantities are not accelerator lattice parameters. They are the familiar relativistic parameters; $\beta = v/c$ and $\gamma = 1/(1-\beta^2)$. The particle's rest mass is denoted by m. As defined above, normalized emittance is invariant over all particle energies. It is a measuring tool which is used very often to determine if the accelerator is running properly over its entire energy range.

Constraints on a Particle's Tune

The magnetic field in a magnetic element can be expressed as a series of multipole terms: the coefficient of the second order term ($n = 2$) represents the quadrupole field component, the coefficient of the third order term ($n = 3$) represents the sextupole field component of the magnetic field, and so forth (see Section 2.2). Upon passing through a magnetic element, a particle will experience a kick every revolution of the ring due to the sum of all field components in the magnetic element.

Consider the motion of a particle in one dimension with a tune satisfying the relation $nQ = p$, where n and p are integers. If $n = 2$ and the particle's tune is a half-integer value, the kick will add in phase and the particle's tune is on resonance. Similarly, if $n = 3$ and the particle's tune is a third integer value, a resonant condition exists. This argument extends to higher order magnetic field components as well. A resonant condition is equivalent to adding constant vectors parallel to the x'_N axis of phase space as shown in Figure 2.4. A particle's phase space history in the presence of a constant kick at a single location is mapped for a tune which is an odd multiple of one-half. The kick in x' in Figure 2.4a translates into a growth in x at a downstream location as seen in Figure 2.4b.

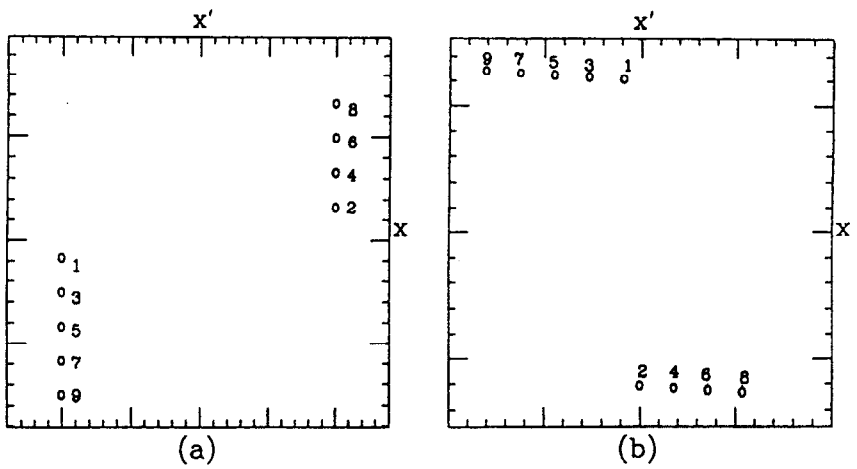

Figure 2.4: Phase plot of a linear one-dimensional turn-by-turn map of 9 turns with a constant kick in x' at one location. The particle's tune is near the half-integer. Figure a is the phase plot at the location of the kick. Figure b is the phase plot at a location $\pi/2$ downstream of the kick location. The turn number is labelled at each point in phase space.

After many turns, even a small kick in x' will cause growth in a particle's amplitude at a downstream location and will eventually lead to the loss of the particle. This resonance condition is defined in two transverse dimensions as

$$n_x Q_x \pm n_y Q_y = p. \tag{2.24}$$

The order of the resonance is given by summing the constants $|n_x| + |n_y|$. The integer p is the azimuthal frequency which drives the resonance.[12]

A plot of resonance lines satisfying Equation 2.24 is shown in Figure 2.5. The solid lines represent sum resonances and satisfy Equation 2.24 when both n_x and n_y are positive. The dashed lines represent difference resonances and satisfy Equation 2.24 when either n_x or n_y are negative.

If all resonance lines which satisfied Equation 2.24 were drawn in tune space, a countably infinite number of lines would fill the plot. It will be demonstrated in this work that only lower order resonance effects in the Tevatron are important to avoid. Consequently, only resonance lines up to twelfth order are drawn. The fractional tune used as a nominal operating point in the Tevatron Collider is marked in the tune plot. The horizontal and vertical operating tunes are amidst the region of 12th order resonances and are bordered by 5th and 7th order resonances.

The expression relating a magnetic field gradient error in an accelerator to the shift in

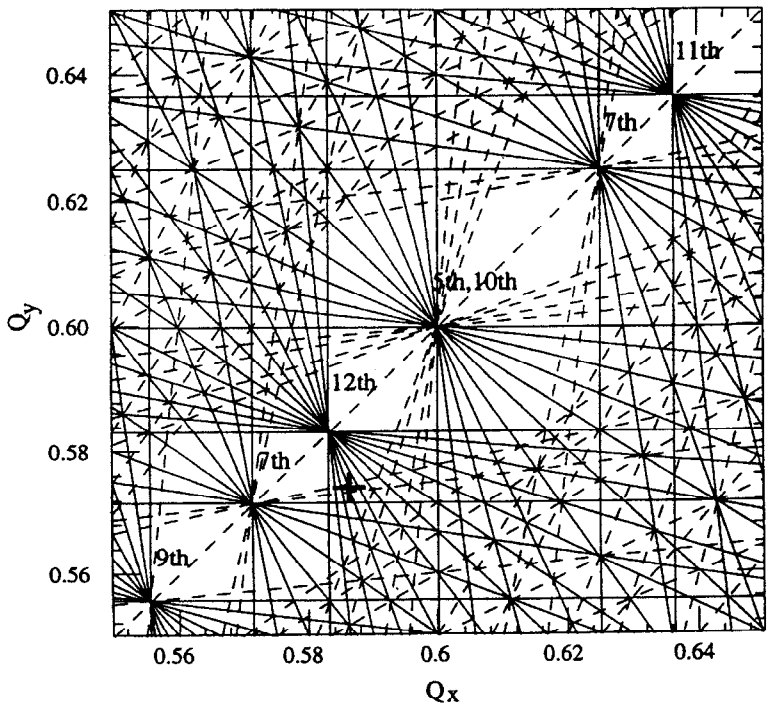

Figure 2.5: Resonance lines in tune space. Solid and dashed lines denote sum and difference resonances, respectively. Regions are labelled by the order of the sum resonances. The operating point of the Tevatron is indicated by the cross mark.

a particle's tune is found by comparing the one turn transfer matrix which includes a small gradient error to the transfer matrix of equation 2.16. The gradient error is expressed as the inverse focal length of a thin quadrupole; $q = \frac{1}{f} = KL$. The shift in a particle's tune due to a magnetic field gradient error q is

$$\Delta Q = \frac{1}{4\pi}\beta q, \tag{2.25}$$

where β is the beta function at the location of the gradient error.

In order to control the tune shift of particles due to random gradient errors in standard quadrupoles of the lattice, correction quadrupoles are added at a location close to the standard quadrupoles. The correction quadrupoles are capable of varying the tune of the Tevatron by ± 1 tune unit at 900 GeV to keep a particle distribution in a "resonance-free" region of tune space.

Thus far, single particle motion in a synchrotron has been discussed for particle trajectories with a design energy specified by the magnitudes of the design magnetic fields. However, particle distributions in a synchrotron do not all have the design energy. If a particle is injected into the accelerator with an energy which does not match the accelerator's design energy, for example, a particle's energy will oscillate about the design energy. These energy oscillations, referred to as synchrotron oscillations, will couple into the particle's transverse motion through dispersion. Off momentum particles will no longer pass axially through the center of a quadrupole and consequently be subject to a focusing force. The closed orbit will thus be displaced from the central design orbit.[11] A particle's transverse position with a momentum offset is given by

$$x(s) = x_\beta(s) + \eta(s)\frac{\Delta p}{p_0}. \tag{2.26}$$

The free betatron oscillations of Equation 2.9 are denoted by $x_\beta(s)$. The momentum offset, Δp, is the measured deviation of the particle's momentum from the design momentum, p_0. The parameter $\eta(s)$ is called the dispersion and is in units of meters. Since orbits of higher momentum are usually at a larger radius in a high energy accelerator (when a particle's energy is above transition energy), the dispersion function is usually a positive function. In an accelerator which bends horizontally and thus lies in the horizontal plane, path length deviations from the design will occur horizontally. The dispersion function, therefore, is generally a non-zero function only in the horizontal plane. In the Tevatron, the horizontal dispersion in the arcs ranges from 2 to 6 meters. The rms momentum spread of a bunch distribution at 900 GeV is typically $\frac{\sigma_p}{p} = 0.0001$.

The dispersion $\eta(s)$ and the slope of the dispersion $\eta'(s) = \partial\eta(s)/\partial s$ are both Twiss parameters. Along with $\beta(s)$, $\alpha(s)$, and $\psi(s)$, they define a complete set of accelerator lattice parameters used to map a particle's linear motion in a synchrotron.

Given the dispersion and beta function at a specific location in the ring, the rms transverse size of a bunch distribution of emittance ϵ and momentum spread σ_p/p is completely defined. An unnormalized beam emittance defined at 1σ ($f = 0.15$ in Equation 2.20) gives an rms transverse beam size of

$$\sigma_i(s) = \sqrt{\beta_i(s)\ \epsilon_i + \left(\eta_i(s)\frac{\sigma_p}{p}\right)^2}. \tag{2.27}$$

The index i is used to emphasize the parameters which are defined in both transverse planes;

$i \equiv \hat{x}, \hat{y}$. Using the Fermilab definition of beam emittance (Equation 2.21), the rms transverse beam size in terms of normalized beam emittance is

$$\sigma_i(s) = \sqrt{\frac{\beta_i(s)\ \epsilon_{Ni}}{6\pi(\beta\gamma)_{rel}} + \left(\eta_i(s)\frac{\sigma_p}{p}\right)^2}. \tag{2.28}$$

Consider the variation of the rms transverse beam size in the arcs of the Tevatron at 900 GeV for a beam with a normalized emittance of 20π mm-mrad. A beta of 100 m and a dispersion of 6 m corresponds to a σ of 0.67 mm. A beta of 30 m and a dispersion of 2 m corresponds to a σ of 0.37 mm. A particle at 3σ in a particle distribution would occupy up to 2 mm in both transverse dimensions, or approximately 3 square mm in transverse space.

Because a spread of momentum exists in a particle distribution, particles will traverse a quadrupole magnet at different transverse positions. Consider a particle with its momentum expressed in terms of the design momentum and a momentum offset as $p = p_0(1 + \frac{\Delta p}{p_0})$. Upon traversing a focusing quadrupole of length L, the particle will see a change in the focal length of the quadrupole. The focal length of a quadrupole was previously found to be proportional to a particle's momentum; $f = p/(eB'L)$. By substituting the new momentum of the particle into this focal length expression, the change in focal length is found to be

$$\Delta f = \left(\frac{B\rho}{B'L}\right)\frac{\Delta p}{p}. \tag{2.29}$$

A positive momentum offset corresponds to a larger focal length. A particle with a positive momentum offset will thus be focused less than a particle at the design momentum. This leads to a chromatic focusing effect on a distribution of particles similar to chromatic effects seen in optical systems. A parameter called the chromaticity, ξ, is used to relate a particle's momentum offset to a corresponding change in its tune;

$$\Delta Q = \xi\ \frac{\Delta p}{p_0}. \tag{2.30}$$

The chromaticity is defined in each transverse plane of motion. By using the expression for the tune shift due to a quadrupole kick as described by Equation 2.25, the chromaticity is formally defined as

$$\xi = -\frac{1}{4\pi}\oint \beta(s)K(s)ds, \tag{2.31}$$

where $K(s)$ is the focusing strength of the lattice quadrupoles.[11] The natural chromaticity is the chromaticity of a synchrotron with no correction elements added to the lattice. The

natural chromaticity is approximately equal in magnitude and opposite in sign to the tune of the synchrotron.

Given a momentum spread in a particle distribution, a large chromaticity may cause a tune spread which is large enough that some of the particles have tunes that lie on or near undesirable resonances. To compensate for this effect, sextupole magnets are added as correction elements in the lattice. The magnetic field in a sextupole is quadratic in position; $B_x = \frac{1}{2}B_x^{'}y^2$ and $B_y = \frac{1}{2}B_y^{'}x^2$. Sextupole magnets, therefore, provide a field gradient which is linearly proportional to a particle's position offset. Using Equation 2.31, the contribution to the chromaticity from N sextupoles in the accelerator ring is

$$\xi_x = \frac{1}{2\pi}\sum_{i=1}^{N}\beta_x(s_i)\eta_x(s_i)k_x(s_i) \qquad \xi_y = \frac{1}{2\pi}\sum_{i=1}^{N}\beta_y(s_i)\eta_x(s_i)k_y(s_i) \tag{2.32}$$

where $k(s) = B^{''}(s)L/B\rho$. The natural chromaticity is thus corrected for with the addition of sextupoles at high dispersion points in the ring. Note, however, that along with the beneficial contribution to the chromaticity, sextupoles do add nonlinearities to the lattice which must be accounted for to ensure stable running conditions.

2.2 Resonant Motion due to Magnetic Field Errors

Magnetic field errors arise from many sources in a real accelerator. There may be small magnet-to-magnet variations in the magnetic field produced even when the electric currents are the same in all magnets. Even if the magnetic field is within the design specifications, a magnet may be misaligned from its design position. This misalignment may occur in its transverse placement in the ring causing the particle to see field errors in normal components of the magnetic field. The misalignment may also manifest itself as a slight rotation of the magnet causing the particle to interact with skew components of the magnetic field. Magnetic fields along with field errors in a magnet are fully expressed as a fraction of the dipole bending field B_0 by[14],[13]

$$iB_x(x,y) + B_y(x,y) = B_0\sum_{n=0}^{\infty}(b_n + ia_n)(x+iy)^n. \tag{2.33}$$

The constants b_n and a_n are the multipole coefficients of the magnetic field.

Suppose that there is a constant magnetic field error in either a dipole or quadrupole which is located at $s = 0$. As discussed in Section 2.1 of this chapter, a particle's trajectory will be a free betatron oscillation about the unperturbed closed orbit. When the particle arrives at $s = 0$, the slope of its trajectory will change by an amount $\Delta\theta$. To constrain the

particle's motion to a new closed orbit, the trajectory of the orbit must close upon itself after one revolution.

$$x_c(s + 2\pi R) = x_c(s) \tag{2.34}$$

This constraint allows a closed orbit position to be calculated:

$$x_c(s) = \frac{\Delta\theta\sqrt{\beta(s)\beta_0}}{2\sin\pi Q}\cos(\Delta\psi - \pi Q) \tag{2.35}$$

where $0 < \Delta\psi < 2\pi$ and β_0 is the beta function at the location of the field error.[15] The displacement of the orbit is directly proportional to the magnitude of $\Delta\theta$ and the beta function at the location of the error. A resonant condition due to the field error is seen in the denominator of the closed orbit expression. As the tune approaches an integer, the amplitude of the oscillation will become large. This condition to be avoided is known as an integer resonance condition.

For completeness, let the transverse position of a particle be written explicitly as the sum of free betatron oscillations, energy oscillations and oscillations due to closed orbit errors. A subscript notation is used to denote $x_\beta(s)$ as the free oscillations of Equation 2.9 about the closed orbit given by Equation 2.35. The position $x_d(s)$ denotes the change in position due to dispersion effects as described in Equation 2.26. Beam position monitors in the accelerator will thus measure orbit positions which include all of these effects:

$$x(s) = x_\beta(s) + x_d(s) + x_c(s). \tag{2.36}$$

If a field error exists which is a quadrupole field error, the beta function in the accelerator will change. The deviation of the beta function from the beta function of the lattice design which is free from magnetic field errors is commonly referred to as a beta wave. The results of the derivation of a beta wave due to a small gradient error in a quadrupole is[15]

$$\frac{\Delta\beta(s)}{\beta(s)} = \frac{1}{2\sin 2\pi Q}\oint q(s')\beta(s')\cos 2(\Delta\psi - \pi Q)ds'. \tag{2.37}$$

The beta function of the real lattice normalized to the beta function of the design lattice is denoted by $\frac{\Delta\beta}{\beta}$. The parameter $q(s)$ is the quadrupole strength associated with the kick of magnitude $\Delta\theta$ a particle sees at a transverse position x: $qx = \Delta\theta$. Note that the denominator of the beta wave indicates a new set of resonances which must be avoided when quadrupole field errors are present. Half-integer values of the tune correspond to a beta wave of infinite magnitude. Along with an integer resonance, therefore, operating close to a half-integer resonance in an accelerator is a particularly dangerous condition. Regardless of whether

the particles are initially at a high oscillation amplitude or are in the core of the distribution, particles will grow in amplitude without bound and eventually be lost.

In general, if a magnetic field error exists in an accelerator, the transverse equation of motion of a particle becomes inhomogeneous:

$$\frac{\partial^2 x}{\partial s^2} + K(s)x = g(x,s). \tag{2.38}$$

The driving function, $g(x,s)$, is a force term which may be a nonlinear function of amplitude x and azimuth s.

A Courant-Snyder coordinate transformation into the normalized coordinates of Equation 2.18 along with a phase transformation will enable this inhomogenous Hill's equation to be expressed as the equation of motion of a driven harmonic oscillator. By reducing the phase $\psi(s)$ by Q such that $\phi(s) = \frac{1}{Q}\,\psi(s)$, the equation of motion becomes

$$\frac{\partial^2 x_N}{\partial \phi^2} + Q^2 x_N = -Q^2\,\beta^{\frac{3}{2}}(\phi)\,g(x_N,\phi). \tag{2.39}$$

The phase ϕ now advances by 2π after each turn. In the (x_N,ϕ) coordinates, the mathematical methods used to describe the motion of a driven harmonic oscillator become available. The notion of a resonance between a particle's tune and a harmonic amplitude of the driving term is the same as that of a simple harmonic oscillator.

The driving force is expressed in terms of m multipole moments of the dipole field error using Equation 2.33. A magnetic field expressed in terms of normal multipoles (assuming skew multipoles terms are equal to zero) in one dimension is given by

$$g(x_N,\phi) = \frac{\Delta B}{(B\rho)} = \frac{1}{(B\rho)}[\beta^{\frac{3}{2}}\,b_0 + \beta^{\frac{4}{2}}\,b_1 x_N + \beta^{\frac{5}{2}}\,b_2 x_N^2 + ... + \beta^{\frac{(m+3)}{2}}\,b_m x_N^m]. \tag{2.40}$$

The first, second and third terms denote the dipole, quadrupole and sextupole moments of the field error ΔB, respectively. In general, the mth term denotes the mth order multipole moment of the field error. Each multipole moment can drive a particle into resonance if the resonant frequency of the driving term equals that of the frequency of the solution to the homogeneous Hill's equation;

$$x_N(\phi) = A\cos(Q\phi + \delta). \tag{2.41}$$

Consider, for example, the resonance effects of a sextupole moment. The equation of motion expressed in terms of the b_2 moment is

$$\frac{\partial^2 x_N}{\partial \phi^2} + Q^2 x_N = -\frac{Q^2 B_0}{(B\rho)} \beta^{\frac{5}{2}}(\phi)\, b_2\, x_N^2. \tag{2.42}$$

If the driving term on the right hand side of the equation has the same frequency as a particle's tune, a resonant condition will exist. The right hand side is a product of a sextupole moment and x_N^2, both of which can be alternatively expressed as Fourier series in ϕ. The frequency of the driving term is a combination of the frequency $2Q$ expressed by x_N^2 and the harmonic frequency of $b_2\beta^{\frac{5}{2}}$. If the product $b_2\beta^{\frac{5}{2}}$ has a nonvanishing pth harmonic such that $p \pm 2Q = Q$, a resonant condition exists. The frequency $p + 2Q = Q$ leads to the condition that the tune should not be an integer if one wants to avoid a resonant condition. The frequency $p - 2Q = Q$ leads to the condition that the tune should not be a third of an integer.[9]

In general, the equation of motion for a driven harmonic oscillator is well suited for discussion using Hamiltonian techniques. Chapter 3 will concentrate on the Hamiltonian approach to solving this equation of motion for the nonlinear driving force of the beam-beam interaction.

2.3 THE TEVATRON AS A COLLIDER

In a typical colliding beam store, six proton bunches and six antiproton bunches circulate in the Tevatron in opposite directions. A given proton bunch passes by an opposing antiproton bunch at twelve locations in the ring. The details of the electromagnetic beam-beam interaction which occur at these twelve crossing points will be reviewed in the next chapter, so suffice it to say here that the beam-beam interaction will cause a tune spread of particles in the distribution which may cause some particles to shift onto resonances.

It was experimentally determined, for example, in the first Tevatron Collider Run (1987-1988) that the dominant factor limiting the luminosity was the beam-beam interaction. A "beam-beam limit" was reached in the Collider; the luminosity could not be increased by decreasing the beam emittance or by increasing the bunch intensity of the protons.[2] In order to minimize the adverse effects of the beam-beam interaction, electrostatic separators were installed in the Tevatron. The separators are oppositely charged stainless steel parallel plates which provide a transverse electrostatic field in the path of the particle. The electrostatic field causes particles of opposite charge to circulate on different closed orbits. The electrostatic fields in the Tevatron are in both transverse dimensions, causing closed orbits of the protons and antiprotons to wrap around each other in a double-helical fashion.

This ability to separate the beams in two dimensions is a unique capability of the Tevatron Collider. It proved to be a successful method of limiting adverse effects of the beam-beam interaction during normal collider operation.

The separators are configured to separate the beams everywhere except at the location of the Colliding Detector Facility (CDF) detector located at the B0 straight section and at the D0 detector. In order to provide the highest luminosity at these locations, 'low-beta' insertions are added.[5] Low beta insertions are composed of quadrupoles of a much larger focusing gradient than the quadrupoles used for focusing in the arcs. A low beta quadrupole in the Tevatron, for example, has twice the focusing gradient of a standard quadrupole, operating with a magnetic field gradient of 140 T/m at 1 TeV. Low beta quadrupoles are also much longer than quadrupoles in the arcs (approximately 180 inches as compared to 66 inches for a standard quadrupole) and thus have more than six times the focusing strength.

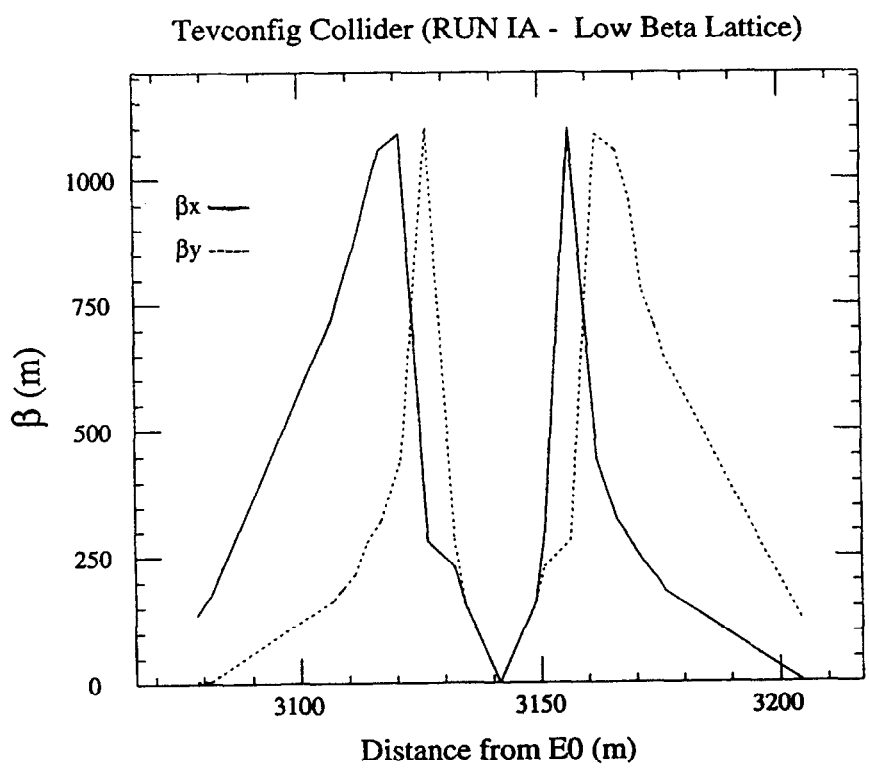

Figure 2.6: The horizontal (solid line) and vertical (dashed line) beta function at the CDF interaction region as specified by the design lattice of Collider Run IA.

The advantage of greater focusing strength is seen by substituting the transverse rms beam size of Equation 2.21 into the luminosity expression of Equation 1.2.

$$L = \frac{3 f_{rev} N_p N_{\bar{p}}}{2\beta\epsilon} F(z) \tag{2.43}$$

For a given emittance and bunch intensity, the highest luminosity will be achieved at the lowest beta. The strong focusing properties of the low beta insertion reduces the magnitude of the beta function at the collision point to less than a meter. The result of such strong focusing is that a transverse rms bunch size of approximately 1 mm in the arcs is focused to approximately 30 microns at the detector locations.

It is of interest to examine the change in the beta function in a low-beta insertion. The beta function through a straight section is found by setting the focusing strength equal to zero in Equation 2.11 and solving for β.

$$K = 0: \quad \beta(s) = \beta^* - 2\alpha^* s + \frac{(1+\alpha^*)^2}{\beta^*} s^2 \tag{2.44}$$

The lattice parameters denoted by the asterick are defined at the collision point which is, by definition, located at the azimuthal location $s = 0$. During Collider Run IA, the beta function varied quadratically from approximately 0.35 meters at either the B0 or D0 interaction points to 130 meters at the quadrupoles which marked the endpoints of the B0 and D0 straight sections. The variation of the beta function in the B0 interaction region as calculated from a model of the Tevatron is shown in Figure 2.6. The highest beta in the Tevatron (approximately 1100 meters) is reached at the defocusing low beta quadrupole locations in the low beta insertion.

2.4 Accelerator Parameters during Collider Runs IA and IB

Collider Run IA (1992-1993) and Collider Run IB (1994-1995) are characterized by operational accelerator parameters which are quite similar. An increase in the luminosity is apparent in Collider Run IB as the bunch intensities increase and operation of the accelerator continues to improve.

Collider Run IA was split into two "low-beta modes" of operation in which the magnitude of beta at both head-on collision points was changed. The first part of the run intended to collide protons and antiprotons at the B0 and D0 collision points with a 0.5m value of β^*. The presence of a beta wave in the Tevatron resulted in a lower β^* than the design value at both the B0 and D0 interaction points. The existence and consequences of the beta wave are discussed in the latter part of this section. The second part of the collider run attempted

to lower β^* to 0.25m to further increase the luminosity.

At the time of this writing, Collider Run IB has operated exclusively with a β^* of approximately 0.35m. Current machine studies are testing the possibility of operating at a β^* of 0.25m in the latter part of Run IB.

The experimental measurements which are presented in this dissertation were taken using the 0.5m β^* lattice of Collider Run IA and the 0.35m β^* lattice of Collider Run IB. Consequently, the conditions of operation discussed here concern only those relevant parts of Run IA and Run IB. Typical values of operational accelerator parameters during Collider Run IA and Collider Run IB are listed in Table 2.1.

Tevatron Accelerator Parameters

Parameter	Symbol	Run IA	Run IB
Kinetic Energy	E (GeV)	900	900
Dipole Bend Radius	ρ (m)	754	754
Revolution Frequency	f_{rev} (kHz)	47.7	47.7
Magnetic Rigidity	$\lvert B\rho \rvert$ (T-m)	3×10^3	3×10^3
Horizontal Tune	Q_x	20.585	20.583
Vertical Tune	Q_y	20.575	20.575
Synchrotron Tune	Q_s	5.7×10^{-4}	5.7×10^{-4}
Momentum Spread	σ_p/p	1×10^{-4}	1×10^{-4}
Protons per bunch	N_p	120×10^9	200×10^9
Antiprotons per bunch	$N_{\bar{p}}$	40×10^9	70×10^9
Proton Transverse Emittance	ϵ_{N_p} (π mm-mrad)	25	25
Antiproton Transverse Emittance	$\epsilon_{N_{\bar{p}}}$(π mm-mrad)	15	15
Longitudinal Emittance	ϵ_l (eV-sec)	4	4

Table 2.1: Tevatron accelerator parameters in Collider Run IA and Collider Run IB.

The actual collider lattice in the 0.5m β^* part of Run IA differed from its intended design in that a beta wave existed in both transverse dimensions of the Tevatron. As shown in Equation 2.37, a small perturbation of the strength of a quadrupole from its design specification will produce a beta wave which modifies the beta function of the design lattice. The problem in the Tevatron occurred in the magnetic fields produced by the quadrupoles in the low beta insertions. The transfer constants which represent the actual field produced for a given current differed in the real accelerator from the design specifications. The difference

between the beta function as specified by the design lattice and the beta function which was actually present during Collider Run IA is shown for a section of the Tevatron in Figure 2.7.[19]

The perturbation of the strength of the low beta quadrupole is too large to be described exactly by Equation 2.37. A perturbative analysis is not valid in this case.[20] It should be noted that the beta wave was corrected for in Collider Run IB by adding "low-beta trims"; power supplies were installed which allowed independent control of upstream and downstream low-beta quadrupoles to compensate for the gradient errors.

Tevatron Lattice Parameters

Lattice Parameter	Symbol (units)	Run IA B0	Run IA D0	Run IB B0	Run IB D0
Horizontal beta	β_x (m)	0.39	0.49	0.35	0.35
Vertical beta	β_y (m)	0.41	0.44	0.33	0.34
Horizontal dispersion	η_x (m)	0.02	0.01	-.005	0
Slope of dispersion	η_x'	0.08	0.06	0.28	0.28
Horizontal alpha	α_x	-0.34	-0.57	0.01	0.01
Vertical alpha	α_y	0.16	0.23	0.02	0.01

Table 2.2: Tevatron lattice parameters in Collider Run IA and Collider Run IB.

As Equation 2.37 indicates, a beta wave is directly proportional to the beta function at the location of the field error. The magnetic field error which produced the beta wave in the Tevatron occurred in a low beta quad which is at a high beta location. Peaks in the resulting beta wave were approximately 50% greater than that of the design during the 0.5m β^* run. Note, though, that the value of the beta function at the two head-on collision sites was lower than the design value. This was a nice consequence of the beta wave. The measured luminosity obtained during the 0.5m β^* run was greater than what was estimated using the design lattice.

Lattice parameters at the B0 and D0 interaction points for the 0.5 m β^* lattice of Collider Run IA and the 0.35 m β^* lattice of Collider Run IB are listed in Table 2.2.

The beta wave did cause some problems in operation though. When changing the tune in the Tevatron, it was found that the measured chromaticity also changed. Experiments which will be discussed in Chapter 5 indicated that the change in the measured chromaticity per tune unit using the 0.5m β^* lattice was approximately

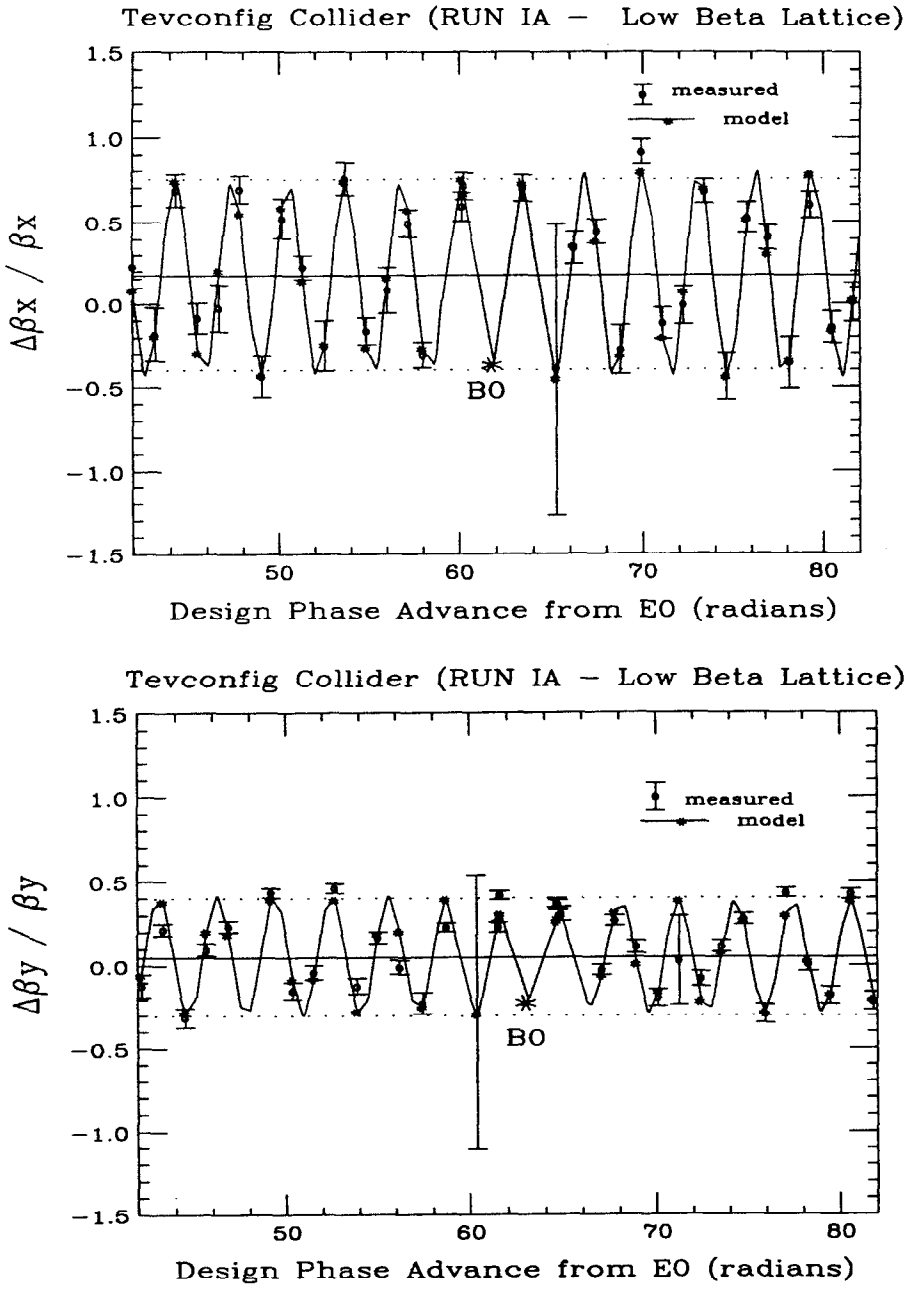

Figure 2.7: The horizontal and vertical beta wave in a section of the Tevatron. The vertical axis is the variation of beta from the design lattice. The solid line connects points calculated from a model of the Tevatron (Tevconfig) for Collider Run IA. Actual measurements of the beta function occurred at the points denoted by circles with error bars.

$$\frac{\Delta\xi_x}{\Delta Q_x} = 117 \quad \frac{\Delta\xi_y}{\Delta Q_y} = 50. \tag{2.45}$$

To verify this dependence of the 0.5m β^* lattice on the tune, the change in chromaticity per change in tune was calculated for two different models of the Tevatron. One of the models of the Tevatron contained the design lattice only and the other lattice more closely reproduced the beta wave in the Tevatron. The chromaticity did not vary when changing the tune of the design lattice. The chromaticity did change, however, when it was calculated for different tune settings of the lattice describing the beta wave. The calculated results showed good agreement with the experimental results. The reason for the change in chromaticity in the lattice describing the beta wave could be seen in the beta function. The average beta around the ring did not vary largely when the tune was changed in the design lattice, but there was a large increase in the average beta around the ring when the tune was changed in the lattice describing the beta wave.[17] As indicated in Equation 2.32, if there is an increase in the average beta around the ring, the chromaticity will increase also.

Chapter 3

THE BEAM-BEAM INTERACTION

3.1 THE BEAM-BEAM FORCE

A weak-strong model of the beam-beam interaction is used to define the motion of a "weak" or low intensity bunch colliding with a "strong" or high intensity bunch. A weak-strong picture of the beam-beam interaction translates in the Tevatron to an antiproton bunch colliding with a static electromagnetic field generated by a round, Gaussian, and short proton bunch. Antiprotons, in a weak-strong model, are the main focus of attention as test particles. Test particles differ from each other in that they have different amplitudes (a_x, a_y, a_s). The proton intensity is assumed to be large enough that protons are unaffected by the weak electromagnetic fields generated by low intensity antiprotons.

In the first approximation, the angular deflection a single antiproton experiences as it collides with a proton charge distribution does not depend on the longitudinal charge distribution of the protons.[28] The transverse charge distribution is assumed Gaussian and round for the counter-rotating proton bunch. In cylindrical coordinates, the proton charge distribution is given by

$$\rho(r) = \frac{ne}{2\pi\sigma^2} \exp\left[-\frac{r^2}{2\sigma^2}\right], \tag{3.1}$$

where σ is the rms transverse size of the bunch, n is the number of protons per unit length and e is the proton charge.

The electromagnetic force an antiproton experiences as it traverses a proton bunch is described by the Lorentz force:

$$\vec{F} = e(\vec{E} + \vec{v} \times \vec{B}) = e(E_r \pm \beta_{rel} c B_\phi)\, \hat{r}, \tag{3.2}$$

where $\hat{r}$ is a radial unit vector. A positive sign of the magnetic force term represents the force due to electromagnetic interactions with colliding protons; the beam-beam force. A negative magnetic force term corresponds to the Coulomb force between antiprotons in the same bunch; intrabeam scattering. The electric and magnetic fields counteract each other in the case of intrabeam scattering, but are additive in the case of the beam-beam force.

The electric field, E_r, and the magnetic field B_ϕ are described by Gauss' theorem and Ampere's Law, respectively.

$$E_r = \frac{ne}{2\pi\epsilon_0}\frac{1}{r}\left(1 - e^{-\frac{r^2}{2\sigma^2}}\right) \tag{3.3}$$

$$B_\phi = \frac{ne\mu_0\beta_{rel}c}{2\pi}\frac{1}{r}\left(1 - e^{-\frac{r^2}{2\sigma^2}}\right) \tag{3.4}$$

The kick $\Delta r'$ an antiproton receives from an interaction force F_r is

$$\Delta r' = \frac{L}{2\beta_{rel}c}\frac{1}{e(B\rho)}F_r, \tag{3.5}$$

where L is the proton bunch length. The beam-beam kick is found by substituting the beam-beam force into the kick expression:

$$\Delta r' = -\frac{2Nr_p}{\gamma_{rel}}\frac{1}{r}\left[1 - \exp\left(-r^2/2\sigma^2\right)\right]. \tag{3.6}$$

The classical radius of the proton is denoted by r_p and N is the total number of protons in the bunch ($N = nL$). Equation 3.6 is the beam-beam kick for a "head-on" beam-beam collision; the antiproton is oscillating about the same closed orbit as the centroid of the opposing proton bunch.

Figure 3.1 describes the beam-beam kick as a function of the oscillation amplitude of an antiproton normalized to σ of the opposing proton distribution. If the antiproton collides at a normalized amplitude which is much less than one, the kick is linear in r. The particle experiences an "electrostatic lens" force which, unlike a magnetic quadrupole, focuses in both the horizontal and vertical directions. When the normalized amplitude is approximately equal to one, the force on the antiproton becomes highly nonlinear. As shown in the figure, the beam-beam kick decreases like $1/r$ at large amplitudes.

For a small amplitude particle in one dimension, $x = r \ll \sigma$ and the beam-beam kick acts like a thin lens of focal length f, where

$$\frac{1}{f} = \frac{\Delta x'}{x}. \tag{3.7}$$

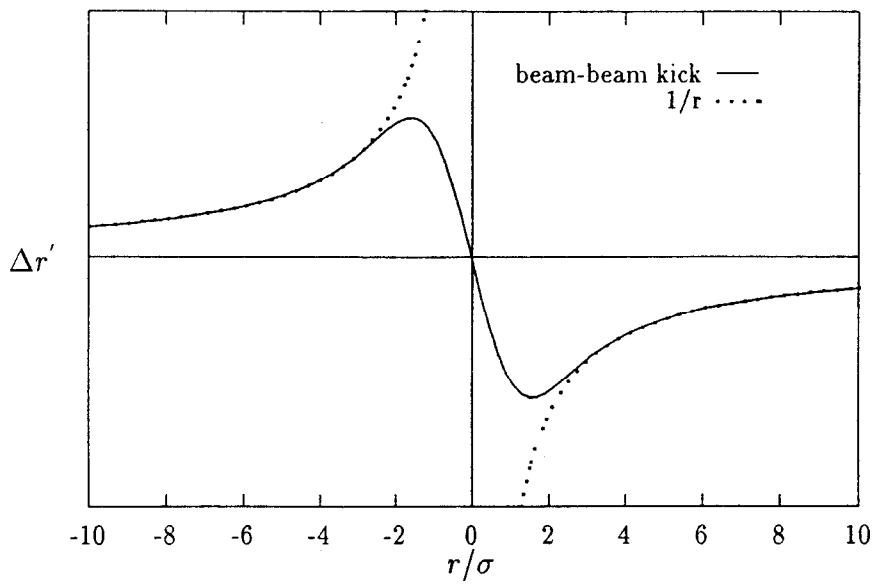

Figure 3.1: Angular deflection due to a proton-antiproton electromagnetic interaction as a function of the oscillation amplitude of a particle. The oscillation amplitude is normalized to the rms σ of the opposing charge distribution. A $1/r$ asymptotic dependence is observed.

Substituting for the focal length in Equation 2.25 (remembering $q = 1/f$), the tune shift of a small amplitude particle due to the beam-beam kick is

$$\begin{aligned} \xi &\simeq \frac{1}{4\pi}\beta\frac{\Delta x'}{x} \\ &= \frac{N r_p \beta}{4\pi\gamma_{rel}\sigma^2}, \end{aligned} \tag{3.8}$$

where β is measured at the beam-beam crossing point. The beam-beam tuneshift parameter ξ is an important scale factor which parameterizes the strength of the beam-beam kick. For non-round beams, the beam-beam tuneshift parameter is[28]

$$\xi_{x,y} = \frac{N r_0 \beta_{x,y}}{2\pi\gamma_{rel}\sigma_{x,y}(\sigma_x + \sigma_y)}. \tag{3.9}$$

3.2 A Hamiltonian Analysis

A two-dimensional Hamiltonian of a weak-strong colliding beam system is defined as

$$H(x, p_x, y, p_y; s) = \frac{1}{2}(p_x^2 + K_x x^2) + \frac{1}{2}(p_y^2 + K_y y^2) + V(x,y) \sum_{l=-\infty}^{\infty} \delta[s - (2\pi R l)] \tag{3.10}$$

where p_x and p_y are the canonical momenta associated with a particle's transverse positions in the horizontal and vertical planes, respectively.[32][24] The summation over l is a summation of the periodic crossing points in which a particle receives a localized beam-beam kick.

The beam-beam potential is described by Poisson's equation $\nabla^2 V = -\rho/\epsilon_0$ with the constraint that $V \to 0$ as $x, y \to \infty$.[33] In terms of x and y, the transverse charge distribution of Equation 3.1 is rewritten:

$$\rho(x,y) = \frac{ne}{2\pi\sigma_x\sigma_y} \exp\left[-\frac{1}{2}\left(\frac{x^2}{{\sigma_x}^2} + \frac{y^2}{{\sigma_y}^2}\right)\right]. \tag{3.11}$$

The beam-beam potential due to this charge distribution is

$$V(x,y) = \frac{Nr_p}{\gamma_{rel}} \int_0^\infty dt \, \frac{1 - \exp\left[-\frac{x^2}{2\sigma_x^2+t} - \frac{y^2}{2\sigma_y^2+t}\right]}{\sqrt{2\sigma_x^2+t}\sqrt{2\sigma_y^2+t}}. \tag{3.12}$$

An integration over the bunch length has occurred in the above expression, as evidenced by a change in the particles per unit length n to the total particles in the distribution N.

The symmetry of the potential expression dictates that only even-ordered resonances will be driven in head-on collisions. An expansion of the exponential term in the potential gives terms of order $x^{2n}y^{2m}$, where n and m are integers. In other words, $|n_x| \pm |n_y|$ of Equation 2.24 must be equal to an even integer. Just like any nonlinear resonance driving term (caused by sextupole magnets or octupole magnets, for example), these driving terms excite resonances whenever the betatron tunes satisfy the resonance condition described by Equation 2.24.

Odd-ordered resonances require the symmetry of the potential to be broken, and are present when the beams are separated transversely or when there is dispersion or a crossing angle at the collision point. If there is a transverse separation between the closed orbit of the particle and the centroid of the colliding particle distribution, the potential is redefined as

$$V(x,y) = \frac{Nr_p}{\gamma_{rel}} \int_0^\infty dt \, \frac{1 - \exp\left[-\frac{(x-d_x)^2}{2\sigma_x^2+t} - \frac{(y-d_y)^2}{2\sigma_y^2+t}\right]}{\sqrt{2\sigma_x^2+t}\sqrt{2\sigma_y^2+t}}, \tag{3.13}$$

where d_x and d_y denote the horizontal and vertical separations of a particle from the centroid of the bunch distribution.

At a single crossing point, the equations of motion described by the Hamiltonian of Equation 3.10 are

$$\frac{dz^2}{ds^2} + K_z(z) = -\frac{\partial V}{\partial z}\,\delta[s], \quad z \equiv x, y. \tag{3.14}$$

THE UNPERTURBED HAMILTONIAN

Consider the simple case of a one-dimensional system ($y = 0$) in which the beam-beam potential is equal to zero. Hamilton's equation $\partial H/\partial p_x = x'$ yields the relation $p_x = x'$ and confirms the conjugate coordinate of the position x as x'. A generating function is used to canonically transform the Hamiltonian into a new Hamiltonian using action-angle coordinates $(\vec{J}, \vec{\phi})$. The new Hamiltonian has the advantage of being independent of the longitudinal coordinate s if one introduces a periodic coordinate, $\tilde{\psi}_x$, which is related to ψ_x of Equation 2.12 by

$$\tilde{\psi}_x = \psi_x - Q_x\theta = \psi_x - \frac{Q_x s}{R}. \tag{3.15}$$

The generating function used in the canonical transformation is given by[31]

$$\begin{aligned} G_x(x, \phi_x; s) &= -\frac{x^2}{2\beta_x}[\tan F_x + \alpha_x], \quad where \\ F_x &\equiv \psi_x - Q_x\theta + \phi_x \end{aligned} \tag{3.16}$$

This generating function produces the coordinate transformations[21]

$$x = \sqrt{2J_x\beta_x}\cos(\tilde{\psi}_x + \phi_x) \tag{3.17}$$

$$x' = -\sqrt{\frac{2J_x}{\beta_x}}\left[\sin(\tilde{\psi}_x + \phi_x) + \alpha_x\cos(\tilde{\psi}_x + \phi_x)\right], \tag{3.18}$$

and the new Hamiltonian is

$$H_1 = H(x, x'; s) + \frac{dG_x}{ds} = \frac{Q_x J_x}{R}. \tag{3.19}$$

The parameter R is a scaling of the longitudinal parameter s. By rescaling the Hamiltonian using θ, the parameter R is eliminated. Recalling that $d/d\theta = Rd/ds$, the Hamiltonian is

$$H_1(J_x, \phi_x; \theta) = H_1(J_x, \phi_x; s) \times R = Q_x J_x. \tag{3.20}$$

The equations of motion are given by

$$\dot{\phi}_x = \frac{\partial H_1}{\partial J_x} = Q_x, \tag{3.21}$$

$$\dot{J}_x = -\frac{\partial H_1}{\partial \phi_x} = 0, \tag{3.22}$$

where the dot notation designates a derivative with respect to θ. With no beam-beam interaction, the amplitude of a particle at a given location remains constant: $J_x = constant$. J_x is therefore equal to the area enclosed by the ellipse in (x, x') phase space. The invariant single particle emittance is closely related to the invariant J_x; $J = A^2/2$, where πA^2 is the invariant described in Equation 2.17.

An equivalent derivation holds for both transverse degrees of freedom. The unperturbed part of the Hamiltonian described by Equation 3.10 is thus

$$H(\vec{J}, \vec{\phi}; \theta) = Q_x J_x + Q_y J_y = \vec{Q} \cdot \vec{J} \tag{3.23}$$

This system is equivalent to a system of two uncoupled harmonic oscillators.

THE RESONANT HAMILTONIAN

It is of interest to examine a particle's motion due to a single resonance, that is, to isolate part of the Hamiltonian when a particle's tune Q is close to a value satisfying $nQ \approx p$, where n and p are integers. The resulting "resonant" Hamiltonian is used to delineate a particle's motion when its tune is close to a resonance of order n. With the inclusion of the beam-beam perturbation, the resonant Hamiltonian is of the form[32][24]

$$H_n(\vec{J}, \vec{\phi}; \theta) = \vec{Q} \cdot \vec{J} + \vec{\xi}\, U(\vec{J}) + \vec{\xi} V_n(\vec{J}) \cos(\vec{n} \cdot \vec{\phi} + m\theta). \tag{3.24}$$

The first term in the Hamiltonian describes the linear motion of a particle near a resonance of order n. The last two terms are scaled by the linear beam-beam tuneshift parameter; both terms are due to the beam-beam interaction. The term $U(\vec{J})$ is the amplitude detuning function which describes the variation of tune with amplitude due to the beam-beam interaction. The term $V_n(\vec{J})$ is a beam-beam "resonant excitation" term and is known as the resonance width function.[32] Each of these terms will be discussed in more detail in the next two sections.

An important property of a single resonance model is found from Hamilton's equation of motion describing a particle's amplitude.[21] Motion dominated by a single resonance is given by

$$\dot{\vec{J}} = \vec{n}\ (\vec{\xi} V_n(\vec{J})\ \sin(\vec{n} \cdot \vec{\phi} + m\theta)\,). \tag{3.25}$$

The dot denotes a derivative with respect to θ. Equation 3.25 points to a relation between the two transverse amplitudes:

$$\frac{\dot{J}_x}{n_x} + \frac{\dot{J}_y}{n_y} = constant \tag{3.26}$$

or, equivalently,

$$\frac{J_x}{n_x} + \frac{J_y}{n_y} = c_1 + c_2 f(\theta) \tag{3.27}$$

where c_1 and c_2 are constants. A particle's motion plotted in amplitude space (J_x, J_y) follows a straight line. Motion in amplitude space is bounded or unbounded depending upon the signs of n_x and n_y. Bounded motion occurs when one of the components of $\vec{n}$ are negative; when the resonance is a "difference resonance". A growth in a particle's horizontal amplitude, for example, will lead to a decrease in a particle's vertical amplitude. Unbounded growth in amplitude occurs when both components of $\vec{n}$ are positive; when the resonance is a "sum resonance". This relation has led to a popular assumption that sum resonances are dangerous resonances and that difference resonances are safe. What is not considered in this assumption is that even in the case of bounded motion in amplitude space, a particle still has the potential of being lost due to a large amplitude growth in one dimension.

3.3 THE BEAM-BEAM TUNE SHIFT

In the absence of all resonances ($n = 0$), a particle's tune shift due to the beam-beam interaction is derived from the amplitude detuning function $U(\vec{J})$ in the resonant Hamiltonian. This amplitude detuning function is obtained from the beam-beam potential using the action-angle coordinate transformation of Equation 3.15. In the case of round beams, $\sigma_x = \sigma_y$ is σ and the beam-beam potential in terms of action-angle coordinates is given by

$$V(\vec{J}, \vec{\phi}) = \frac{N r_o}{\gamma} \int_0^\infty dt \, \frac{1}{2\sigma^2 + t} \left(1 - \prod_{k=1,2} \exp\left[\frac{-\left(\sqrt{2J_k\beta_k}\cos\phi_k - d_k\right)^2}{2\sigma^2 + t} \right] \right). \tag{3.28}$$

The product over k represents the two transverse dimensions; $(1,2) \equiv (x,y)$.

Consider the case of a non-zero separation d in the horizontal direction. Equation 3.28 is rewritten as

$$V(\vec{J}, \vec{\phi}) = \frac{N r_o}{\gamma} \int_0^1 \frac{du}{u} \left(1 - \exp\left[-u \left(\sqrt{\frac{J_x}{2\epsilon}} \cos\phi_x - \frac{d_N}{2} \right)^2 - u \frac{J_y}{2\epsilon} \cos^2\phi_y \right] \right). \tag{3.29}$$

The separation, d_N, is a normalized horizontal separation ($d_N \equiv d/\sigma$). The variable of integration has been changed to u, where $u \equiv 1/(1 + (t/\sigma^2))$. The beam emittance ϵ is substituted into the expression ($\epsilon = \sigma^2/\beta$), where the beam emittance of Equation 2.20 is defined at 1σ.

The detuning function of the resonant Hamiltonian is found by averaging the beam-beam potential over all angles. In one dimension, the detuning term in the resonant Hamiltonian is

$$\xi\, U(J) = \frac{1}{2\pi} \int_0^{2\pi} V(J, \phi)\, d\phi. \tag{3.30}$$

The beam-beam tune shift is obtained from the derivative of the detuning term. This is seen by examining Hamilton's phase equation of motion. In the absence of resonances,

$$\frac{d\phi}{d\theta} = \frac{\partial H}{\partial J} = Q - \xi\, \frac{\partial U(J)}{\partial J} \tag{3.31}$$

or, equivalently, the shift in tune is

$$\Delta Q = \xi\, \frac{\partial U(J)}{\partial J}. \tag{3.32}$$

Horizontal and vertical tune shifts for round beams in the presence of a non-zero horizontal separation are given by[29]

$$\frac{\Delta Q_x}{\xi_x} = \frac{1}{2\pi} \int_0^{2\pi} d\phi\, \frac{\cos\phi}{\alpha_x \left[\cos\phi - \frac{d_N}{2\sqrt{\alpha_x}}\right]} \left(1 - \exp\left[-2\left(\sqrt{\alpha_x}\cos\phi - \frac{d_N}{2}\right)^2\right]\right) \tag{3.33}$$

and

$$\frac{\Delta Q_y}{\xi_y} = \frac{1}{2\pi} \int_0^{2\pi} d\phi\, \frac{\cos^2\phi}{\alpha_y \cos^2\phi + \frac{d_N^2}{4}} \left(1 - \exp\left[-\left(2\alpha_y \cos^2\phi + \frac{d_N^2}{2}\right)\right]\right). \tag{3.34}$$

For convenience, the parameter α has been used in the above expressions, where

$$\alpha_k = \frac{J_k}{2\epsilon_k}, \tag{3.35}$$

and $k \equiv x, y$. Horizontal and vertical tune shifts for various beam separations in the horizontal plane are plotted in Figure 3.2. Tune shifts are plotted as a function of normalized particle amplitude, a. The amplitude of a particle is defined in terms of action-angle coordinates as

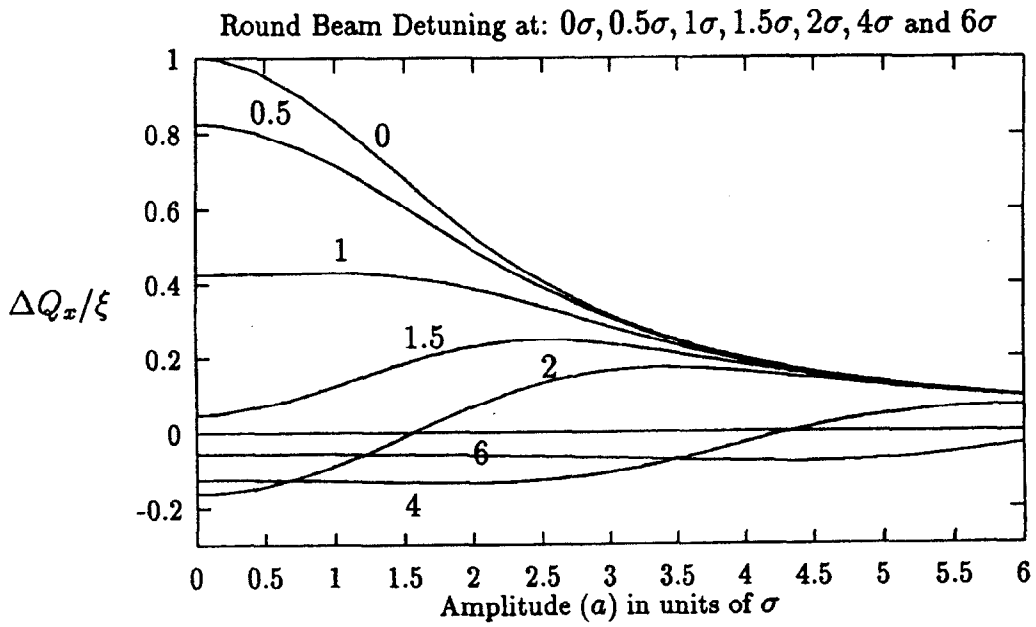

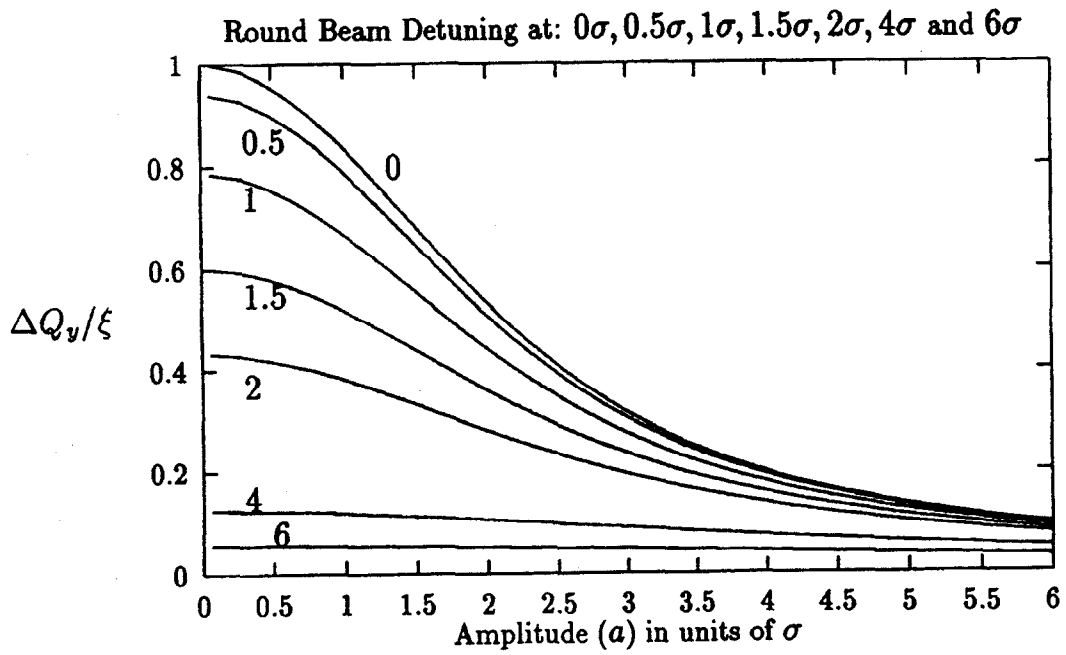

Figure 3.2: Horizontal and vertical tune shift due to beam-beam detuning in the presence of horizontal separation. A round beam approximation is used.

$$a = \sqrt{x^2 + (\alpha x + \beta x')^2} = \sqrt{2\beta J} \tag{3.36}$$

Normalizing to the transverse beam size of the proton distribution,

$$a = \sqrt{\frac{2J}{\epsilon}} \tag{3.37}$$

and is in units of σ.

Note that horizontal and vertical tune shifts are scaled by the beam-beam tuneshift parameter. Maximum tune shifts for any amplitude particle occur in the case of head-on collisions. In head-on collisions, small amplitude particles are shifted in tune by the largest amount. The shift in tune decreases nonlinearly with particle amplitude. Amplitude dependent tune shifts lead to a spread in particle tunes for a distribution of particles. The antiproton tune spread characteristic of one head-on collision in the Tevatron during Collider Run IB is mapped in Figure 3.3 as a "beam-beam tune footprint". In the figure, the tune which is unperturbed by the beam-beam interaction (referred to as the base tune in this work) is marked with a cross mark. Zero amplitude antiprotons are shifted linearly in tune by approximately 0.006 tune units both horizontally and vertically. A typical Collider Run in the Tevatron operates with two head-on collisions and thus with a linear tune shift ξ of 0.012.

The beam-beam interaction redefines the working point for particles with unperturbed tunes into a working area in tune space. For good beam lifetimes and stable operating conditions, it is desirable to keep the entire area in which particles are spread in tune away from destructive resonance lines in tune space.

It is interesting to note that the amplitude dependent tune shift which results from the beam-beam interaction is predicted to have a stabilizing effect on a particle in resonance. Consider a situation in which a small amplitude particle is driven into resonance and experiences amplitude growth. The tendency of the particle to take on different tunes as it grows in amplitude characterizes a "detuning" effect. The rate of a particle's amplitude growth will decrease as the particle is shifted in tune off of a resonance. The detuning effect brings the destructive effects of the resonance under control. This is an important aspect of the beam-beam force. The phase space of a particle in the presence of the beam-beam interaction is always a closed phase space; a chaotic region which may exist will not extend to infinity. Previous beam-beam studies have examined the onset of resonance islands in phase space and the overlap of resonance islands which leads to chaotic motion. Surprisingly, typical strengths of the beam-beam interaction in hadron colliders are much smaller than that predicted for the onset of chaotic motion in a particle's phase space. Resonance overlap

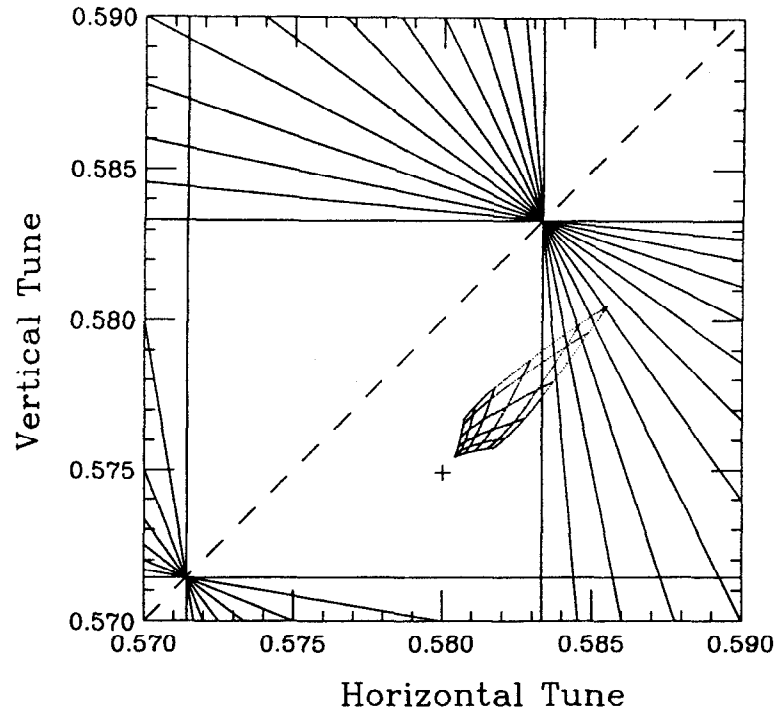

Figure 3.3: Beam-beam tune footprint for one head-on collision in the Tevatron Collider. The footprint was calculated analytically for antiprotons with oscillation amplitudes ranging from 0 to 5σ.

has been observed when an external modulation, such as a tune modulation, is added to the beam-beam model.[24][23][22]

In a real collider, though, beam stability in the presence of the beam-beam interaction is not observed. It will be shown in this work that higher background rates are driven by the beam-beam interaction in the Tevatron when the operating tune is near 7th and 9th order resonances. The SPS collider at the European Laboratory for Particle Physics (CERN) found destructive beam-beam effects (a decrease in beam lifetime) due to the 16th order resonance. Higher background rates were also measured in the SPS due to an increased beam-beam interaction effect for proton and antiproton emittances of unequal size.[26] A long range beam-beam experiment performed in the Tevatron collider showed an increased beam loss when the proton and antiproton bunches were separated by about 1.5 σ to 2.0 σ.[27]

3.4 Amplitude of a Resonance

As expressed in Equation 3.28, the beam-beam potential is an even function in angle. In one dimension, the Fourier series expansion of the beam-beam potential is

$$V(J,\phi) = \sum_{n=1}^{\infty} V_n(J)\cos n\phi, \tag{3.38}$$

where the summation over n includes all orders of resonances. In an isolated resonance model, a single resonance of order n is accepted as the dominant resonant term. Higher order terms are neglected as contributing to a particle's resonant motion. The resonant width function, $V_n(J)$ of Equation 3.24, represents the amplitude of the dominant resonant excitation term in the beam-beam potential.

The amplitude of a beam-beam resonant driving term is obtained from the derivative of the beam-beam potential ($\vec{F} = -\nabla V$). The Fourier series expansion of beam-beam driving terms of order n is given by

$$\left(\frac{\partial V(J,\phi)}{\partial J}\right) = \sum_{n=1}^{\infty}\left(\frac{\partial V_n(J)}{\partial J}\right)\cos n\phi. \tag{3.39}$$

The amplitude of a resonance of order n is the nth Fourier component of its Fourier series expansion. This amplitude is the derivative of the resonance width function with respect to J.

$$\left(\frac{\partial V_n(J)}{\partial J}\right) = \frac{1}{\pi}\int_0^{2\pi} d\phi\left(\frac{\partial V(J,\phi)}{\partial J}\right)\cos n\phi \tag{3.40}$$

Substituting the beam-beam potential of Equation 3.28 into the above expression gives the amplitude of a resonance due to the beam-beam interaction:

$$V_n'(\alpha) = \xi\frac{1}{2\pi}\int_0^{2\pi} d\phi\frac{\cos n\phi\cos\phi}{\alpha\left(\cos\phi - \frac{d_N}{2\sqrt{\alpha}}\right)}\left(1 - \exp\left(-2\left[\sqrt{\alpha}\cos\phi - \frac{d_N}{2}\right]^2\right)\right), \tag{3.41}$$

where ξ is the linear beam-beam tuneshift parameter and the prime denotes a derivative with respect to J.[29]

For head-on collisions, the amplitude of the resonance for various even-ordered resonances is shown in Figure 3.4 and 3.5. Both figures normalize the resonance amplitude to the beam-beam tune shift parameter. Figure 3.4 displays the absolute value of the resonance amplitude in the more familiar logarithmic scale seen in much of the literature (See Evans (1983) or Peggs (1986), for example). Figure 3.5 is the resonance amplitude plotted on a linear scale. It is evident in both of these figures that the absolute magnitude of the resonant component of the beam-beam perturbation is greater for lower order resonances than for higher order resonances. This is true for a particle at any oscillation amplitude.

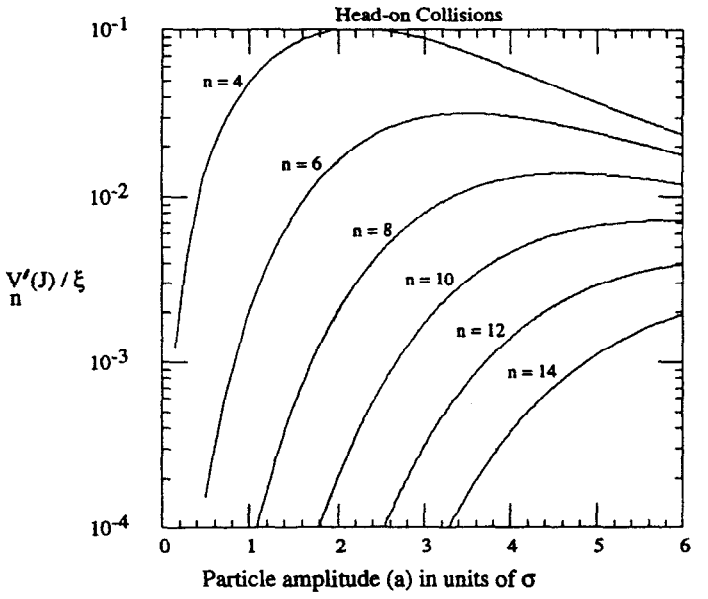

Figure 3.4: Absolute value of the amplitude of a beam-beam driven resonance of order n for head-on collisions. A round beam approximation is used.

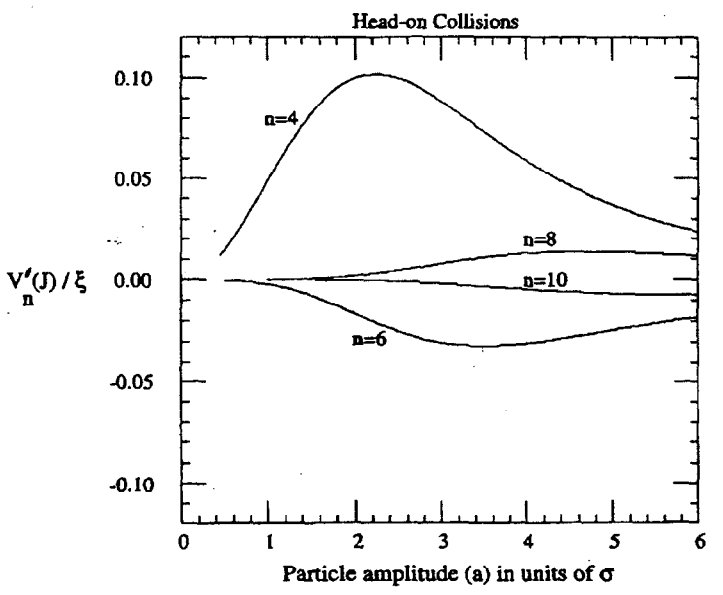

Figure 3.5: Amplitude of a beam-beam driven resonance of order n for head-on collisions. A round beam approximation is used.

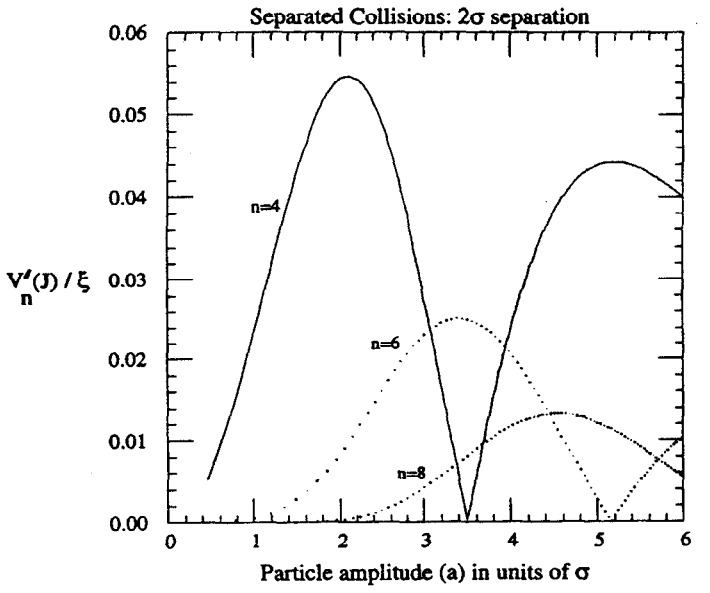

Figure 3.6: Absolute value of the amplitude of a beam-beam driven resonance of order n for a beam separation of 2σ. A round beam approximation is used.

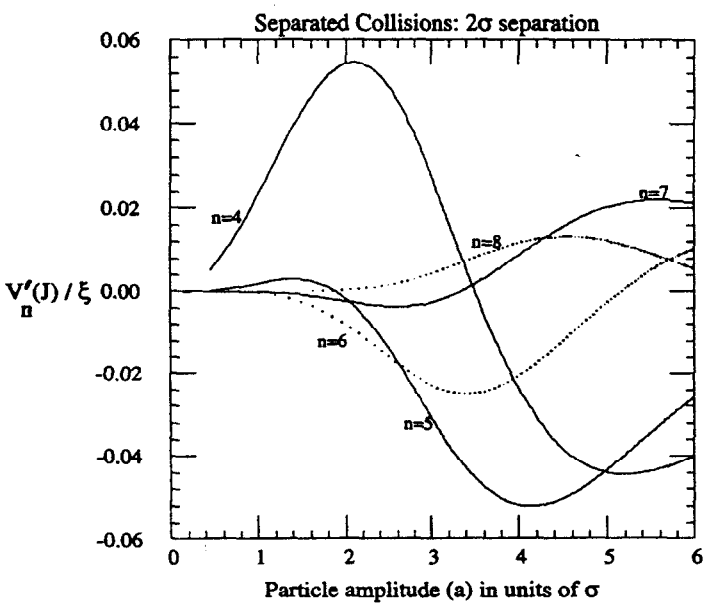

Figure 3.7: Amplitude of a beam-beam driven resonance or order n for a beam separation of 2σ. A round beam approximation is used.

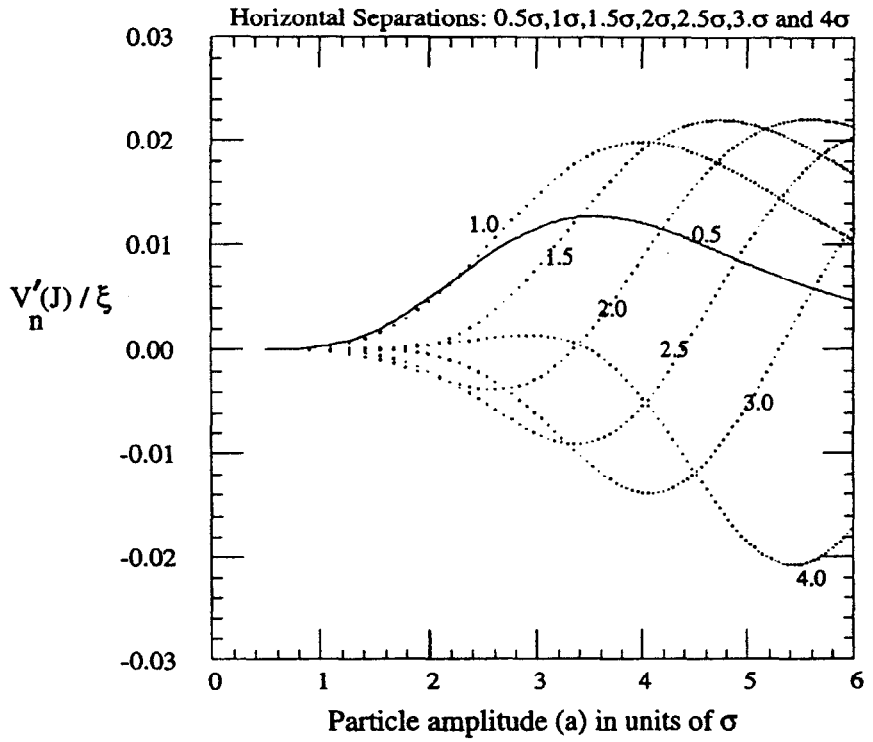

Figure 3.8: Amplitude of a beam-beam driven resonance of $7th$ order for different horizontal separations. A round beam approximation is used.

A non-zero separation introduces resonant components of the beam-beam force which drive odd-ordered resonances. For a separation of 2σ, the resonance amplitude is plotted for some odd and even-ordered resonances in Figure 3.6 and Figure 3.7. Although driving terms from lower order resonances have a maximum oscillation amplitude which is larger than higher order resonances, it is no longer possible to generalize that the amplitude of a beam-beam resonant driving term is larger for lower order resonances. A particle oscillating at a given amplitude may in fact see a larger resonance excitation near a higher order resonance.

The dependence of resonance amplitude on beam separation is shown in Figure 3.8 for a seventh order resonance.

3.5 BEAM-BEAM SIMULATIONS

In order to predict a particle's behavior in the presence of the beam-beam interaction in the Tevatron, a simulation code was developed to calculate the predicted position and phase of a particle after a designated number of turns. The simulation code is descendant from simulation code originally written by Werner Herr.[34][35]

The model used for the simulation is concerned only with particle motion due to the beam-beam interaction. The motion of a particle between beam-beam crossing points is assumed to be linear motion and coupling between the two transverse planes is not taken into account. The particle experiences an angular kick due the beam-beam interaction at each beam-beam crossing point. The simulation code is summarized below.

Given a particle's initial position and phase at a location 1 in a collider, a linear propagation to location 2 is described by

$$\begin{pmatrix} x_2 \\ x_2' \\ y_2 \\ y_2' \end{pmatrix} = M_{12} \begin{pmatrix} x_1 \\ x_1' \\ y_1 \\ y_1' \end{pmatrix}. \tag{3.42}$$

The transfer matrix M is defined by the lattice parameters in the horizontal and vertical planes at the corresponding locations [9]:

$$M_{12} = \begin{pmatrix} m_x & 0 \\ 0 & m_y \end{pmatrix}, \tag{3.43}$$

where m_x and m_y are given by Equation 2.13. The simulation assumes the motion of a particle from one beam-beam collision point to the next is a linear motion as described above. The phase advance from a beam-beam crossing point (1) to the next crossing point (2) is given by

$$\Delta\phi = \phi_2 - \phi_1 = 2\pi\Delta Q_{21}. \tag{3.44}$$

At each beam-beam interaction point, a beam-beam kick of magnitude $\Delta x'$ and $\Delta y'$ is added to a particle's phase. The beam-beam kick expression of Equation 3.5 is generalized to non-round beams in the simulation. For computational purposes, the vertical kick in the simulation is given by

$$\begin{aligned} \Delta y' &= -\frac{2N_b r_p y}{\gamma}\sqrt{\frac{2\pi}{a^2-b^2}} \cdot \\ &\mathcal{R}\left[w\left(\frac{x+iy}{\sqrt{2(a^2-b^2)}}\right) - \exp\left[\left(-\frac{x^2}{2a^2}-\frac{y^2}{2b^2}\right)\right] w\left(\frac{x\frac{b}{a}+iy\frac{a}{b}}{\sqrt{2(a^2-b^2)}}\right)\right] \end{aligned} \tag{3.45}$$

for $a > b$.[38] The parameters a and b denote the horizontal and vertical bunch sizes of the colliding proton distribution. The function $w(A+iB)$ is the complex error function.

The horizontal kick is given by the imaginary part of the square brackets. The use of an algorithm to calculate the complex error function using an asymptotic approximation and Pade approximations decreased computation time significantly.[39]

When a non-zero beam separation is present at a collision point, care must be taken in calculating the beam-beam kick.[36] Consider a beam-beam collision with a non-zero separation d in the horizontal plane. The beam-beam potential of Equation 3.13 is

$$V(x,y) = C \int dt \frac{1 - e^{-\left(\frac{(x-d)^2}{2\sigma_x^2+t} + \frac{y^2}{2\sigma_y^2+t}\right)}}{\sqrt{(2\sigma_x^2+t)(2\sigma_y^2+t)}} \tag{3.46}$$

where $C = Nr_p/\gamma$. The kick from this potential is

$$\begin{aligned} \Delta x' &= \frac{\partial V}{\partial x} \\ &= C(x-d) \int dt \frac{e^{-\left(\frac{(x-d)^2}{2\sigma_x^2+t} + \frac{y^2}{2\sigma_y^2+t}\right)}}{\sqrt{(2\sigma_x^2+t)^{3/2}(2\sigma_y^2+t)^{1/2}}}. \end{aligned} \tag{3.47}$$

For zero amplitude particles, this expression becomes

$$\Delta x' = Cd \int dt \frac{e^{-\left(\frac{d^2}{2\sigma_x^2+t}\right)}}{\sqrt{(2\sigma_x^2+t)^{3/2}(2\sigma_y^2+t)^{1/2}}} \tag{3.48}$$

which is merely a dipole kick. This dipole kick will result in a shift in the closed orbit of the particle. In order to calculate a particle's tune, it is necessary to calculate the gradient of the kick around the closed orbit of the particle, i.e. x=0. The approximation of Equation 3.8, $q = \Delta x'/x$, which was used in the head-on collision case is no longer valid. The valid expression is

$$q = \frac{\partial(\Delta x')}{\partial x}. \tag{3.49}$$

The change in a particle's closed orbit due to the constant dipole kick is negligible for small kicks, but the change is large for sizeable kicks. A large dipole kick will change a particle's reference system. A subtraction of the dipole kick is necessary to bring the reference system back. The beam-beam kick used in the simulation code is obtained by subtracting out the dipole kick contribution;

$$\Delta x'_{total} = \Delta x'(y+d) - \Delta x'(d). \tag{3.50}$$

This beam-beam kick expression will give a correct calculation of the beam-beam tune shift of a particle. If the dipole contribution is not subtracted, small amplitude particles will assume much larger amplitudes. These particles will then start betatron oscillations with larger

amplitudes than their original amplitudes and start to sample a different amplitude of the opposing beam. In reality, the particles oscillate with the same betatron amplitudes but at different closed orbits. The tune change is thus

$$\Delta Q \propto q = C\frac{\partial}{\partial x}\left((x-d)\int dt \frac{e^{-\left(\frac{(x-d)^2}{2\sigma_x^2+t}+\frac{y^2}{2\sigma_y^2+t}\right)}}{\sqrt{(2\sigma_x^2+t)^{3/2}(2\sigma_y^2+t)^{1/2}}}\right) \tag{3.51}$$

and

$$\Delta Q \propto q = C\int dt \frac{e^{-\left(\frac{(x-d)^2}{2\sigma_x^2+t}+\frac{y^2}{2\sigma_y^2+t}\right)}}{\sqrt{(2\sigma_x^2+t)^{3/2}(2\sigma_y^2+t)^{1/2}}} - 2C(x-d)^2\int dt \frac{e^{-\left(\frac{(x-d)^2}{2\sigma_x^2+t}+\frac{y^2}{2\sigma_y^2+t}\right)}}{\sqrt{(2\sigma_x^2+t)^{5/2}(2\sigma_y^2+t)^{1/2}}} \tag{3.52}$$

For $x = 0$, the linear tune shift is

$$\Delta Q \propto q = C\int dt \frac{e^{-\left(\frac{d^2}{2\sigma_x^2+t}+\frac{y^2}{2\sigma_y^2+t}\right)}}{\sqrt{(2\sigma_x^2+t)^{3/2}(2\sigma_y^2+t)^{1/2}}} - 2Cd^2\int dt \frac{e^{-\left(\frac{d^2}{2\sigma_x^2+t}+\frac{y^2}{2\sigma_y^2+t}\right)}}{\sqrt{(2\sigma_x^2+t)^{5/2}(2\sigma_y^2+t)^{1/2}}} \tag{3.53}$$

The first term is the well known classical part. The second term can cause the tune shift to become negative after a certain separation d.

Figure 3.9 illustrates the beam-beam tune shift vs. separation as computed by the simulation code. The horizontal and vertical tune shift due to one beam-beam collision is shown for a small amplitude $(0.001\sigma_x, 0.001\sigma_y)$ and a large amplitude $(2\sigma_x, 2\sigma_y)$ particle. The operating tune for the above simulation runs was in a "resonance free" region of tune space; a region absent of lower order resonances.

It is of interest in this work to compare beam-beam simulations to particle losses. In this case, the absolute position of a particle at a given location in the ring is important. The orbit offset due to the dipole kick which is subtracted from the beam-beam kick during particle tracking must be taken into account. The dipole kick causes a particle to orbit on a new closed orbit. All amplitude particles in a particle distribution are kicked equally by the dipole kick. It is sufficient to calculate the additional orbit offset which results from the dipole kick and add this orbit offset to that measured during tracking.[44] The closed orbit offset is calculated using Equation 2.35.

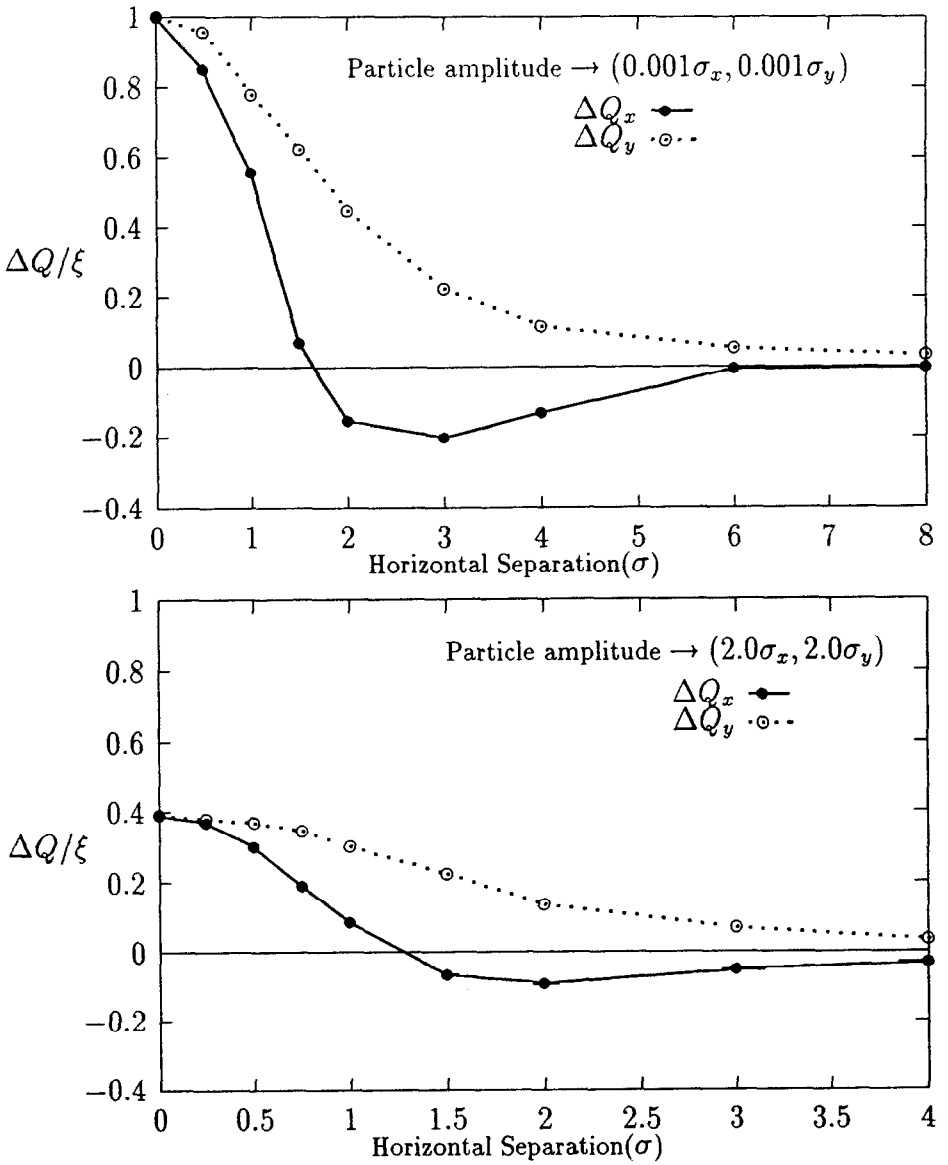

Figure 3.9: Simulation results of the tune shift of a small and large amplitude particle in the presence of a non-zero horizontal separation.

Chapter 4

EXPERIMENTAL METHODS OF MEASUREMENT

4.1 MEASUREMENT OF THE TUNE

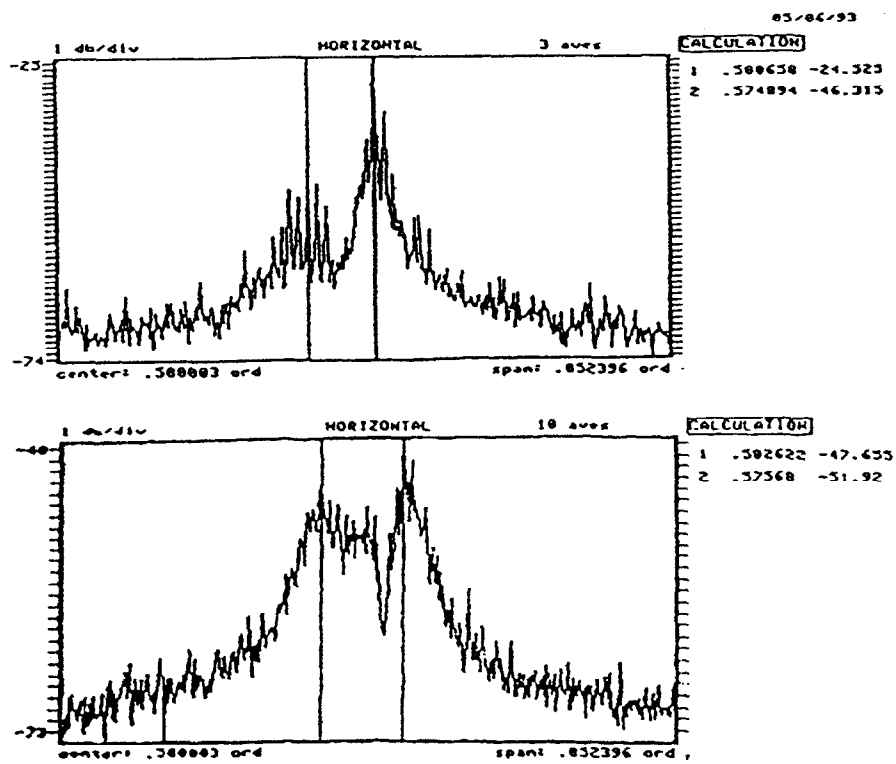

Figure 4.1: Tune spectrum measured from horizontal Schottky plates in the Tevatron. The top picture is the tune spectrum of a proton beam. The bottom picture displays a tune spectrum during a colliding beam store. Two peaks are evident due to coupling between the horizontal and vertical motion of the beam.

A measurement of the tune of protons in the Tevatron is obtained using a Schottky Detector System. The detector consists of opposing one meter long plates in the beam pipe

which are electrically in parallel with an inductor. The Schottky assembly is tuned to produce a resonant circuit frequency at $21.4 MHz$.[45] The output signal of the circuit assembly is fed into a spectrum analyzer for a specified length of time. A Fast Fourier Transform of the time domain signal is then calculated. The signals of Figure 4.1 are the resultant tune spectrum obtained during a proton store and for a colliding beam store. The horizontal axis is in tune units labelled as ords (orders or revolutions); 1 ord = 47,713.15 Hz. The vertical axis is the power spectrum of the beam in units of dB.

The relation $\Delta f \Delta t = 1$ determines the resolution of the tune measurement. The length of time data is recorded, Δt, is the inverse of the resolution bandwidth of the detector. Under normal operating conditions of the Collider and during the beam-beam experiments discussed in this work, Δt is 84 msec; data is read for approximately 4000 turns. This corresponds to $\Delta f = 12$ Hz or a tune resolution of approximately 0.0003. The tune signal on the spectrum analyzer is broadened, though, by the tune spread of particles due to the non-zero chromaticity of the bunch distribution. Tune signals in the case of two colliding bunches are also broadened by the amplitude dependent tune spread caused by the beam-beam interaction.

The Tevatron Schottky detector was so named because it was designed to measure transverse Schottky signals; signals arising from the incoherent motion of particles in a circular accelerator. Historically, measurements of Schottky noise on unbunched beam in the CERN ISR led to the powerful technique of stochastic cooling.[46] Bunched beam situations, though, make measurements of Schottky noise much more difficult. In fact, signals from the Schottky detector in the Tevatron are dominated by coherent motion of the proton bunches rather than by incoherent Schottky noise. The power spectrum of coherent motion is proportional to the the square of the number of particles in the distribution. Incoherent motion gives a power spectrum which is linearly proportional to the number of particles in the distribution.[46] The existence of noise at the betatron sideband frequencies produces a response of the beam which has much greater power than the magnitude of a Schottky signal. Modulated power supply ripple, for example, has been shown to be a source of noise which drives coherent motion of protons in the Tevatron. Power supply ripple has been measured to have a strong effect on transverse bunch motion and the resultant tune spectrum.[47]

4.2 Background Losses

The most sensitive loss monitors to measure proton and antiproton background losses in the Tevatron are located at the CDF and D0 detector facilities in the ring. The loss monitors

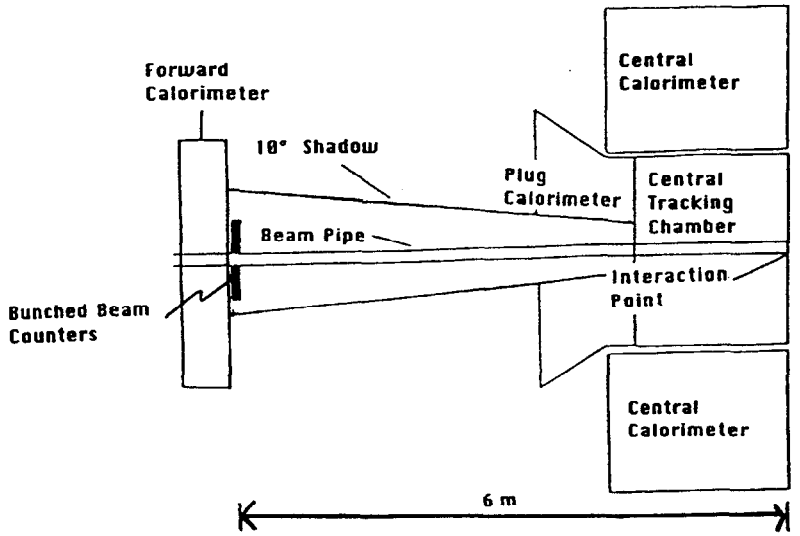

Figure 4.2: A sketch of one half of the CDF detector. The detector is axisymmetric about the Interaction Point. The longitudinal location of the Bunched Beam Counters is specified.

at CDF are described.

As indicated in Figure 4.2, the loss monitors are located at a distance of 6 meters from the east and west sides of the main CDF detector.[49] A scintillating material connected to a photomultiplier tube is used for particle detection. An array of scintillators, as sketched in Figure 4.3, surround the beam pipe.[49]

A particle passing through a scintillator on both sides of the detector is counted as a lost particle. The east and west loss monitors are therefore set up in coincidence with a 40 ns time delay on the downstream detector to account for the time of flight of the particle across 12 meters.

If a discriminated signal of particle losses from both the east and west loss monitors is in coincidence, the output is sent to a frequency to voltage convertor yielding a loss rate in units of Hz. Since the detectors cannot count scintillator hits at a frequency which is higher than the 3.5 microsecond delay between bunch collisions, the highest rate for detecting particle losses is 280 kHz. The saturation level of the loss monitors used to measure particle losses discussed in this work, though, were set for a dynamic range of 100 kHz. This saturation level was chosen to give a good resolution signal for typical background loss levels during a store.

It would be difficult to estimate the absolute number of particles lost from a bunch using the loss monitor data. The loss monitor will give the same signal for one particle hitting the bunched beam counters (BBC) directly or for many particles hitting the BBC. The

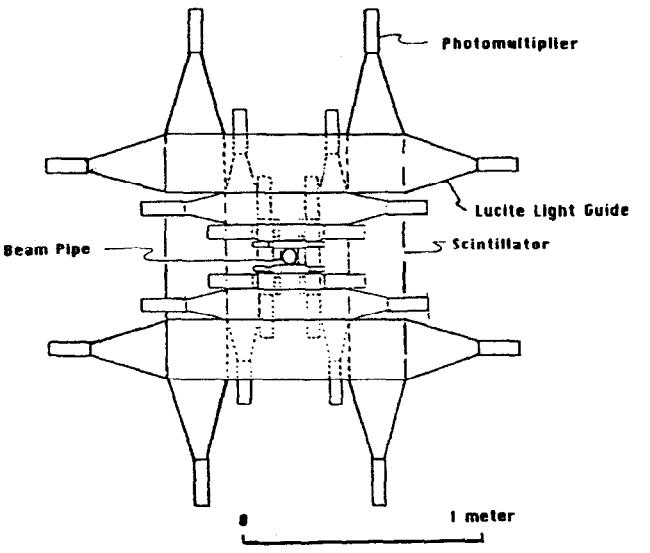

Figure 4.3: Transverse View of a Bunched Beam Counter at CDF.

discriminated signal does not provide sufficient information to calibrate the loss signal to the actual number of particles which hit the BBC. A statistical error estimate therefore becomes difficult. One can only measure background losses relative to stable or low loss operations. An estimate of the error in background losses is hence defined by the fluctuations in the readback of the background loss monitors during stable operations when the background losses remain relatively constant.

4.3 LUMINOSITY

The luminosity at the CDF and D0 interaction points is monitored using the bunched beam counters gated to detect inelastic collisions. The counters are gated to count as a collision only particles which arrive at the east and west counters within a gated window of time. At CDF, a 30 nsec gate centered around a 20 nsec (time of flight) delay after each proton/pbar bunch crossing is used to count collisions. The circuit is otherwise equivalent to the loss monitor circuit.

CDF used the experimental results of a measurement of the inelastic cross section at 546 GeV in the CERN UA4 detector to make an estimate of the inelastic cross section in the Tevatron.[50] Knowledge of the cross section enabled CDF to define a luminosity calibration. The inelastic cross section is estimated to be 46.8 mb for the BBCs, defining a luminosity of 1.0E30 $cm^{-2}sec^{-1}$ every 46.8 kHz. Since the typical luminosity for a given store is close to 5.0E30 $cm^{-2}sec^{-1}$, the signal from the luminosity monitor is typically much

higher than the background rate. The large count rate along with a known inelastic cross section enables a statistical error to be calculated. The statistical error is the square root of the number of collisions. The number of collisions (or counts in the monitor) is the measured luminosity multiplied by the calibration factor of (46.8 kHz /1.0E30 $cm^{-2}sec^{-1}$). When the statistical error in the measurement is compared with the fluctuations in the readback of the luminosity signal over a short period of time (to eliminate possible effects due to lifetime decays), it is found that the fluctuations in the readback of the monitor is the largest source of error in the measurement. This will be seen in more detail in the next chapter.

4.4 Bunch Intensities and Longitudinal Bunch Length

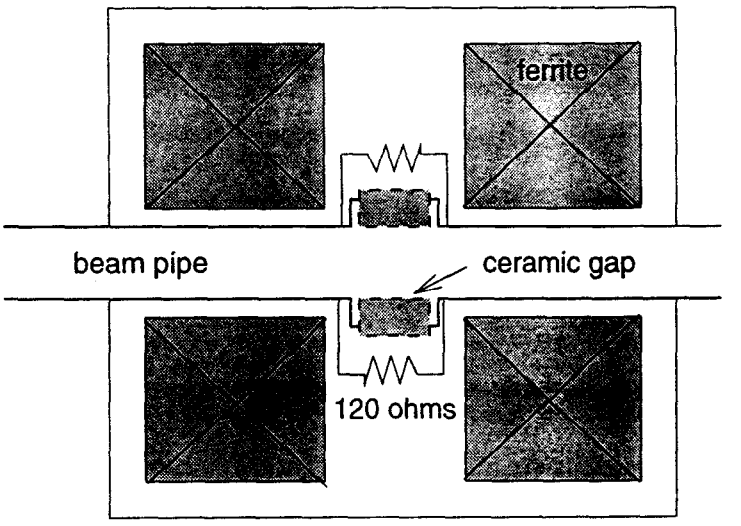

Figure 4.4: The Resistive Wall Monitor in the Tevatron.

The bunch intensity and the longitudinal bunch length of individual proton and antiproton bunches is measured using a fast sampling circuit known as the Sampled Bunch Display (SBD). The input signal of the SBD is the measured voltage across a resistive wall monitor in the Tevatron.

The resistive wall monitor is sketched in Figure 4.4. A 1 mm nonconducting gap between two beam pipe segments forces the image charge to follow a path of least resistance through a set of eighty 120 ohm resistors which are connected in parallel. A ferrite material surrounds the gap, providing a large inductance and preventing high frequency components of the current from travelling along the outer conductive casing of the resistive wall monitor.

The instantaneous voltage across the resistive wall monitor is fed into the SBD. The SBD utilizes a large bandwidth A/D oscilliscope capable of a sample speed of 0.5 ns. The

output signal of the SBD is as indicated in Figure 4.4.[53]

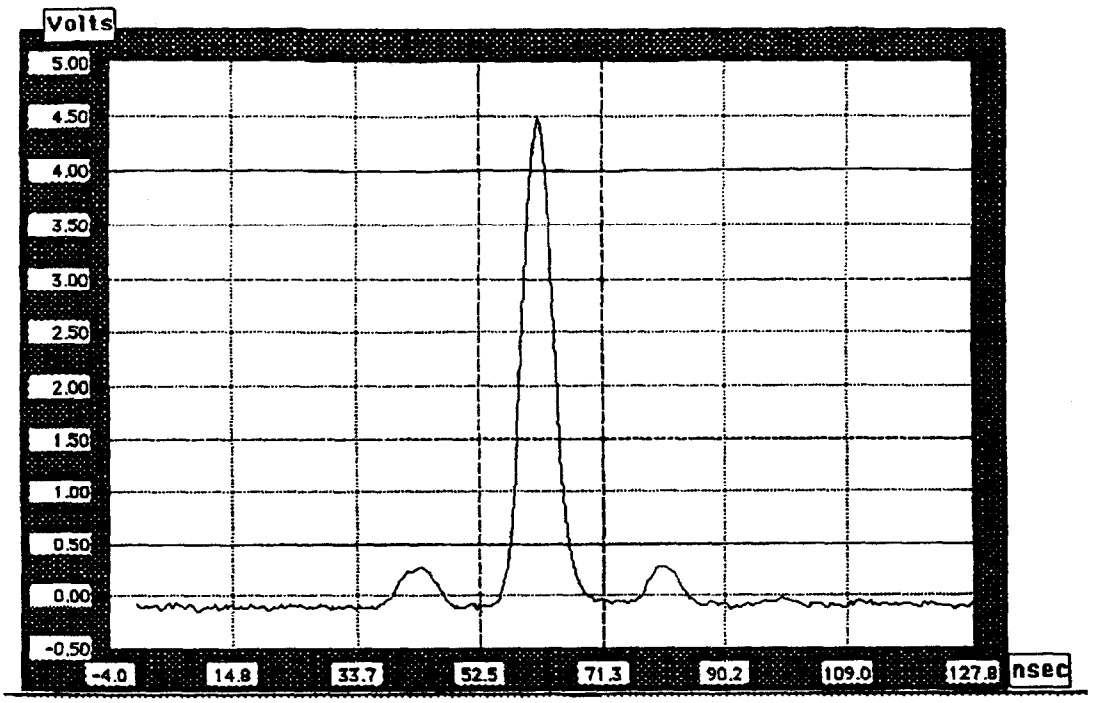

Figure 4.5: The Sampled Bunch Display. The 19 nsec divisions on the horizontal axis mark the edges of the main bunch and neighboring satellite bunches.

The rms of the distribution is the measured bunch length. An integration of the area of the distribution is the measured bunch intensity.

The precision of the SBD measurement is important for the calculation of luminosity using accelerator parameters.[50] A 5% uncertainty in the measured intensity of one bunch translates into a 10% uncertainty in the measured luminosity of two colliding bunches. In Collider Run IA, the agreement between the total bunch intensity measured by the SBD to the total DC current measured using a DC current transformer in the Tevatron was within approximately 5%. The precision of the SBD was improved during Collider Run IB.[53] The agreement between the SBD and the DC current transformer is now within 1%.[54]

The error in the measurement of the longitudinal bunch length is mainly due to limitations of the A/D oscilliscope.[51] It is estimated that the longitudinal bunch length error was of the order of 5% in Collider Run IA. The estimated error in the longitudinal bunch length using the Run IB SBD is approximately 3%.[54]

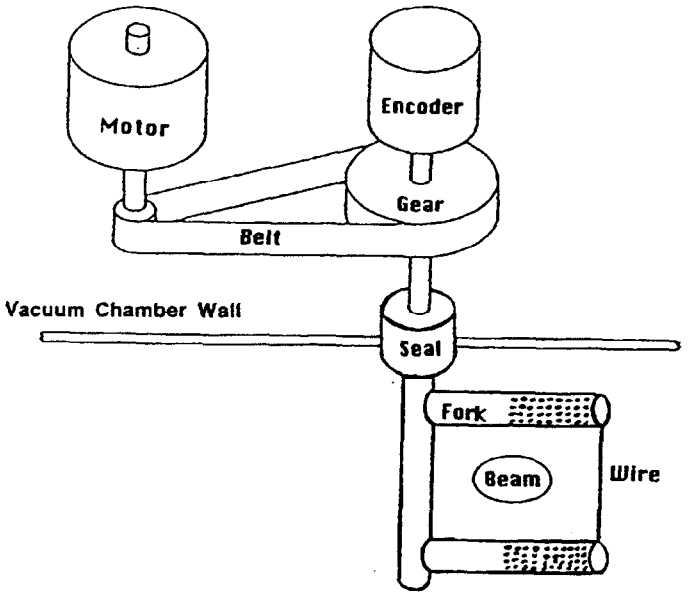

Figure 4.6: Sketch of a flying wire assembly.

4.5 Transverse Beam Sigma and Beam Emittance

The Flying Wires

As discussed in Chapter 2 (Equation 28), a measurement of the transverse beam size is necessary to calculate the invariant beam emittance. In the Tevatron, flying wires are used routinely to measure the transverse beam profiles in both the horizontal and vertical planes. A sketch of the flying wire assembly is shown in Figure 4.6.[55]

A flying wire is a 25 micron carbon filament which moves at a constant velocity through the passing proton and antiproton bunches. Scintillators, located downstream from the wires, detect secondary particles which are produced when a proton or antiproton collides with the wire. The scintillator is connected to a photomultiplier tube to measure the light intensity. A transverse beam profile is obtained by plotting the measured light intensity vs. the wire position. The rms of the light intensity data is then used as a measure of the Gaussian rms beam sigma.

Knowledge of the momentum spread of the bunch is also necessary to calculate the beam emittance at a non-zero dispersion location in the ring. Hence two flying wires are used in the horizontal plane, providing two simultaneous equations to solve for the unknown beam emittance and momentum spread. A typical profile obtained from the two horizontal and

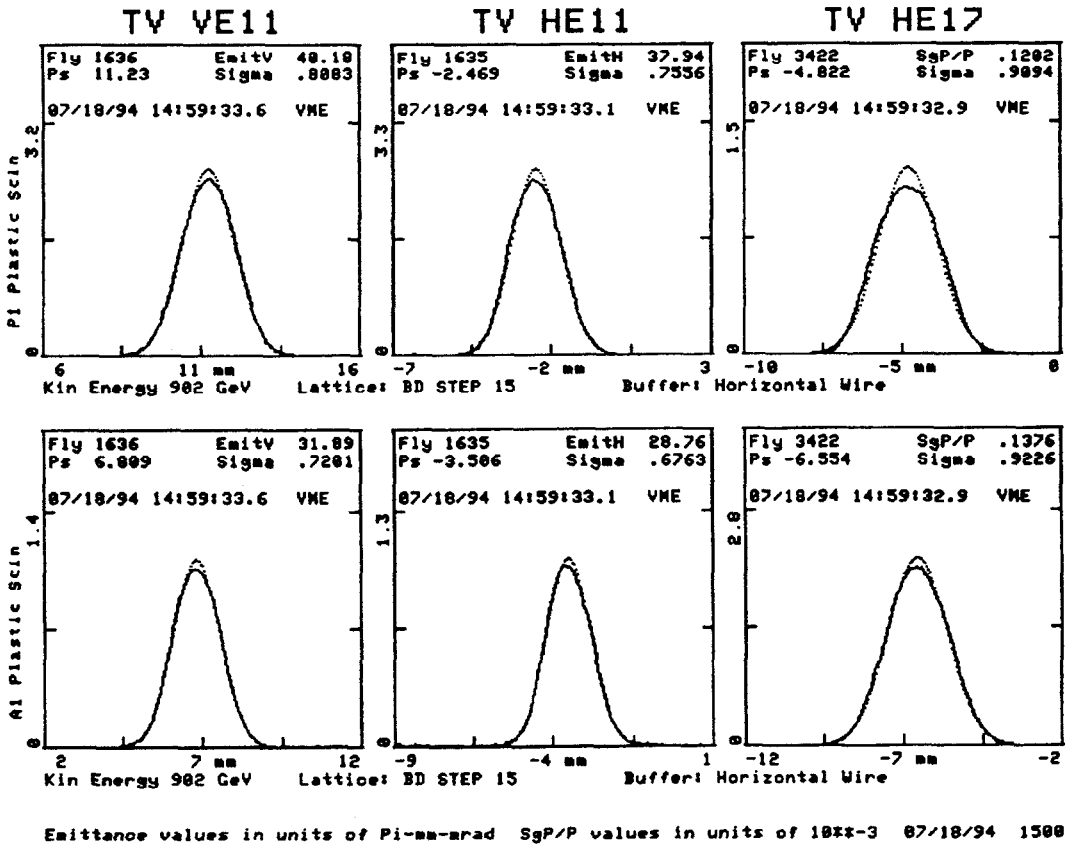

Figure 4.7: Transverse Profiles of a proton (top row) and antiproton (bottom row) bunch as measured by the flying wires. Light intensity vs. position are measured for the vertical (first column) and horizontal (second and third columns) planes. The solid line represents the measured data and the dashed line is a Gaussian profile corresponding to the rms of the light intensity data.

one vertical flying wire for a proton and antiproton bunch is shown in Figure 4.7. A Gaussian profile corresponding to the calculated rms of the data is plotted along with the measured light intensity.

The error in the flying wire measurement of sigma is difficult to estimate.[56] A discussion of some of the sources of calibration errors would include the following:

- The rms sigma of the transverse profile is found to be a function of beam position. The effect is estimated to produce a 5% to 10% variation in the calculated sigma.[57]

- The profile obtained in the Tevatron is dependent on the direction of the fly sweep. The calculated sigma from fly sweeps in the 'forward' and 'reverse' fly directions differ by approximately 3.0%.[58] The reason for this systematic error in the measurement is at present unknown.

The result of such a large uncertainty in the absolute calibration of the flying wire leads one to place importance on relative measurements of beam sigma only. Absolute measurements are difficult to realize. To compensate for the directional fly sweep problem, the average of two consecutive fly sweeps are used for every measurement of sigma in this work.

As Equation 2.28 indicates, the uncertainty of the measured beam sigma leads to an uncertainty in the measured beam emittance. This uncertainty is compounded by the difficulty in obtaining precise measurements of the beta function and the dispersion at the location of the flying wires.

THE SVX AT CDF

A measure of the transverse overlap of two colliding particle distributions at the B0 interaction region can be obtained using the silicon microstrip vertex detector (the CDF SVX).[59] The SVX is composed of 4 radial layers of silicon strips which surround the beam pipe as shown in Figure 4.8. It was designed to track in the cylindrical (r, ϕ) plane in order to link tracks in the Central Tracking Chamber to interactions occurring in regions close to the beam pipe. The SVX thus attempts to separate multiple interactions which may not be readily apparent in the Central Tracking Chamber.

The design of the SVX to make measurements in the (r, ϕ) plane gives it the capability of measuring the transverse overlap of colliding proton and antiproton bunches. In other words, the SVX is able to make a measure of σ in the luminosity relation

$$\mathcal{L} = \frac{N_1 N_2}{4\pi\sigma^2}. \tag{4.1}$$

Note that this luminosity relation is derived in Equation B.4 of Appendix B.

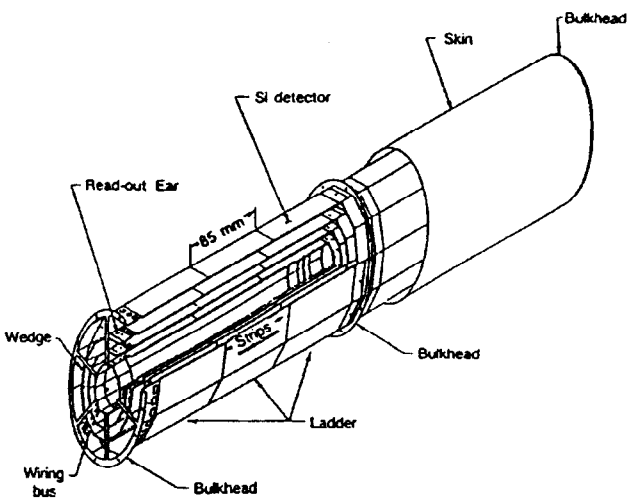

Figure 4.8: The SVX detector at CDF.

The SVX measures the rms transverse width of the luminosity distribution[60]. In terms of individual proton and antiproton bunch sizes, the SVX measures a σ_{rms} which is given by

$$\frac{1}{\sigma_{rms}^2} = \frac{1}{\sigma_z^2} + \frac{1}{\sigma_{\bar{z}}^2}, \tag{4.2}$$

where $z \equiv x, y$ refers to either the horizontal or vertical plane (see Figure 5.8, for example). The parameter σ_z is the bunch size of the protons and $\sigma_{\bar{z}}$ is the bunch size of the antiprotons. If an individual proton or antiproton bunch is assumed to be round ($\sigma_x = \sigma_y$) and the two colliding bunches are assumed to be of equal size ($\sigma_p = \sigma_{\bar{p}} = \sigma_{bunch}$),

$$\sigma_{rms} = \frac{1}{\sqrt{2}}\,\sigma_{bunch}, \tag{4.3}$$

where σ_{bunch} is the size of an individual bunch distribution. Under a round and equal colliding beam assumption, one can calculate σ of Equation 4.1 using the SVX measurement by simply multiplying the SVX results by $\sqrt{2}$.

$$\sigma = \sqrt{2}\sigma_{rms} \tag{4.4}$$

The measurement of σ_{rms} is statistical in nature and requires a few hours in order to measure the luminosity distribution within a few microns. It is not a routine measurement in the Tevatron, but it was used as an independent measure of the transverse overlap of colliding bunches in experiments discussed in the next chapter.

Chapter 5

BEAM-BEAM EXPERIMENTS IN THE TEVATRON

Section 5.1 presents, in some detail, the separators in the Tevatron and their measured ability to ensure that the centroids of proton and antiproton bunches are colliding with zero transverse separation and zero crossing angle at an interaction point. The latter part of Section 5.1 presents transverse overlap measurements at the B0 interaction point using the separators.

Several measurements were performed in the Tevatron in order to investigate detrimental effects of the beam-beam interaction. Section 5.2 describes the experimental procedure and measurements which identified beam-beam driven resonances. Section 5.3 presents experimental measurements of particle losses at various transverse beam separations near these resonances. Section 5.4 compares beam-beam simulations using a weak-strong model to the experimental results.

5.1 ORBIT CONTROL AT AN INTERACTION POINT

As discussed in Section 2.3, separators in the Tevatron provide the electrostatic kicks needed to separate proton and antiproton orbits at all locations where the two beams cross, except those at the B0 and D0 detectors. The resulting helical orbit scheme decreases unwanted beam-beam tune shifts and tune spreads which would otherwise cause a particle distribution to spread into dangerous areas of tune space. If the zero amplitude orbit of an antiproton is not offset from the centroid of the colliding proton distribution at B0 and D0, the collision is said to be head-on and the helix is correctly tuned. It will be seen in the next two sections that it is difficult to measure the separation between the two centroids of a colliding proton and antiproton distribution to better than a 0.03σ orbit offset.

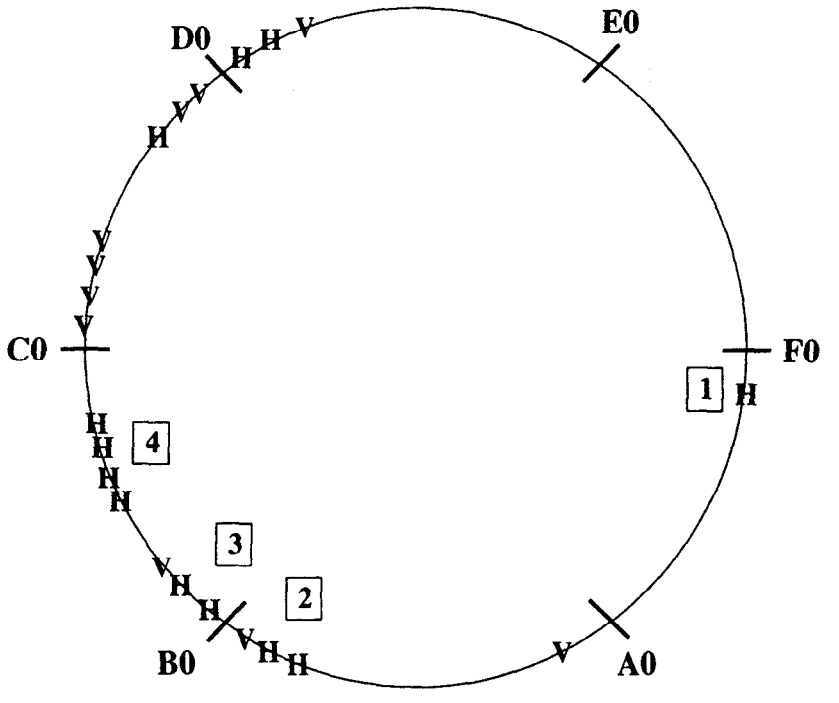

Figure 5.1: Sketch of the location of the separators in the Tevatron. The markers H and V indicate separators which deflect in the horizontal and vertical planes, respectively. The four squares labelled 1 through 4 denote separators used as elements in a horizontal four-bump across B0.

The closed orbit of protons and antiprotons are moved in opposite directions by the electrostatic kicks of the separators. If the resulting helix is not properly tuned, a separation or crossing angle will be present at an interaction point. The consequence of this is a decrease in the available luminosity. Tuning the helix in the Tevatron is accomplished using separator four-bumps. A separator four-bump creates an orbit distortion across an interaction point in order to control both the separation and the crossing angle of colliding beams. Two separators on each side of an interaction point are used as elements in the four-bump. The algorithm used to calculate the angular deflections of the separators is described in Appendix 1. Figure 5.1 sketches the location of the separators in the Tevatron. The separators used in a horizontal four-bump across the B0 interaction region are labelled in the figure. By constraining the outgoing angle and position of the closed orbit at the endpoints of the bump to zero, the four-bump remains a "local" bump; the closed orbit outside of the bump elements is unaffected by the bump.

The predicted orbit of a four-bump which changes only the crossing angle of colliding

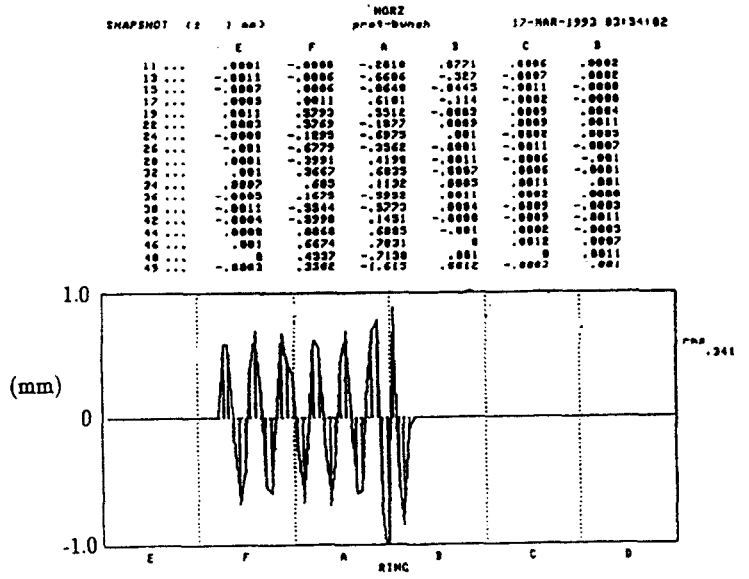

Figure 5.2: A model's prediction (*Tevconfig*) of beam positions in the Tevatron due to a crossing angle bump at B0.

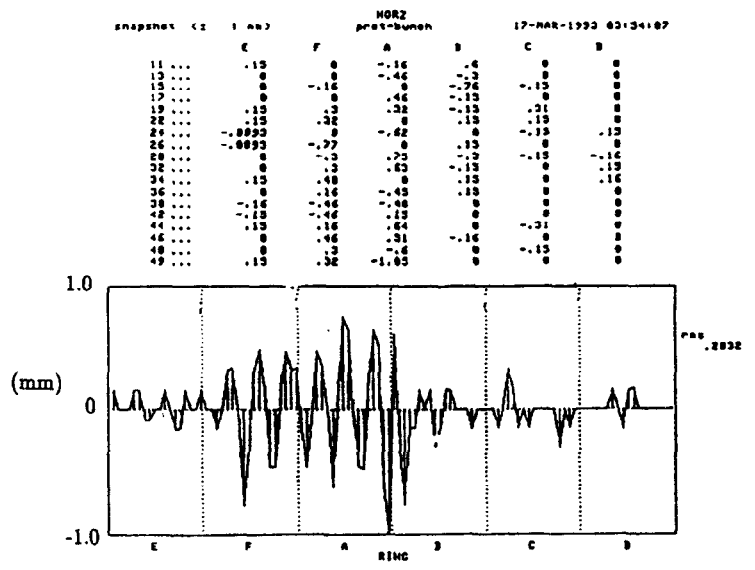

Figure 5.3: An orbit difference between two measured orbits in the Tevatron: a "four-bump on" minus a "four-bump off" orbit.

beams in the Tevatron is shown in Figure 5.2.[18] The four-bump introduces a full crossing angle of 120 μrad and zero separation at the B0 interaction point. This predicted orbit is compared to the measured proton orbit shown in Figure 5.3. Figure 5.3 is the difference between two measured proton orbits in the Tevatron; orbits with and without a 120 μrad crossing angle bump present. The orbit difference gives the beam positions due to the four-bump itself. A comparison of an orbit prediction using a model of the Tevatron and the measured orbit due to the crossing-angle bump shows good agreement. The rms deviation between the two orbits is 0.14 mm, which is within the 0.15 mm least count of the beam position monitors.

A prediction of orbit positions at the beam position monitors (BPMs) in the Tevatron due to a "separation bump" across B0 is shown in Figure 5.4. The four-bump introduces a separation in the colliding beams while constraining the crossing angle to zero. This predicted orbit is the result of a four-bump which creates a 0.1mm orbit displacement and a 0 μrad angle at the B0 interaction point. The separation of the bunches colliding at B0 is twice the magnitude of the orbit displacement or 0.2 mm. Two colliding bunches of 35 μm rms beam sigma, for example, would be separated by approximately six sigma. The predicted positions are shown ringwide in the upper plot of Figure 5.4 and are displayed for BPMs across the B0 straight section in the lower plot. It should be noted that the nature of a low beta insert requires that the phase advance between the separators closest to the interaction point is very close to π radians. Consequently, the orbit due to the four-bump closely resembles one obtained from a two-bump using only those separators. Also, note that the closed orbit at the D0 interaction point remains unaffected.

The separators in the Tevatron have an operating voltage limit of 125 kV per plate.[67] This limit corresponds to a maximum obtainable colliding beam separation of approximately five sigma in each transverse plane. As seen in Figure 5.4, the predicted beam positions throughout the ring for a separation bump of six beam sigma are less than the 0.15 mm least count of the Tevatron beam position monitors. It is therefore not possible to obtain a meaningful measured orbit in the Tevatron to compare with the predicted orbit of this separation bump, since the orbit changes are too small to be detected.

Luminosity vs. Separation and Crossing Angle

The separator four-bumps described in the previous section were used as a tool in controlling both the separation and crossing angle of colliding beams in the beam-beam experiments discussed in this work. By minimizing separation and crossing angle at an interaction

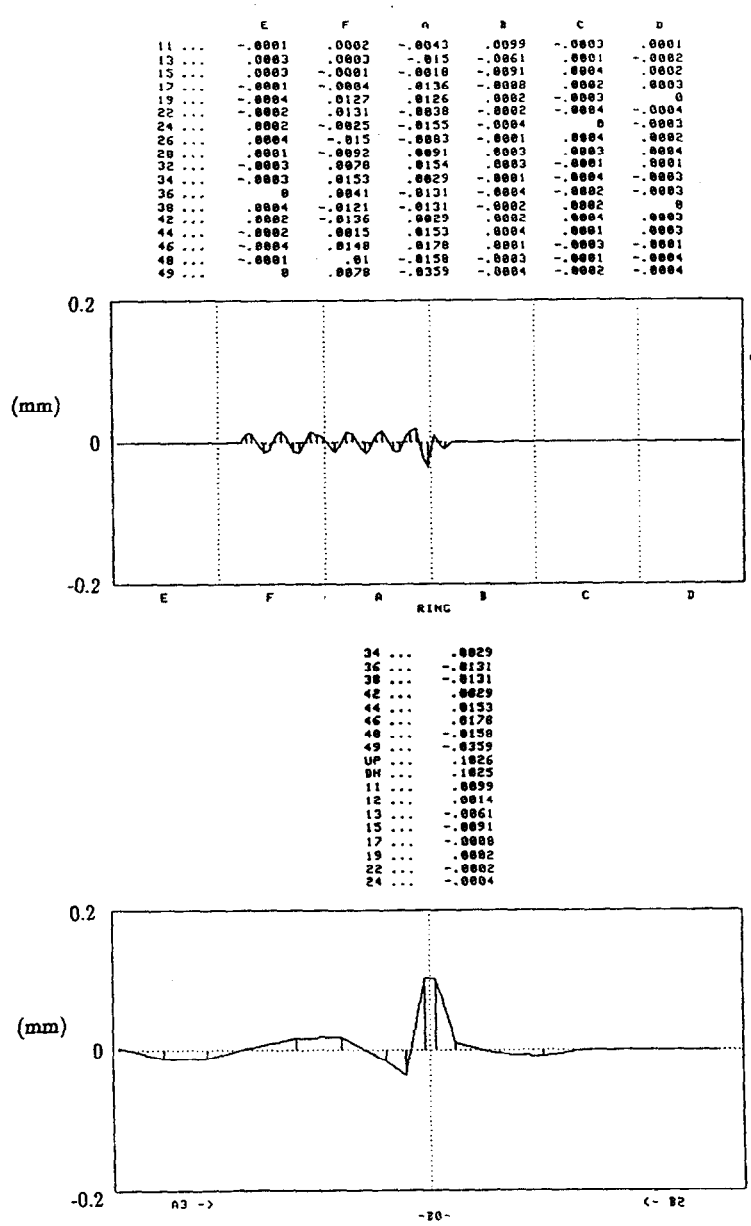

Figure 5.4: A model's prediction (*Tevconfig*) of orbit displacements at the BPMs in the Tevatron due to a separation bump at B0. The top picture plots ringwide positions while the bottom picture plots the predicted positions across the B0 straight section.

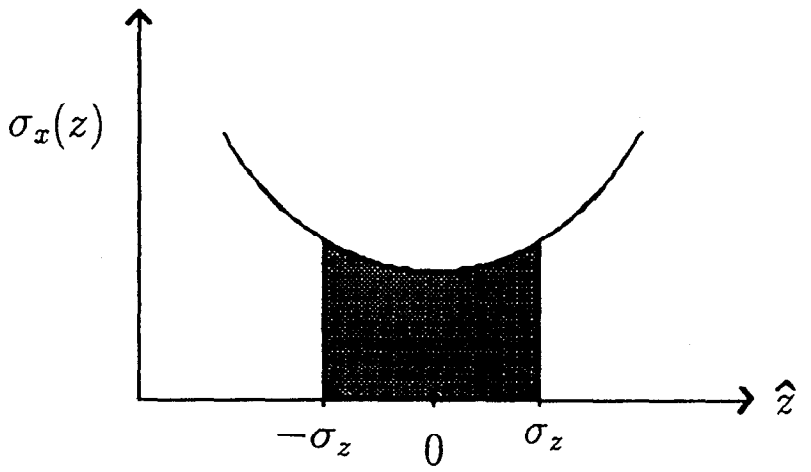

Figure 5.5: A qualitative sketch of the variation of transverse sigma of two colliding bunches in longitudinal space. The shaded area is the horizontal overlap defined within one longitudinal sigma.

point, the luminosity is optimized and a measure of how well "head-on collisions" are determined is obtained.[62][61]

As calculated in Appendix B, the Gaussian dependence of luminosity on a non-zero separation d in one transverse dimension is given by

$$L = L_0 \exp\left[\frac{-d^2}{2\sigma^2}\right]. \tag{5.1}$$

The standard deviation of the Gaussian dependence in the above expression is the convolution of individual proton and antiproton widths; $\sigma = \sqrt{\sigma_p^2 + \sigma_{\bar{p}}^2}$. Horizontal and vertical overlap are given by

$$\begin{aligned} \sigma_x &= \sqrt{\sigma_{p_x}^2 + \sigma_{\bar{p}_x}^2}, \\ \sigma_y &= \sqrt{\sigma_{p_y}^2 + \sigma_{\bar{p}_y}^2}. \end{aligned} \tag{5.2}$$

The simple sketch of Figure 5.5 gives a qualitative interpretation of what measured transverse overlap represents; the longitudinal dependence of the overlap of two colliding beams is accounted for in the measurement.

A longitudinal overlap of two colliding distributions is the convolution of individual bunch lengths and is given by

$$\sigma_z = \sqrt{\sigma_{p_z}^2 + \sigma_{\bar{p}_z}^2}. \tag{5.3}$$

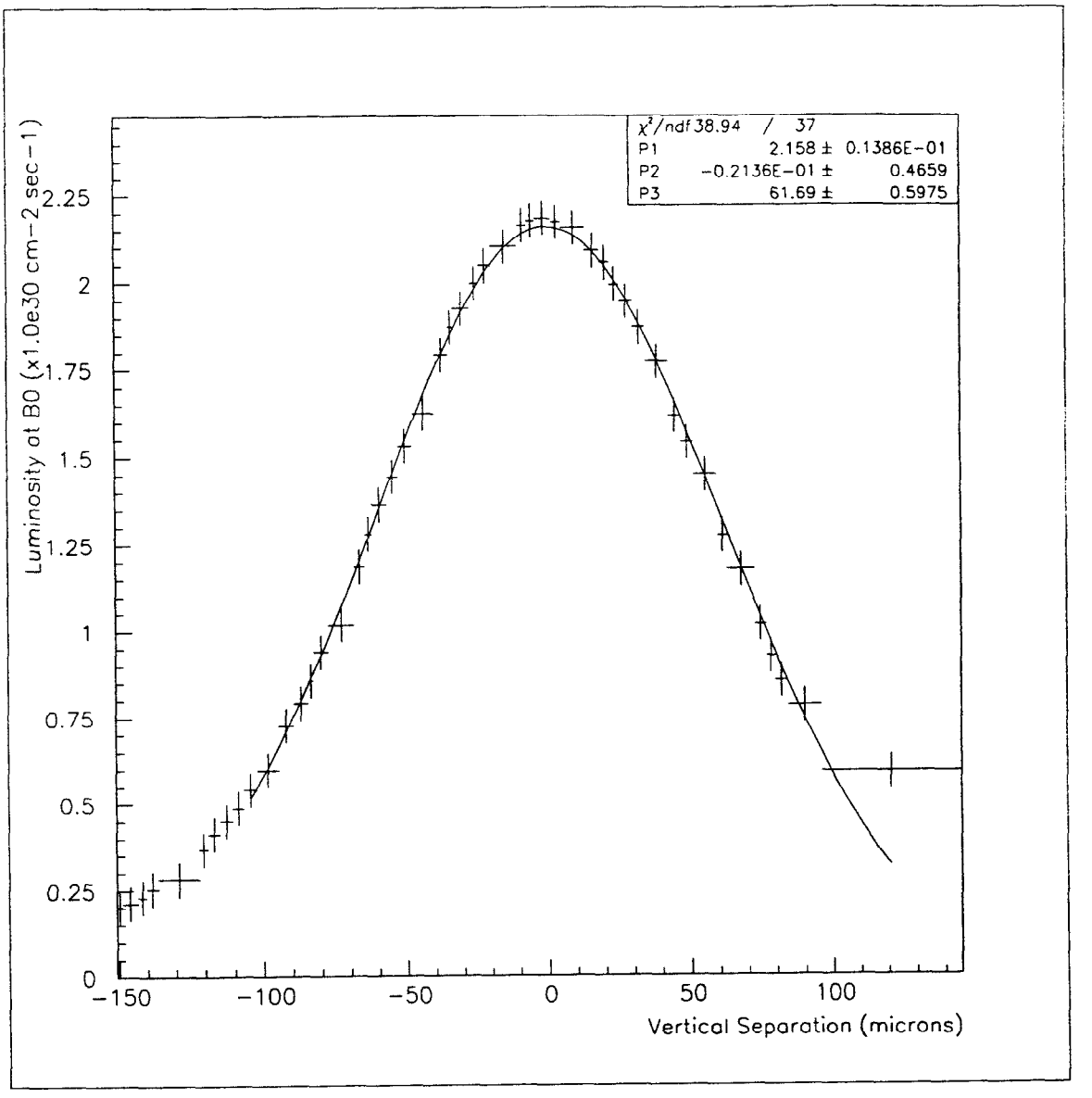

Figure 5.6: A MINUIT fit of measured luminosity vs. vertical beam separation at B0. The parameter P1 is L_0 of Equation 5.1 in $1e30\,cm^{-2}sec^{-1}$. The parameter P3 is the measured vertical overlap in μm. The error on the measured luminosity is $\pm 0.05e30\,cm^{-2}sec^{-1}$.

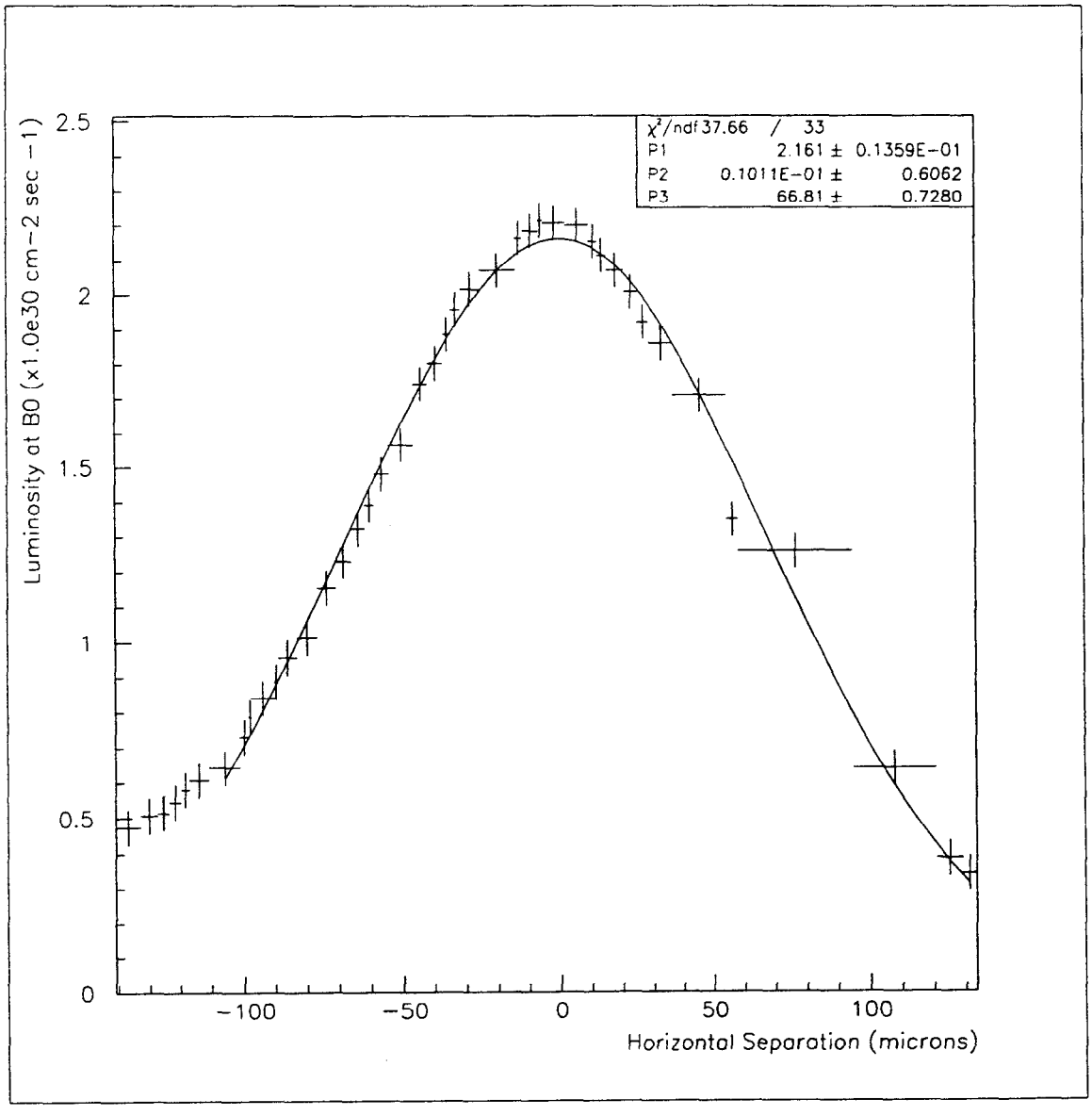

Figure 5.7: A MINUIT fit of measured luminosity vs. horizontal beam separation at B0. The parameter P1 is L_0 of Equation 5.1 in $1e30\,cm^{-2}sec^{-1}$. The parameter P3 is the measured horizontal overlap in units of μm. The error on the measured luminosity is $\pm 0.05e30\,cm^{-2}sec^{-1}$.

Data plotted in Figure 5.6 and Figure 5.7 are the result of typical "separation scans" in the vertical and horizontal planes. The separation scans were done at the end of a 6x6 (six proton bunches colliding with six antiproton bunches) store, so the transverse and longitudinal bunch sizes are large. The measured luminosity at the B0 interaction region is plotted as a function of transverse beam separation at B0. In the figures, horizontal and vertical beam separation corresponds to a voltage change in the horizontal and vertical separators at the A4 location, respectively. Equation A.13 of Appendix A is used to convert separator kV to μrads and then Equation 2.35 is used to translate the angular deflection into an orbit displacement.

The conversion factor from voltage on the A4 vertical separator to transverse separation of the centroids of the colliding proton and antiproton bunches is $4.6\mu m/kV$. Parameter P3 in Figure 5.6 gives a transverse vertical overlap of $61.7 \pm 1\mu$m. The conversion factor for the A4 horizontal separator is $3.9\mu m/kV$ which yields a horizontal overlap of $66.8 \pm 1\mu$m in Figure 5.7. The accuracy of the measurement in both planes is within approximately 0.03σ. If one assumes that the two colliding beams are round, an overlap of $64 \pm 1\mu$m corresponds to individual beam widths of $45 \pm 1\mu$m.

Note that a translation from kV to transverse beam separation requires knowledge of the lattice functions at the interaction point and at the separators. The lattice functions were obtained using a Tevtron model *Tevconfig*.[18] The lattice functions at the B0 interaction point are listed in Table 2.2. Separator lattice functions are listed in Table A.1.

Plane	ϵ_{N_p} (π mm-mrads)	$\epsilon_{N_{\bar{p}}}$ (π mm-mrads)	σ_z (cm)	$\sigma_{x,y}$ (μm)
Horizontal	28	19	70	68.2 ± 2
Vertical	28	17	70	68.0 ± 2

Table 5.1: Normalized emittance ϵ_N and longitudinal bunch length σ_z used in the calculation of σ_x and σ_y.

Flying wire profiles and longitudinal bunch length measurements enable a calculation of the luminosity using Equation B.12 in Appendix B. A Gaussian profile of luminosity vs. beam separation is obtained by calculating the luminosity at different beam separations in a given transverse plane. The standard deviation of the resulting Gaussian profile gives a calculated transverse overlap. Using this method, a horizontal overlap of $68.2\,\mu$m and a vertical overlap of $68.0\,\mu$m was found. Relevant measured parameters used in the calculation are listed in Table 5.1. The lattice functions used in the calculation were obtained from the

Tevatron model *Tevconfig*. This method is not strongly dependent upon accurate knowledge of the lattice functions. A 10% variation in the beta function at the interaction point gives a 3% variation in the calculated overlap. This error is reflected in the values of σ_x and σ_y in Table 5.1.

Agreement between an overlap measurement using separation scans and one using flying wires profiles to calculate the luminosity overlap integral is within 10%.

Method	$\sigma_x(\mu\text{m})$	$\sigma_y(\mu\text{m})$
Separation Scan	66.8 ± 1	61.7 ± 1
Profile Measurement	68.2 ± 2	68.0 ± 2
SVX	57.6 ± 1	63.2 ± 1
Crossing Angle	62.7 ± 9	-

Table 5.2: A comparison of transverse overlap measurements.

The SVX provides a completely independent measure of transverse overlap of colliding beams. An SVX measurement, occurring over a time span of approximately one and a half hours just prior to the above separation scans, measured an rms horizontal width of the luminosity distribution of $40.7 \pm 0.6\mu$m and an rms vertical width of $44.7 \pm 0.7\mu$m.[64] Using Equation 4.4, the rms widths correspond to a horizontal and vertical overlap of $57.6 \pm 0.9\mu$m and $63.2 \pm 0.9\mu$m, respectively. A fit of primary vertex data in each transverse plane to a Gaussian curve is shown in Figure 5.1. A three dimensional distribution of the luminosity as measured by the SVX is also displayed in Figure 5.9.

The discrepency between the horizontal separation scan and the SVX measurement of transverse overlap is approximately 16% while agreement in the vertical plane is approximately 2%. Further studies are required to discover the source of the discrepancy in the horizontal plane. The same lattice function dependence is used for the separation scans and the calculation of transverse overlap using flying wire profile measurements. The usefulness of the SVX measurement in this comparison is that it does not require knowledge of any lattice function.

As discussed in Appendix B, a one-dimensional dependence of the luminosity on a horizontal crossing angle, α_x, is given by

$$L = L_0 \frac{1}{\sqrt{1 + \left(\frac{\sigma_z}{\sigma_x}\,\alpha_x\right)^2}}. \tag{5.4}$$

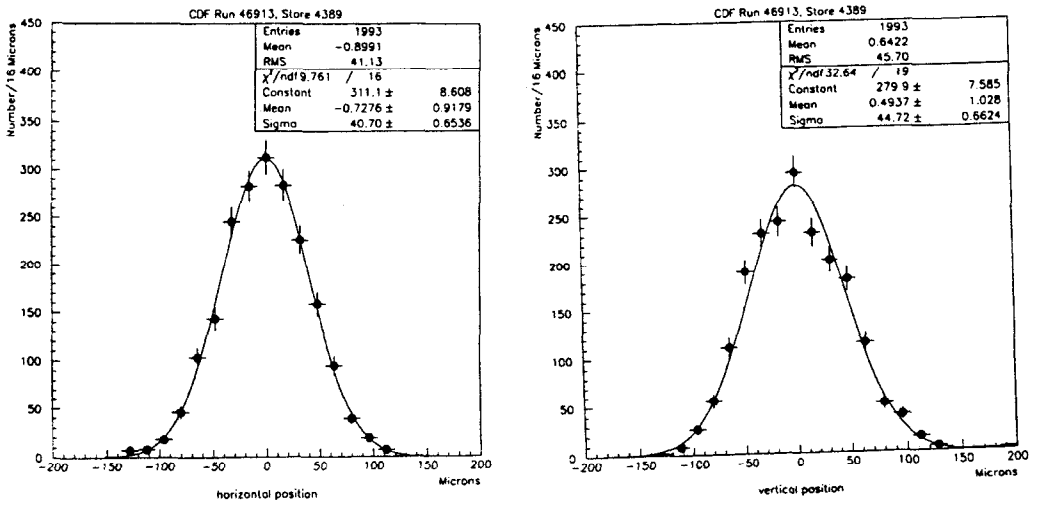

Figure 5.8: Primary vertex data as measured by the SVX at the B0 interaction point. By fitting the data to a Gaussian curve, a measure of the transverse overlap sigma is obtained.

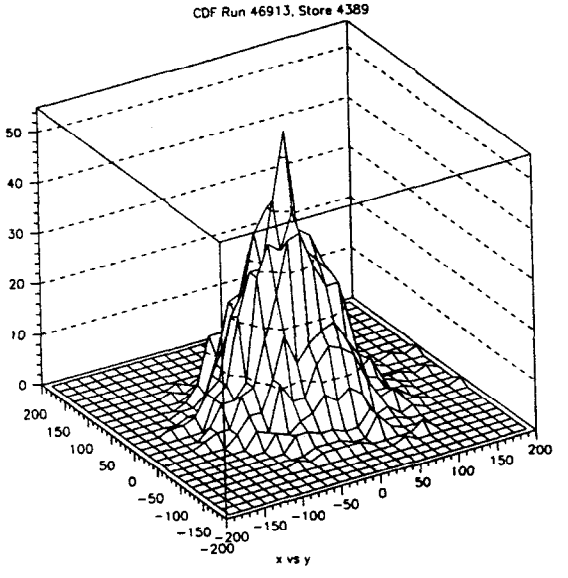

Figure 5.9: A three dimensional view of primary vertex data as measured by the SVX.

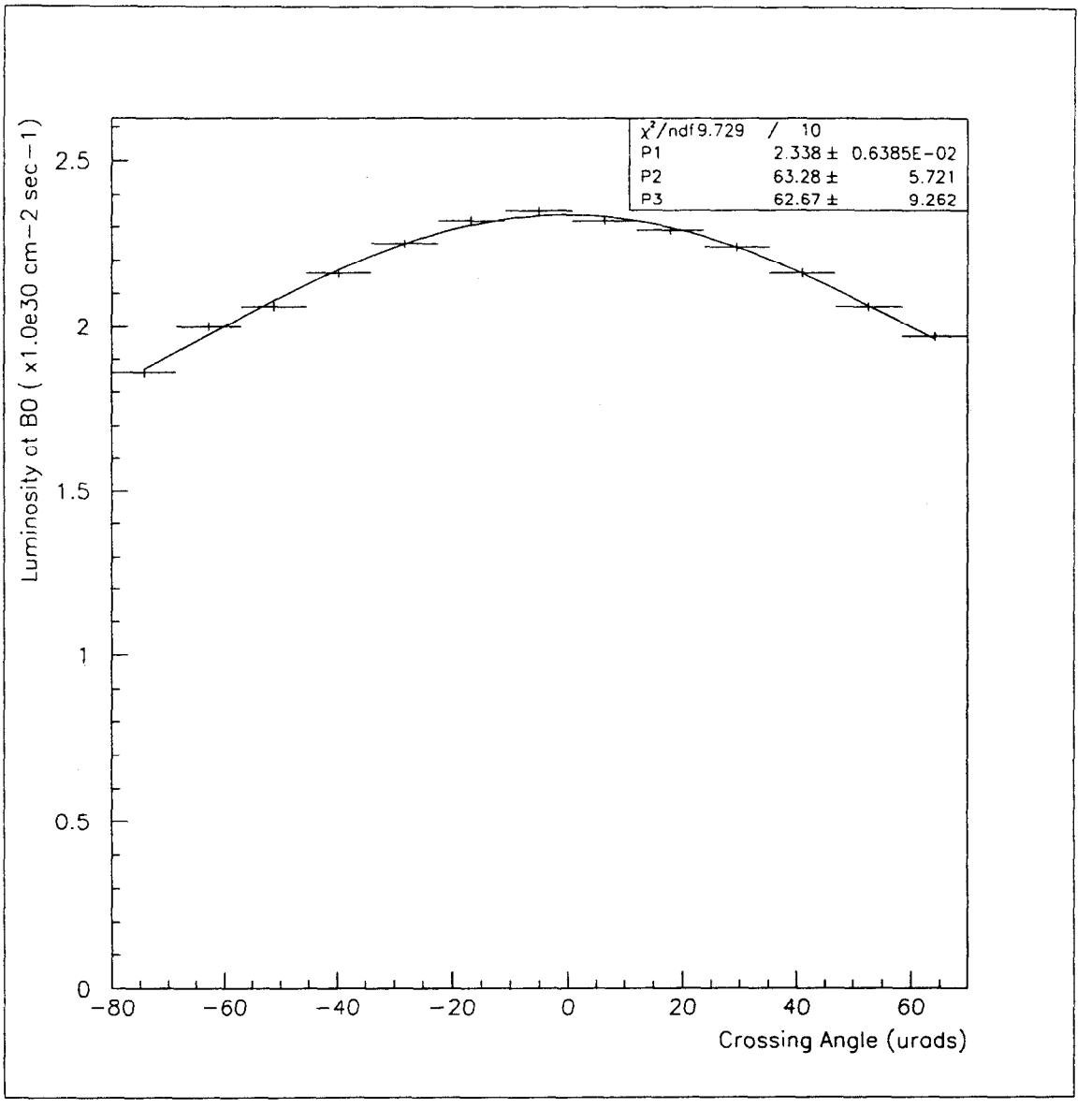

Figure 5.10: A MINUIT fit of measured luminosity vs. horizontal crossing angle of proton-antiproton collisions at B0. Note that the horizontal axis represents one half of the full crossing angle at the collision point. The parameters P1, P2, P3 are L_0, σ_z and σ_x, of Equation 5.4, respectively. The error on the measured luminosity is $\pm 0.014e30\, cm^{-2} sec^{-1}$.

A fit to a horizontal "crossing angle scan" is shown in Figure 5.10; the luminosity is measured as the horizontal crossing angle is varied. A measure of σ_x resulting from the fit is found to be $62.7 \pm 9\mu$m.

Table 5.2 summarizes a comparison of the different measurement techniques used to measure transverse overlap of colliding protons and antiprotons in the Tevatron.

The beam-beam experiments discussed in Section 5.3 and 5.4 use separation and crossing angle scans to control beam separation at the B0 interaction point. As seen in the above results, beam separation in these experiments is accurate to within 0.03 σ.

5.2 Identifying Beam-beam Driven Resonances

As shown in Figure 2.5, the Tevatron operates in a region of tune space which is bordered by fifth and seventh order resonances. The antiprotons are spread in tune space across twelfth order resonances due to the beam-beam interaction. In order to investigate which of these resonances are largely driven by the beam-beam interaction, particle losses were measured as the operating tune of the Tevatron was moved across these various ordered resonances.

A "tune scan" consisted of varying the operating tune by changing the correction quadrupoles in the Tevatron. The quadrupole current was ramped linearly in time between the endpoints of the tune scan sketched in Figure 5.11. The cross marks in the figure roughly designate the endpoints of the tune scans. A tune change of 0.061 tune units in Tune Scan B, for example, corresponded to a 3 amp linear ramp in the current of both the focusing and defocusing correction quadrupole circuits. As expressed in Equation 2.26, it is assumed that a linear change in the quadrupole current corresponds to a linear change in the proton tune. The tune was thus measured only at the two endpoints of the tune scan. The rate of change of tune with time was held constant at 0.01 tune units per minute.

In order to identify beam-beam driven resonances, it was necessary to compare background losses for colliding beams to background losses obtained when resonance lines were crossed with a single beam. Particle losses were measured while operating under both conditions: with protons only (6 proton bunches) in the Tevatron and also during a 6x6 colliding beam store.

Particle losses were measured using the most sensitive background loss monitors in the Tevatron, which are located at the CDF and D0 interaction regions. A comparison of typical loss patterns obtained at each interaction region during a diagonal tune scan (Tune Scan B of Figure 5.11) is shown in Figure 5.12. Loss monitors at D0 are located farther away from

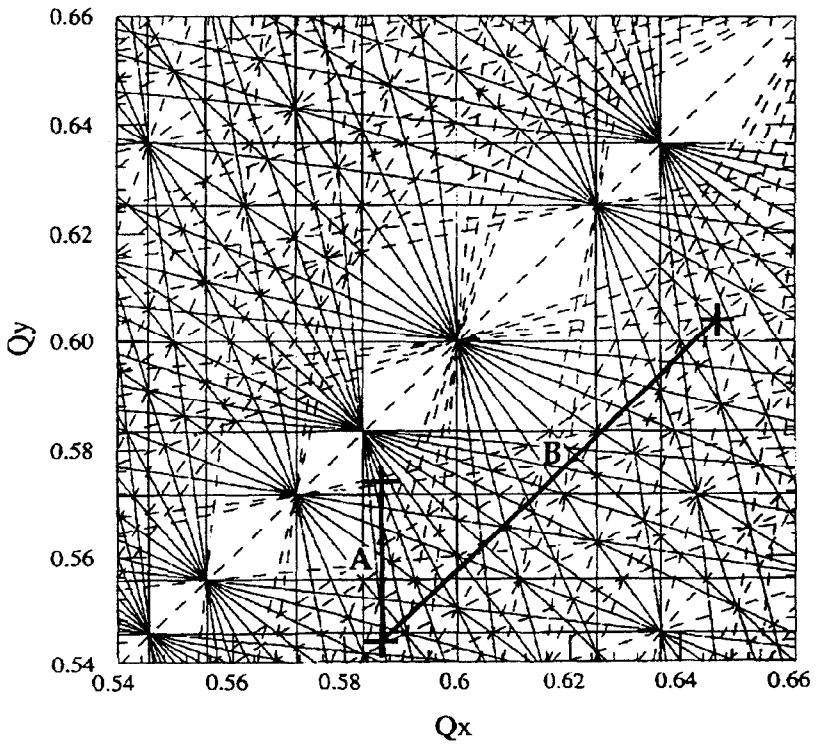

Figure 5.11: A map in tune space which sketches the endpoints and the change in the proton tune during tune scans experimentally performed in the Tevatron. Tune Scan A is a vertical scan crossing 7th and 9th order resonances. Tune Scan B is a diagonal scan which crosses a large number of resonances including 5th and 8th order resonances. Note that only the fractional part of the tune is plotted. The integer part of the tune in the Tevatron is equal to 20.

the beam pipe than the B0 monitors, so the D0 loss monitors do not saturate during the tune scan. In order to make a comparison of particle losses at the two locations, D0 losses are normalized to one of the B0 loss peaks. It can be seen that the loss patterns at both interaction regions are quite similar. This is indicative that losses during the tune scans are not occurring at one location only in the Tevatron. More particles are lost at points of maximum beta, where the beam envelope occupies the largest space in a given transverse dimension. In the Tevatron, a maximum beta of approximately 1100 m occurs at the low beta insertions located at B0 and D0. In the arcs of the Tevatron, the maximum beta is approximately 100 m.

Only a 5% decrease in proton and antiproton intensities occurred across the 7th and 9th order resonances of Tune Scan A. A larger decrease in particle intensities occurred during Tune Scan B, which crosses 5th and 8th order resonances. Proton and antiproton intensities

typically decreased by approximately 10% to 20% during Tune Scan B. The small number of particles lost while crossing lower ordered resonances such as the 5th order is due to the continuous change of the operating tune during a tune scan. The operating tune did not remain near a resonance long enough for larger particle losses to occur.

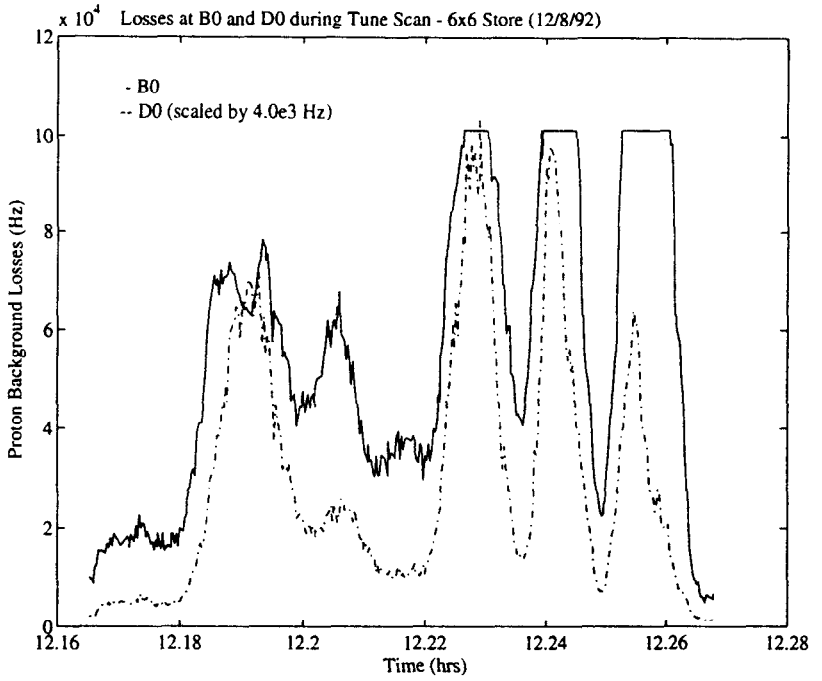

Figure 5.12: A comparison of measured background losses at the B0 and D0 interaction regions during a tune scan (Tune Scan B of Figure 5.11). The D0 background losses are scaled for the comparison. The B0 background loss monitors saturate at 10^4 Hz.

PROTON LOSSES DURING TUNE SCANS

Proton losses were used to identify beam-beam driven resonances during the tune scans of Figure 5.11. A comparison of proton losses from a proton only store and from a 6x6 colliding beam store for tune scans A and B are shown in Figures 5.14 and 5.13, respectively.

It is evident from the measured losses of Tune Scan B that the 5th and 8th order resonances are driven both by the Tevatron lattice itself and by the beam-beam interaction between colliding protons and antiprotons.

It is possible that proton losses which occur in the single beam case are due to the separated closed orbits in the Tevatron. Separated orbits cause a particle to receive non-linear kicks as it travels off-centered through magnetic elements and sees non-linear components of magnetic fields. It would be interesting to perform Tune Scan B with the separators off

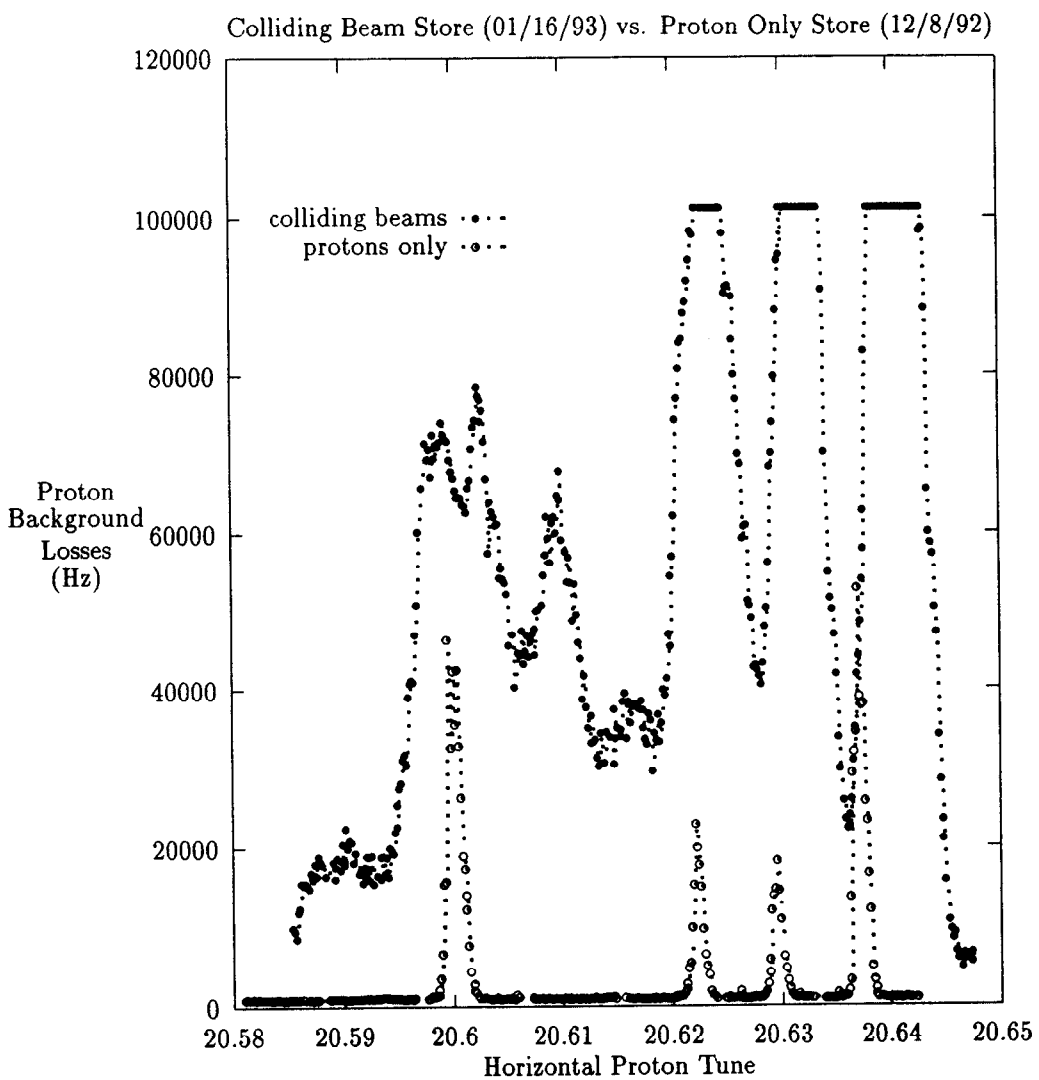

Figure 5.13: A comparison of proton losses measured at B0 while crossing the 5th and 8th order resonances (Tune Scan B of Figure 5.11) for protons only and for a 6x6 colliding beam store.

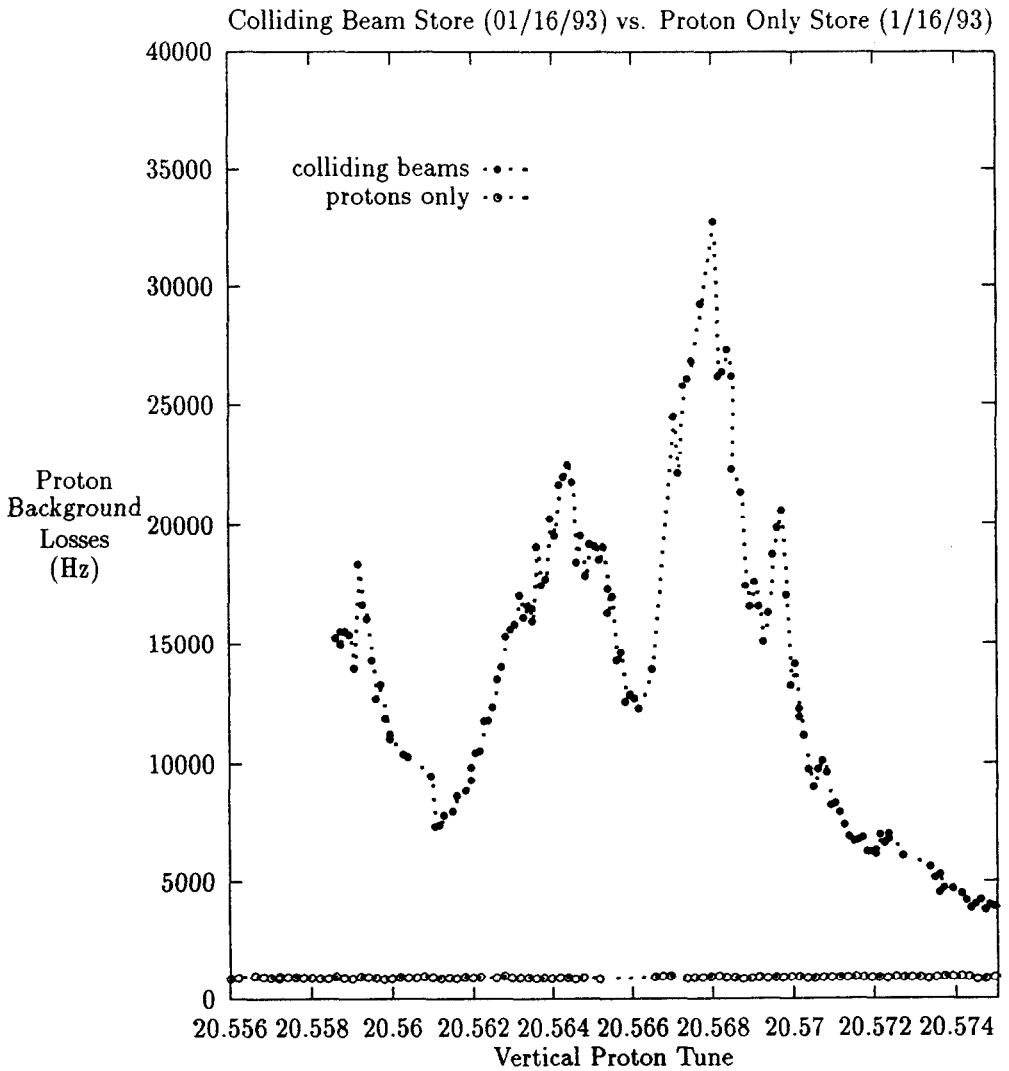

Figure 5.14: A comparison of proton losses measured at B0 while crossing 7th and 9th order resonances (Tune Scan A of Figure 5.11) for protons only and a colliding beam store.

to measure the effect of these non-linear kicks. At the time of this writing, it has not been determined what magnetic elements are driving 5th and 8th order resonances.

It is interesting to note that proton losses are negligible for the single beam case when crossing 7th and 9th order resonance lines in Tune Scan A. Only the colliding beam case is characterized by significant particle losses. This suggests that the 7th order resonance is a resonance which is at least initially driven only by the beam-beam interaction in the Tevatron. Once a particle's amplitude grows due to the nonlinearities of the beam-beam interaction, it can be lost because of non-linear kicks it receives from elements in the lattice itself.

The observation that an odd-ordered component of the beam-beam driving force caused significant particle losses in the Tevatron led to an investigation of how well the beams were colliding. As stated in Section 3.1, if two particles are colliding head-on, the beam-beam potential is an even function in both transverse dimensions. Only even-ordered resonances are expected to be driven by the beam-beam interaction when collisions are head-on. Indeed, a 50 μrad crossing angle at the B0 interaction region was discovered and removed due to this observation. After the crossing angle at B0 was corrected, particle losses were low in Tune Scan A. This observation suggests that 7th order resonant excitation was removed and only 14th order resonant effects were observed when the helix was properly tuned. Correcting the crossing angle at the B0 collision point led to a 5% increase in the luminosity.

5.3 Investigating Beam-beam Driven Resonances as a Function of Beam Separation

Experimental results of particle losses as a function of proton tune for various transverse separations of two colliding beams are presented. The first section describes measurements taken during Collidier Run IA. Problems with this measurement procedure and the experimental results during this experiment are discussed. The experimental procedure was improved and the experiment repeated in Collider Run IB. The second section presents measurements taken during Collider Run IB. The third section presents a comparison of the experimental results of Collider Run IB with simulation results.

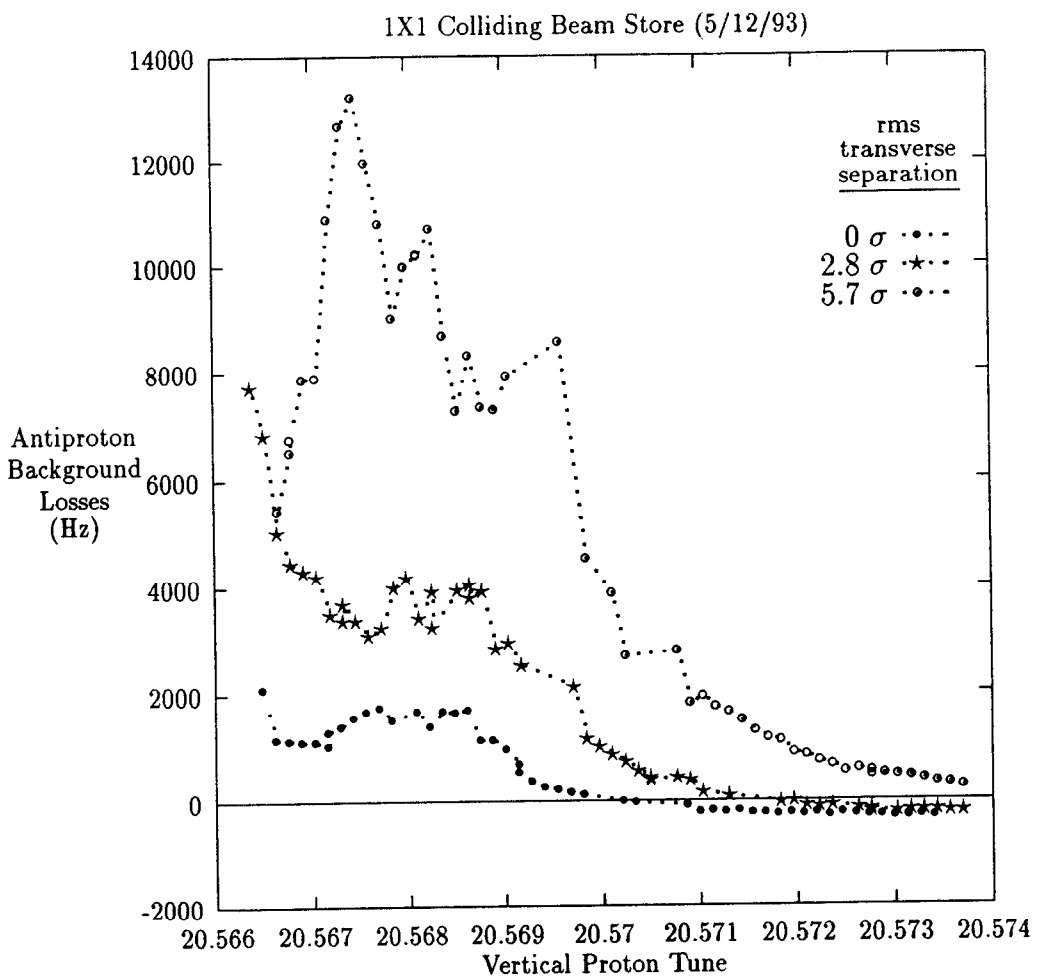

Figure 5.15: Background Losses as a function of vertical proton tune for three tune scans done at three different transverse separations of the centroids of the colliding proton and antiproton bunches.

COLLIDER RUN IA - A BEAM-BEAM EXPERIMENT AND PROBLEMS WITH THE MEASUREMENT

A 1x1 store (one proton bunch colliding with one antiproton bunch) was utilized to measure particle losses in the Tevatron as a function of different transverse beam separations. The two bunches were set to cross at the B0 interaction point and consequently crossed again at the opposing E0 straight section. The operating tune was moved across 7th and 9th order resonances as in Tune Scan A of Figure 5.11. The tune was changed linearly in time during the tune scans, that is, the correction quadrupoles were ramped smoothly between two endpoints. Each tune scan represented different transverse beam separations of the colliding protons and antiprotons at the B0 interaction point. The orbits of the antiprotons and protons were separated at the interaction point using separation four-bumps. The results of the measurements of particle losses is shown in Figure 5.15.

The results of the loss measurements were puzzling in that regardless of the tune, antiproton losses were largest under conditions when the bunches were fully separated at 5.7σ. Since the beam-beam kick at such a large separation is much smaller than at intermediate separations, these results aroused some suspicion in the measurement procedure. The dynamically changing tune was thought to have caused a non-equilibrium situation in particle losses.[65] A beam-beam experiment performed in the SPS at CERN in 1989 had in fact seen such a non-equilibrium behavior in the background rate. SPS experimenters described particle losses due to a 13th order resonance as suddenly increasing as the tune was changed and then settling to a new equilibrium value with a time constant of many seconds.[25]

Particle loss behavior as a function of tune was thus investigated in another 1x1 store. Figure 5.16 displays a confirmation of this non-equilibrium behavior of particle losses. As the tune (correction quadrupole current) is changed, both the antiproton and proton losses are seen to increase significantly. After a period of time of the order of minutes, this initial rise in the losses settles down to a new equilibrium value which more accurately describes particle losses at the new tune.

Confirmation of the non-equilibrium behavior of particle losses as the tune was changed led to a modification in the experimental procedure in proceeding beam-beam experiments. In order to eliminate measuring particle losses which resulted solely from the slew rate of quadrupole currents, the operating tune was moved across 7th order resonances in discrete steps. Particle losses were measured after a stable tune setting was reached and equilibrium values of particle losses became apparent.

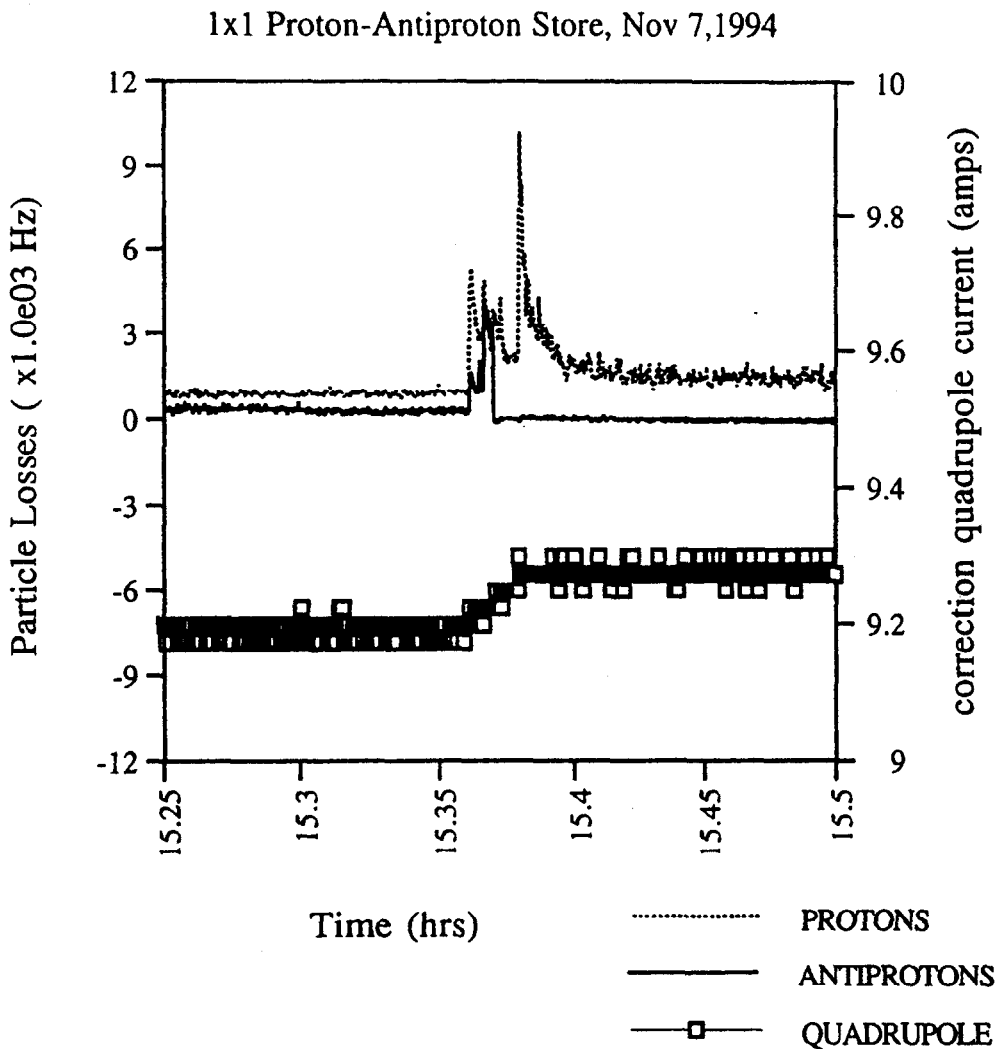

Figure 5.16: Particle losses during a change of tune. The non-equilibrium value of the losses during a tune change is apparent.

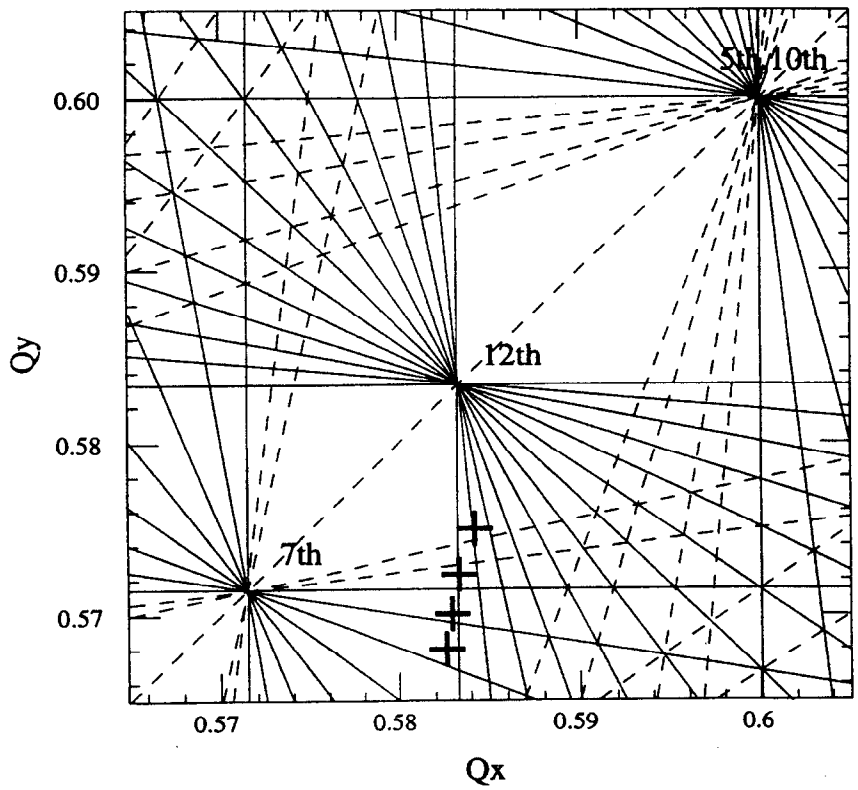

Figure 5.17: Tune diagram marking the proton tune settings where particle losses were measured during the beam-beam experiment discussed in Section 5.3.2.

COLLIDER RUN IB - MEASUREMENT OF PARTICLE LOSSES AS A FUNCTION OF TRANSVERSE BEAM SEPARATION

A 1x1 store was utilized to measure particle losses driven by the beam-beam interaction as a function of transverse beam separation. The antiproton and proton bunch were set to cross at the B0 interaction point and consequently crossed again at the opposing E0 straight section. The operating tune was moved across 7th order resonances in four discrete steps. The points in tune space in which losses were measured are shown in Figure 5.17.

Figure 5.18 is a close-up of Figure 5.17 which labels each tune setting and depicts a measured tune error of ± 0.0003 in both the horizontal and vertical planes. This tune error is the standard deviation of four tune measurements taken for four different beam separations at the same proton tune setting. The measured proton tune for the four measurements are listed in Table 5.3.

Measurement #	Horizontal Tune	Vertical Tune
1	20.5837	20.5753
2	20.5828	20.5727
3	20.5824	20.5704
4	20.5821	20.5683

Table 5.3: Measured proton tune as marked in Figure 5.18.

Because of the transient behavior of particle losses during a tune change (as discussed in Section 5.3.1), measurements of particle losses were taken only after losses reached an equilibrium value after a tune change.

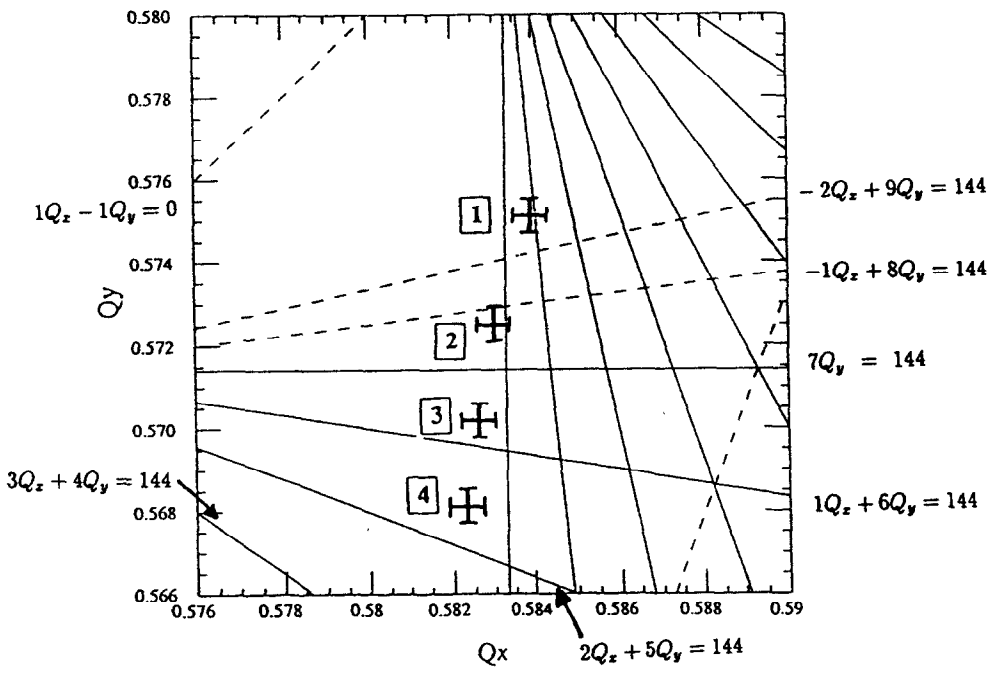

Figure 5.18: A close-up of Figure 5.17 which depicts the measured uncertainty in the proton tune and assigns labels to the four measurement points.

Figures 5.19 and 5.20 display antiproton and proton losses as a function of vertical proton tune. Each symbol in the figures represents a different beam separation at the B0 interaction point. Beam separation is measured in units of transverse rms sigma of the proton bunch and is denoted by σ. An rms separation d is given by

$$d = \sqrt{d_x^2 + d_y^2}, \tag{5.5}$$

where d_x denotes horizontal separation and d_y denotes vertical separation. The beams were separated equally in each plane by 1σ, 2σ and 3σ, yielding an rms beam separation of 1.4σ, 2.8σ and 4.2σ, respectively. The transverse size of the proton bunch at B0 was calculated using Equation 2.28. Normalized proton emittances obtained from flying wire measurements were 16π mm-mrads in the horizontal plane and 18π mm-mrads in the vertical plane. The lattice functions used in the calculation of proton sigma at B0 are listed in Table 2.2. The transverse proton sigma is found to be 32 μm in the horizontal plane and 33 μm in the vertical plane.

Separation bumps which are discussed in Section 5.1.1 were used to separate the beams at B0. A B0 separation bump does not affect the orbit at E0, so separation of the proton and antiproton bunch at E0 remained constant. Beam separation at E0 is estimated to be 2.6 σ in the horizontal plane and 4.9 σ in the vertical plane. The rms beam separation at E0 was thus approximately 5.5 σ.

The error in particle losses is a reflection of the fluctuation of losses during the measurement; each error bar represents the standard deviation of particle losses over a four to five minute period.

Note that both proton and antiproton losses for head-on collisions at all tune settings are minimal. This observation was used to maintain the same initial conditions for each measurement. After particle losses were observed for a given tune at a given separation, separation bumps were removed and collisions at B0 returned to head-on collisions. At these low loss conditions, collimators were moved into the beam in order to scrape the beams and remove any tails on the distribution of both the proton bunch and antiproton bunch which may have developed. In this way, transverse beam blow-up was eliminated and initial proton and antiproton emittances remained constant throughout the experiment. Bunch intensities did decrease significantly at times, but the ratio of particles per bunch between the proton and antiproton bunches remained constant at approximately a 2:1 ratio. Table 5.4 lists initial proton and antiproton bunch intensities for each measurement.

In order to examine what beam-beam resonant driving terms are driving particle losses in the experiment, one must examine more carefully what amplitude particle the measured proton tune spectrum represents. As discussed in Section 4.1, the magnitude of the power spectrum obtained from the Tevatron Schottky detectors indicates that the signal is due to a coherent motion of protons. Since the motion is coherent, the power spectrum represents an oscillation of the entire proton distribution. More protons exist at small amplitudes, thus it is assumed that the peak signal in the measured proton tune is due mainly to small amplitude

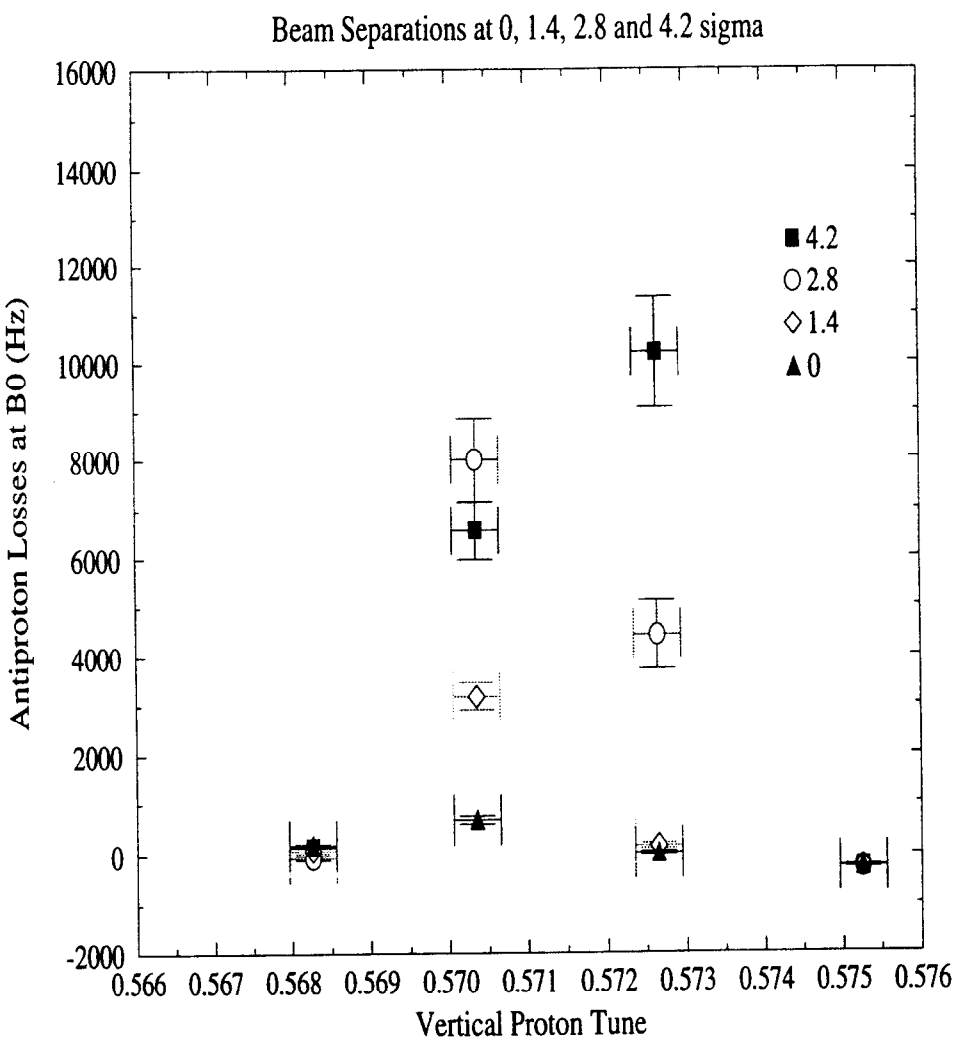

Figure 5.19: Antiproton background losses at B0 when the proton tune is near the 7th, 9th and 11th order resonances of Figure 5.18. Each symbol represents a different proton-antiproton bunch separation at B0.

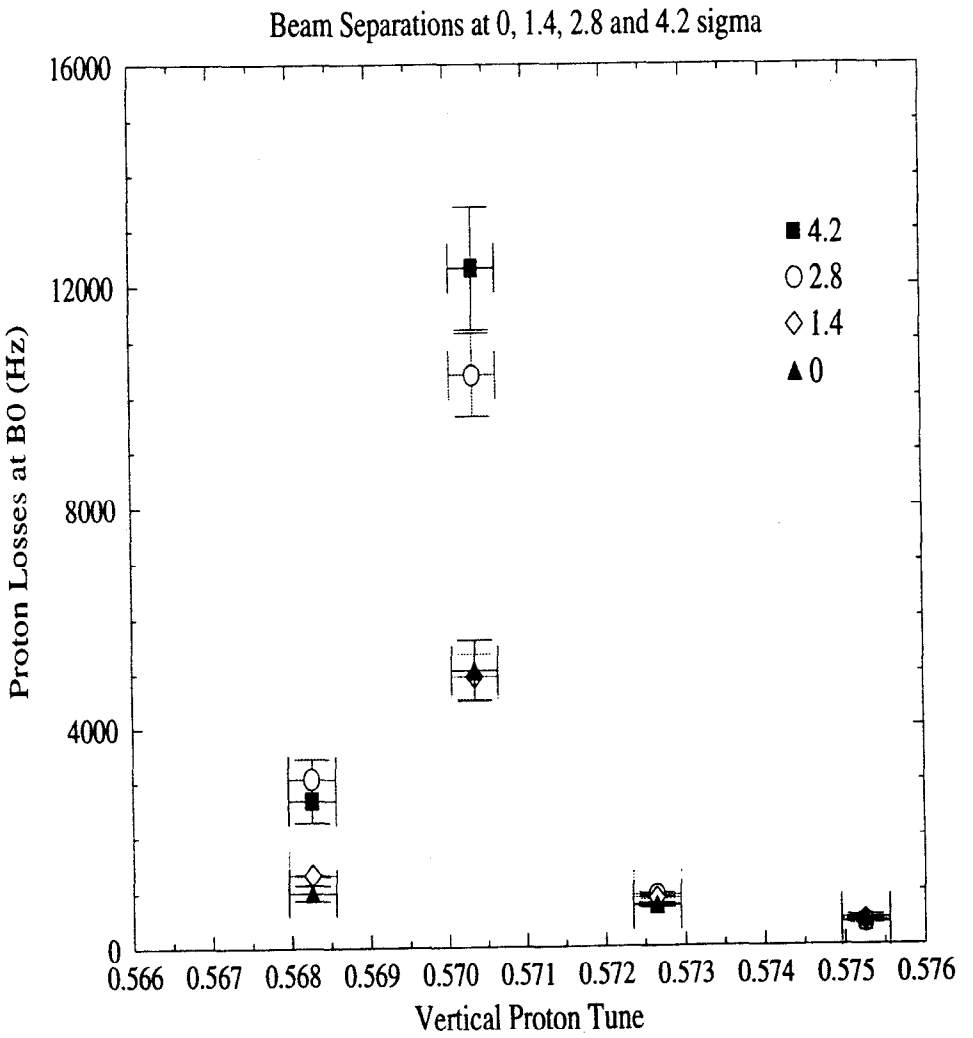

Figure 5.20: Proton background losses at B0 when the proton tune is near the 7th, 9th and 11th order resonances of Figure 5.18. Each symbol represents a different proton-antiproton bunch separation at B0.

protons. The linear tune shift of the small amplitude protons due to beam-beam collisions with the antiprotons must be taken into account.

Initial Proton and Antiproton Intensities (x1.0×10^9)

Vertical Proton Tune	Beam Separation							
	0σ		1.4σ		4.2σ		5.7σ	
	p	$\bar{p}$	p	$\bar{p}$	p	$\bar{p}$	p	$\bar{p}$
20.5753	125	52	125	52	125	52	125	50
20.5727	123	50	122	50	115	45	110	45
20.5704	105	45	100	45	90	40	80	35
20.5683	59	30	58	30	56	30	54	30

Table 5.4: Bunch intensities during beam-beam experiments. Uncertainty in the bunch intensities due to signal fluctuations is approximately 5%.

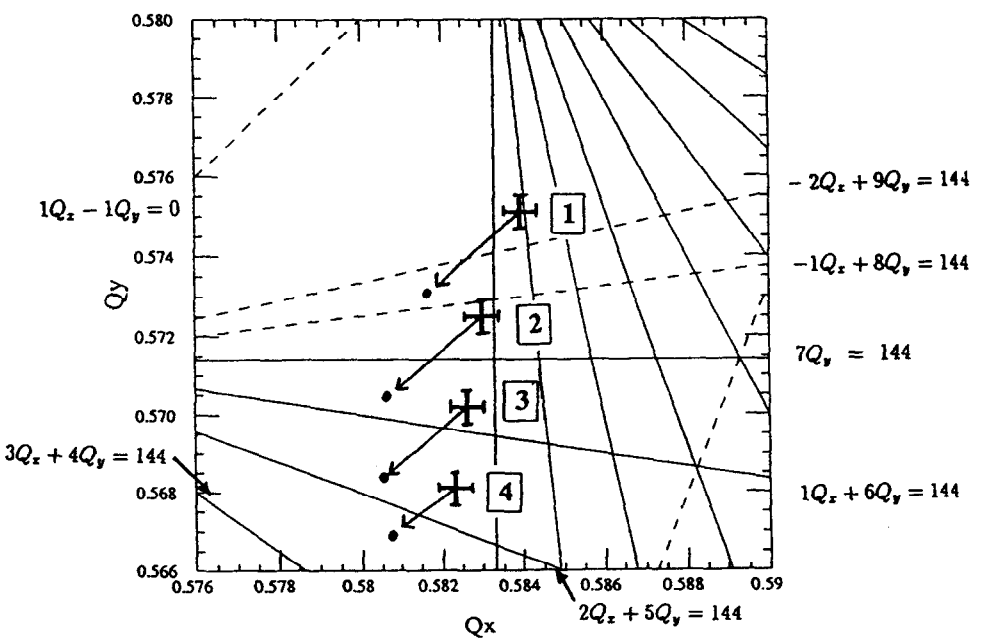

Figure 5.21: Tune diagram marking the measured proton tune settings (crossmarks) of the beam-beam experiment and the base tune (dots) of particles which are unperturbed by the beam-beam interaction. In the beam-beam experiment, protons and antiprotons are spread in tune from the base tune settings.

For the beam intensities listed in Table 5.4 and a beam emittance of 16πmm-mrads, the proton linear tune shift is approximately 0.002. In this work, the tune of a particle if no

beam-beam interaction is present is defined as the base tune. The base tune of both the protons and antiprotons is thus shifted down and to the left from the measured proton tune of Figure 5.18. This tune shift is taken into account in Figure 5.21. The measured proton tune, designated by the crossmark in Figure 5.21, corresponds to a base tune represented by the dot.

Some interesting observations are made from the experimental results plotted in Figures 5.19 and Figure 5.20. Measurement 1 in Figure 5.18 marks the nominal operating point in the Tevatron; protons and antiprotons are spread in tune across 12th order sum resonances and are in between a 9th and 11th order difference resonance. At this tune setting, antiproton and proton losses are minimal for head-on collisions and for separated beams. No beam-beam driving terms are observed to strongly drive 12th order resonances or the 9th and 11th order difference resonances. The experiments above do not address any beam-beam interaction effects on particle lifetimes due to the 11th and 12th order resonance driving terms. Further measurements are necessary to measure particle lifetime effects.

The presence of beam separation is seen to excite odd-ordered sum resonances. At measurement 2 in Figure 5.18, the base tune is close to two 7th order difference resonances: $(1Q_x + 6Q_y)$ and $(7Q_y)$. Antiproton losses at this tune setting increase as beam separation at B0 is increased. Antiproton losses are highest at a beam separation of 4.2σ. An increase of particle losses in the presence of separated beams is also apparent when the tune is near the $(2Q_x + 5Q_y)$ sum resonance (measurement 3 in Figure 5.18). Antiproton losses increase until the beams are separated by 2.8σ and then start to decrease at larger separations. Proton losses are still increasing at a beam separation of 4.2σ at this tune setting. Proton losses are significant only near this 7th order sum resonance, but remain relatively low elsewhere.

Particle losses are minimal for head-on collisions and for separated beams at measurement 4 in Figure 5.18. The bunch intensities during this measurement were very low (proton intensity $< 60 \times 10^9$). It will be shown in the next section that the beam-beam tune spread of the antiprotons was small enough that particles did not cross any dangerous resonances at this tune setting and with such low bunch intensities.

The most important observation relevant to this dissertation is that no clear pattern of particle losses as a function of beam separation due to odd-ordered beam-beam resonant driving terms is apparent. One cannot, for example, make any general statements about the beam-beam driving force which marks a 2.8σ separation as a beam separation which is more destructive in the Tevatron than a 4.2σ separation. The magnitude of particle losses at different beam separations is clearly dependent upon the excitation strength of a given

resonance and the manner in which particles are spread in tune across the resonance. This observation is also apparent in some beam-beam measurements which were done on a 1x1 proton-antiproton store in the SPS at CERN in 1989. Background losses during a tune scan across 13th and 16th order resonances showed higher background rates for 3σ beam separation than 6σ beam separation at the majority of points in the tune scan. At one of the extreme points in the tune scan, though, particle losses were 50% higher at 6σ separation than at 3σ separation.[25]

It should be noted that short particle lifetimes compare agreeably to conditions of large particle losses. A comparison of proton and antiproton losses with their respective particle lifetimes for a tune close to the $(2Q_x + 5Q_y)$ resonance is displayed in Figures 5.22 and 5.23. Particle losses and particle lifetimes are plotted for different beam separations. Particle lifetimes are calculated using bunch intensity data. Bunch intensities were fit to an assumed exponential decay

$$N = N_0 \exp(-\frac{t}{\tau}), \tag{5.6}$$

where t represents time and N_0 is the number of particles per bunch at $t = 0$. The decay constant τ is particle lifetime in units of hours and is plotted in Figures 5.22 and 5.23. The largest decrease in beam intensity and hence the smallest lifetime measurements occurred near this 7th order resonance.

5.4 Comparison with a Beam-beam Model

Certain parameters within a beam-beam model must be specified such that the model can be related to an experiment. Two different definitions of destructive behavior are used in this work to relate beam-beam simulation results to measured particle losses.

The first approach defines particle losses in an intuitive manner; equivalent to introducing an external obstacle into a particle's path. This method of analysis defines a limit on a particle's amplitude. Any particle whose amplitude reaches this limit is counted as a lost particle. A count of the number of lost particles allows a statistical interpretation of the simulation results.

The second approach examines the level of perturbation the beam-beam interaction introduces in a particle distribution. The % smear, a variation in the radius of motion in normalized phase space, is used as a measure of the amount of perturbation. The beam-beam simulation code used in this work focuses on a particle's motion which is due solely to nonlinearities of the beam-beam interaction. A measure of % smear in the beam-beam model

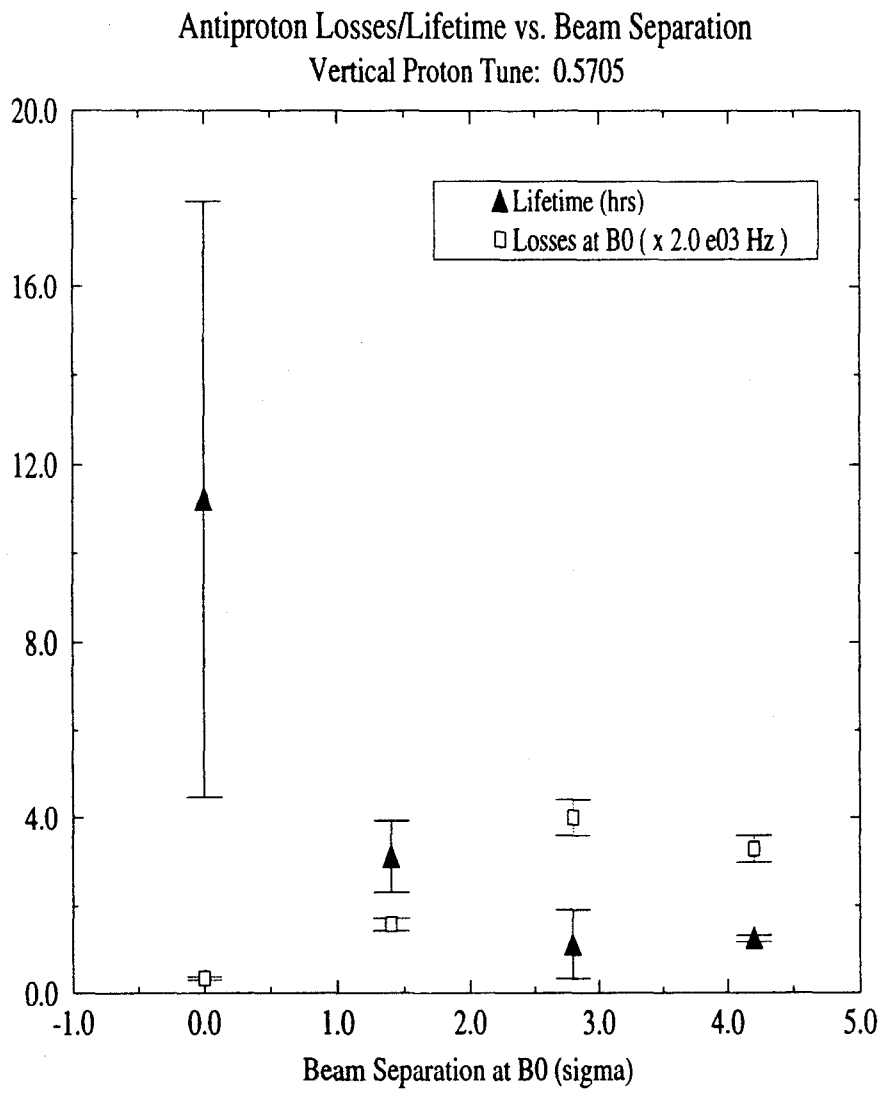

Figure 5.22: Antiproton losses and lifetimes at different beam separations. Each data point represents a measurement over a time span of approximately 4 minutes with the antiproton tunes close to the $(2Q_x + 5Q_y)$ resonance.

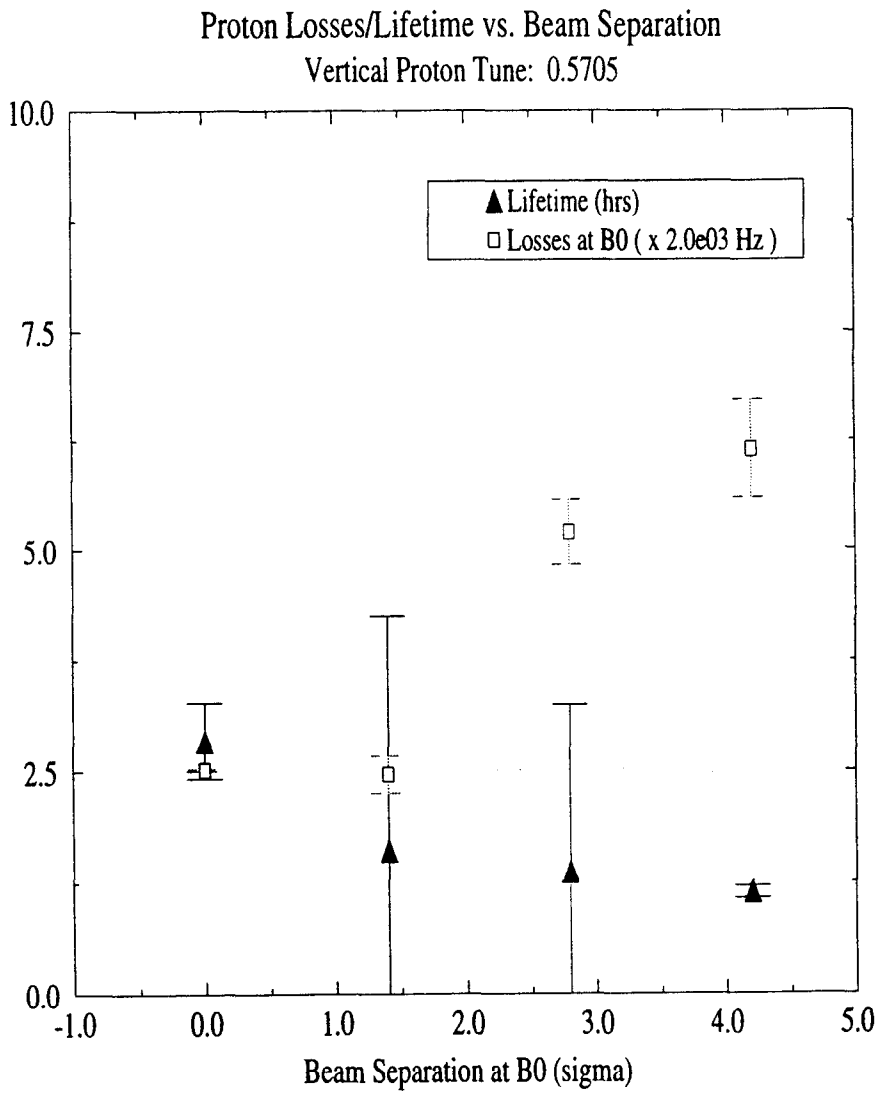

Figure 5.23: Proton losses and lifetimes at different beam separations. Each data point represents a measurement over a time span of approximately 4 minutes with the proton tunes close to the $(2Q_x + 5Q_y)$ resonance.

describes how strongly a particle's motion is affected by the beam-beam interaction. Particle losses are assumed to be related to the largest perturbations in the particle distribution; the maximum % smear of the particle distribution.

The first two parts of this section give more detailed information on how a lost particle and % smear are defined in the beam-beam simulations. Simulated tune scans are presented. The third part of this section presents simulations of the 1x1 beam-beam experiment done in the Tevatron during Collider Run IB.

Definition of a Lost Particle

A lost particle is defined as a particle whose maximum amplitude reaches a specified limit. The magnitude of this amplitude limit and the effect different amplitude limits have on the analysis is discussed in this section.

Particles are launched in the beam-beam simulation at various initial positions and phases. Particle amplitudes, defined by Equation 3.36, range from 0σ to 6σ. Initial particle positions and phases are distributed uniformly throughout phase space. This treatment of a particle distribution creates an artificially large population of high amplitude particles. In order to correct for this, a Gaussian weighting is imposed on a particle distribution. Particles are binned according to initial amplitude and the number of particles per bin is weighted using a Gaussian dependence. The range of amplitudes in each bin is 1σ.

The number of lost particles is defined in terms of a percentage of the total number of particles in the distribution. The % of particles which are lost is given by

$$\%\ lost = 100 \times \sum_b \frac{w_b}{N_b} N_{Lb}, \tag{5.7}$$

where the summation is over the number of bins, w_b is the weight of each bin and N_{Lb} is the number of lost particles in a given bin. The total number of particles per bin is given by N_b. Figure 5.24 displays the % of particles lost during a simulated vertical tune scan across the resonances labelled in Figure 5.18. Lost particles are plotted as a function of vertical base tune in the simulation. Each symbol in the top plot in Figure 5.24 represents the number of lost particles for different horizontal amplitude limits, ranging from 0σ to 3σ. The imposed Gaussian weighting scheme is evident; approximately 70% of the particle distribution is lost at a 1σ amplitude limit, 95% of the particle distribution is lost at a 2σ amplitude limit, etc. A fractional error, Δf, is associated with each simulation point and is given by

$$\Delta f = 100 \times N_L \sqrt{\sum_b \left(\frac{1}{\sqrt{N_b}}\right)^2}, \tag{5.8}$$

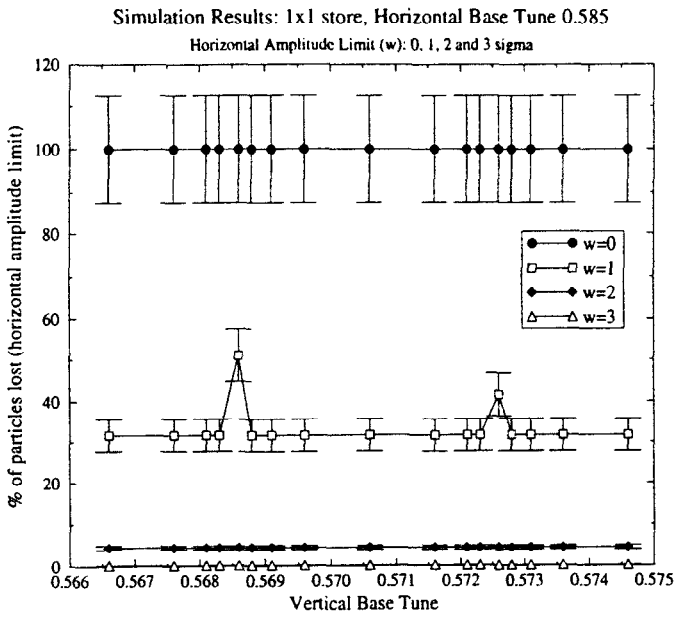

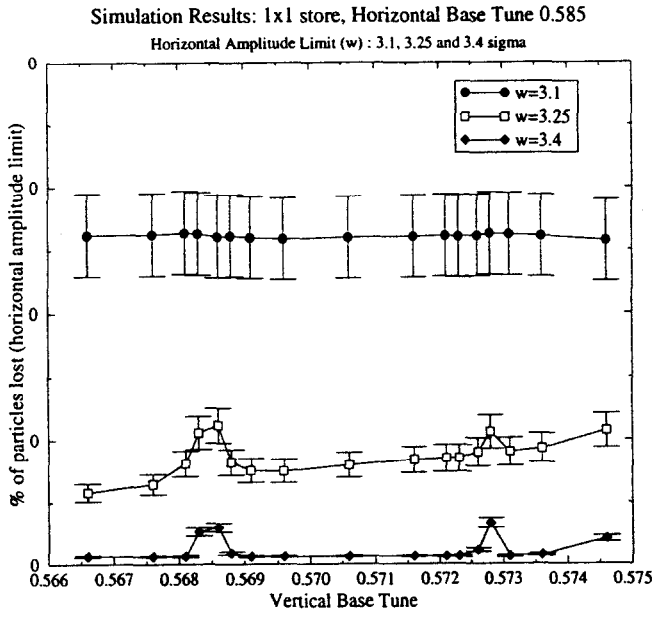

Figure 5.24: A vertical tune scan simulation displaying lost particles across the resonances of Figure 5.18. A beam separation of 2.8σ is present at B0. Each curve represents an amplitude constraint (denoted by w and in units of σ) used to define a particle as lost.

where N_L is the total number of particles lost.

Figure 5.25 plots particle losses for horizontal and vertical amplitude limits of 3.5σ. The top figure imposes a horizontal amplitude limit and the bottom figure imposes a vertical amplitude limit. It is interesting to see the effects of crossing a 9th order difference ($-1Q_x + 8Q_y$) resonance and two 7th order sum resonances ($7Q_y$ and $1Q_x + 6Q_y$) in the tune scan. The loss peak at a vertical base tune of 20.5726 corresponds to antiprotons close to the 9th order difference resonance. Note that only the fractional part of the base tune is enumerated in all plots. The loss peak at a vertical base tune of 20.5686 corresponds to antiprotons near the ($1Q_x + 6Q_y$) resonance. The $7Q_y$ resonance at a vertical base tune of 20.5714 is seen only when examining vertical motion. This is a reasonable observation since the resonant driving term has only a vertical component.

Note that evidence of resonance effects is dependent upon the amplitude limit chosen. The bottom plot of Figure 5.24 displays particle losses for horizontal amplitude limits within a 0.3σ range. Even with a limit specified over such a small range in amplitude, the resonance structure of some resonances is not always apparent.

Definition of Maximum % Smear

As discussed in Section 2.1, motion of a particle in a linear accelerator produces circular motion in normalized phase space. The radius of normalized phase space is

$$r = \sqrt{x_N^2 + x_N'^2}, \tag{5.9}$$

where (x_N, x_N') are the normalized coordinates of Equation 2.18. Figure 5.4 shows the effect of the beam-beam interaction on a particle's motion. A particle's position and phase is tracked for multiple turns with and without the beam-beam interaction present. The circular orbit present in the linear case becomes smeared due to the nonlinear kicks of the beam-beam interaction. The variation in the radius of the smeared orbit is known as % smear and is defined as

$$\%\ smear = \sqrt{\sum_{k=0}^{N} \frac{(r_k - r_m)^2}{(N-1)\, r_m^2}}, \tag{5.10}$$

where k denotes the turn number and N is the total number of turns. The mean radius over N turns is r_m.

It should be noted that very small amplitude particles (amplitudes less than 0.01σ) will give artificially large smears even for small variations in their mean radius. The intention is

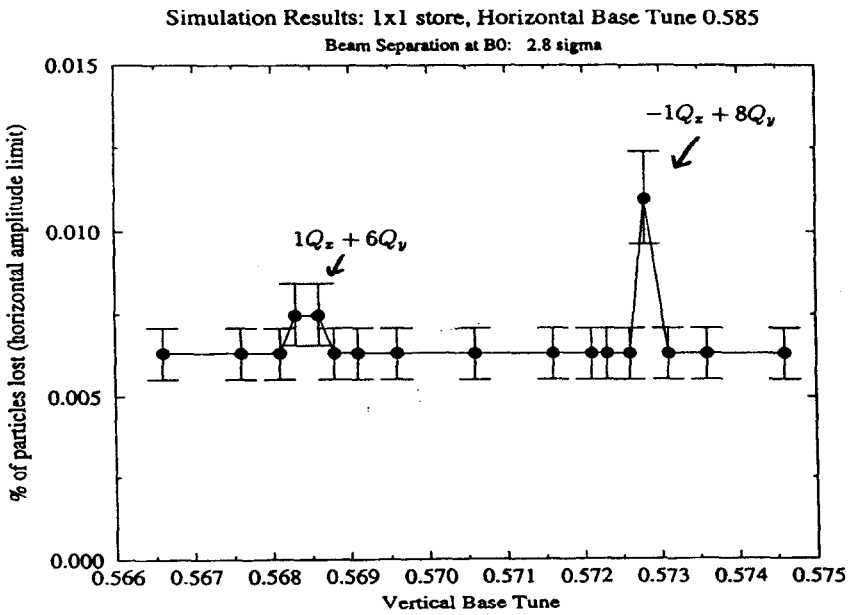

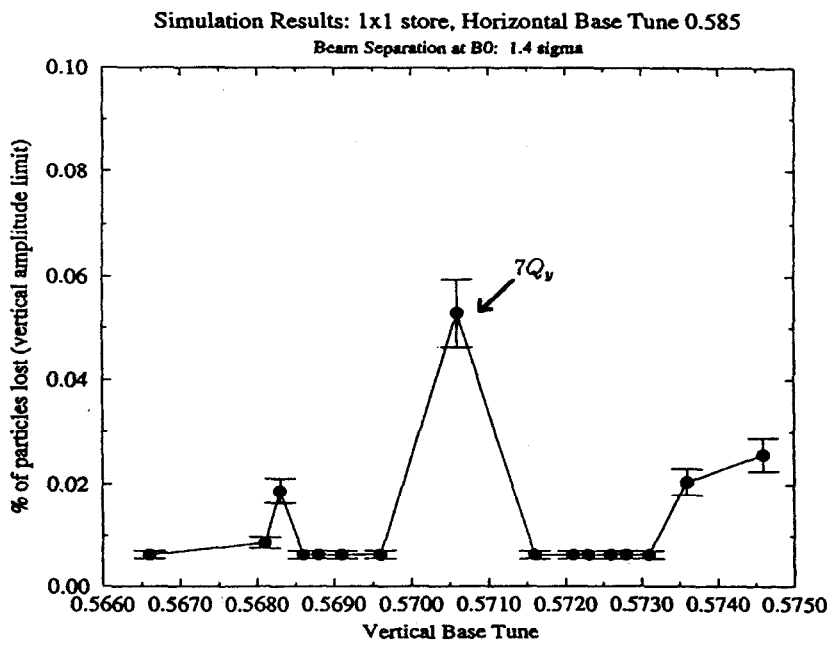

Figure 5.25: Simulation of a vertical tune scan for a 1x1 store. Particle losses reaching a horizontal and vertical amplitude limit of 3.5σ are displayed in the top and bottom plots, respectively.

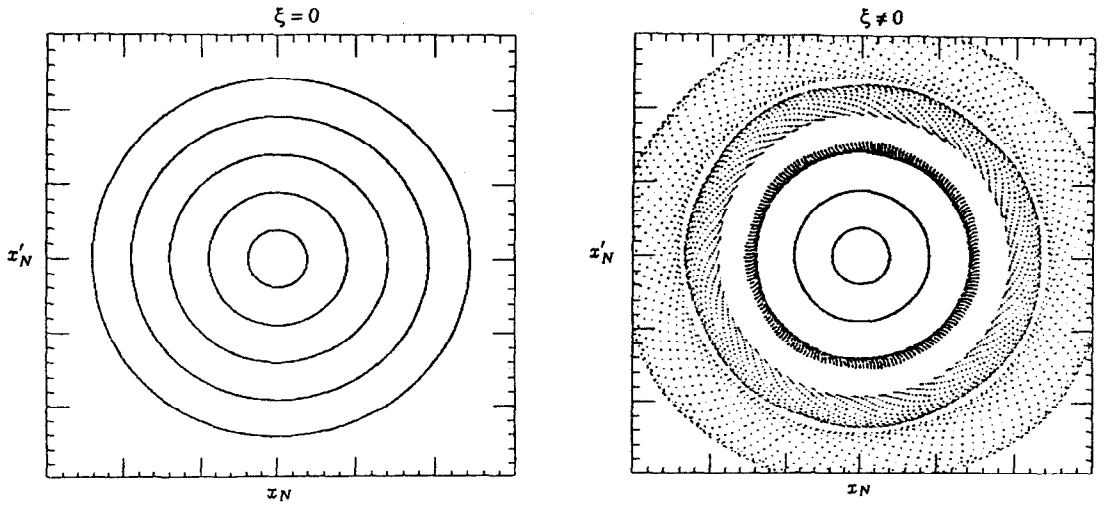

Figure 5.26: Simulation results showing the effect of the beam-beam interaction on one-dimensional motion. The position and phase of particles with different initial amplitudes is tracked over multiple turns and plotted in normalized phase space. The plot displays particle motion with ($\xi \neq 0$) and without ($\xi = 0$) the beam-beam interaction.

to relate % smear to particle losses, so it is assumed that perturbations in very small amplitude particles will not cause the particles to be lost. Only particles with initial amplitudes greater than 1σ in both planes are considered in measurements of maximum % smear.

Figure 5.27 plots maximum % smear in the horizontal and vertical planes for a tune scan across the resonances of Figure 5.18. The top figure measures horizontal % smear (measured in (x_N, x'_N) phase space) and the bottom figure measures vertical % smear (measured in (y_N, y'_N) phase space). The results are similar to those obtained in the tune scans of Figure 5.25.

Simulations of a 1x1 Store in the Tevatron

Beam-beam simulation results presented in this section are compared to the Tevatron beam-beam experiment discussed in Section 5.3.2.

Some parameters remain constant for all simulations. A particle is tracked for 16,000 turns, which corresponds to less than one second of real particle evolution. The total number of particles launched at various amplitudes and phases for each simulation point is approximately 2600. The normalized emittance is 15π mm-mrads in both the horizontal and vertical planes. The energy of the particle is 900 GeV.

The simulation includes a beam-beam kick at the B0 and E0 locations. Lattice functions at each beam-beam crossing point were calculated using a MAD lattice design program.[68]

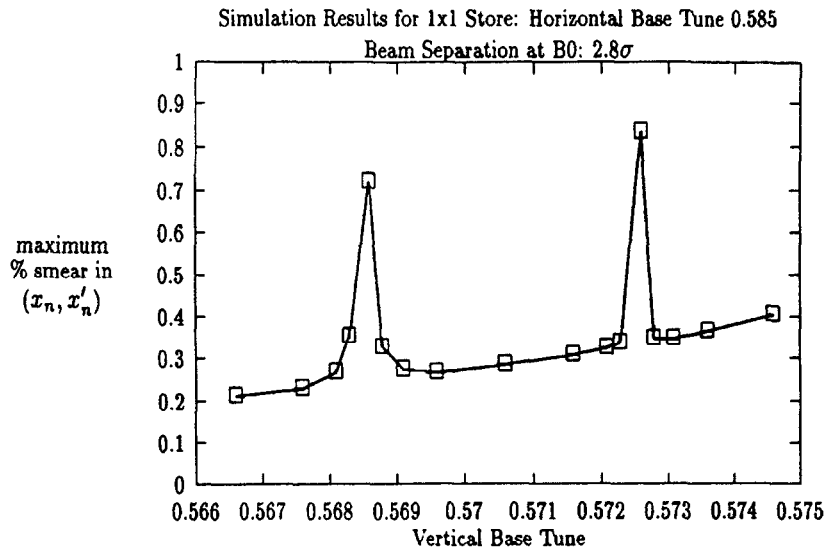

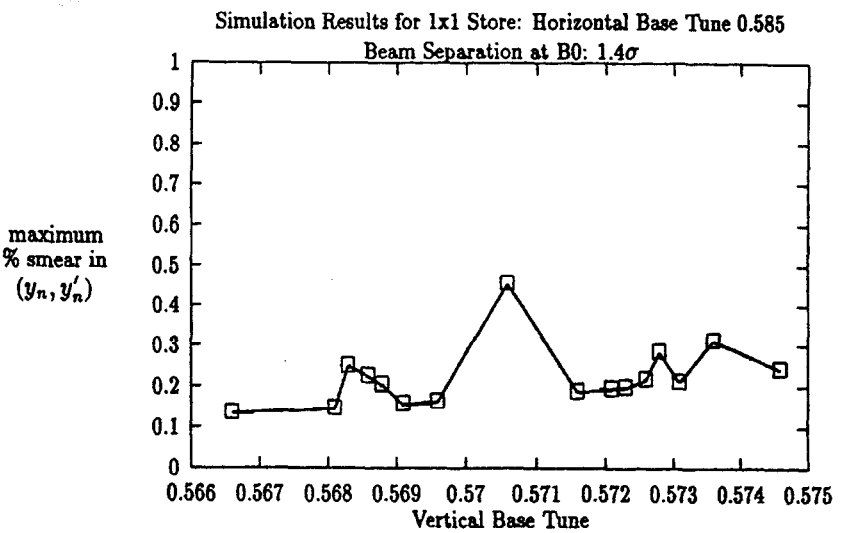

Figure 5.27: Simulation of a vertical tune scan for a 1x1 store. Maximum horizontal and vertical % smear is plotted in the top and bottom plots, respectively. The horizontal base tune remains constant at 20.585. The beam separation d is the beam separation at B0.

Closed orbits for different beam separations at B0 were calculated by including separator four-bumps in the lattice calculation. The angular deflections of the four-bump in the lattice were equivalent to the separator four-bumps used in the Tevatron. Similar to the four-bumps used in the Tevatron, the separator four-bumps used in the lattice calculation changed only the beam separation at B0. The beam separation at E0 remained a constant 2.6σ in the horizontal plane and 4.9σ in the vertical plane.

Determination of the amplitude limit which defines a lost particle is somewhat arbitrary. As discussed previously in this section (see Figure 5.24), a range of amplitude limits must be examined to ensure that resonant effects are seen. In this work, it is observed that different amplitude limits do not cause significant differences in a qualitative comparison of simulated losses at different beam separations.

In the simulation results discussed in this section, a lost particle is defined as one which reaches the tails of the Gaussian distribution; an amplitude limit of 3.5σ is defined for both the horizontal and vertical plane. In a Gaussian distribution of particles, 99.95% of the total number of particles are within a 3.5σ amplitude range.

As discussed in Section 3.5, it is necessary to consider the orbit offset due to the dipole contribution to the beam-beam kick. The position and angle offset at the location in which a particle's maximum amplitude is measured is obtained using Equation 2.35. The total orbit offset is the sum of the orbit offsets due to dipole kicks at the B0 and E0 crossing points. The largest dipole kick of 4.2 μrads occurs at B0 with a beam separation of 1.4σ. The dipole kick at E0 is 0.008 μrads and gives a negligible orbit offset in comparison with orbit offset due to the dipole kick at B0. The calculated closed orbit offset at the observation point which results from the B0 dipole kick is 11.65 μm. In terms of transverse beam sigma at the observation point, this orbit offset adds approximately 0.02σ to a particle's amplitude, which is a negligible effect.

This section is divided into subsections according to the labelled tune settings of Figure 5.21. The proton bunch intensities for measurements at the tune settings of Measurement 1 and 2 are approximately the same. The simulations run at these tune settings are discussed in the first subsection. Beam-beam simulations for Measurement 3 in Figure 5.21 are discussed in the next subsection. The last subsection discusses the experimental conditions of Measurement 4.

MEASUREMENT 1 AND 2

Beam-beam simulations of Measurement 1 and 2 of Figure 5.21 consist of simulated vertical tune scans across 7th order sum resonances and 9th and 11th order difference resonances; $7Q_y$, $(1Q_x + 6Q_y)$, $(-1Q_x + 8Q_y)$ and $(-2Q_x + 9Q_y)$. A proton intensity of 120×10^9 was used for all of the simulation runs discussed in this section.

While the vertical base tune is moved across these resonances, the horizontal base tune remains at 20.5854 during the tune scans. Note that the horizontal base tune used in the simulations is approximately 0.004 tune units larger than the horizontal base tunes of Measurement 1 and 2. Particles in the simulation are spread in tune across more 12th order resonances than in the actual beam-beam experiment. Since minimal losses have been observed in the Tevatron due to 12th order resonances, it is assumed that this discrepancy in the horizontal base tune is not significant. There is also a shift in the vertical base tune in which resonant effects are observed in the simulation because of this discrepency in the horizontal tune.

Figure 5.28 displays antiproton beam-beam tune footprints for a 1x1 store at a proton bunch intensity of 120×10^9. The footprint was obtained from simulation runs in a "resonance free" region of tune space (a region free of lower order resonances). In the simulations, particles were launched with amplitudes ranging from 0σ to 6σ in steps of 1σ and with zero initial phase. There was no Gaussian weighting imposed on the number of particles at a given amplitude. The base tune of the footprint is overlayed on the base tune setting of Measurement 1 in tune space; the tune spread which is plotted represents the tune spread of a particle distribution without resonant effects considered. In effect, it is a qualitative picture of the initial tune spread of the particle distribution. The four plots in the figure represent the four transverse beam separations at B0 which were present in the actual beam-beam experiment in the Tevatron. Figure 5.29 displays the same antiproton beam-beam footprints overlayed on the base tune setting of Measurement 2.

As seen in Figure 5.28, Measurement 1 examines the resonant excitation strength of 9th and 11th order difference resonances. Particles are close to the 9th order resonance and spread across the 11th order resonance when collisions are head-on or when there is a 1.4σ transverse beam separation at B0. At beam separations of 2.8σ and 4.2σ, the tunes of both large amplitude and small amplitude particles surround the 9th order resonance.

As Figure 5.29 indicates, the resonance effects of the $7Q_y$ and $(1Q_x+6Q_y)$ are measured in Measurement 2.

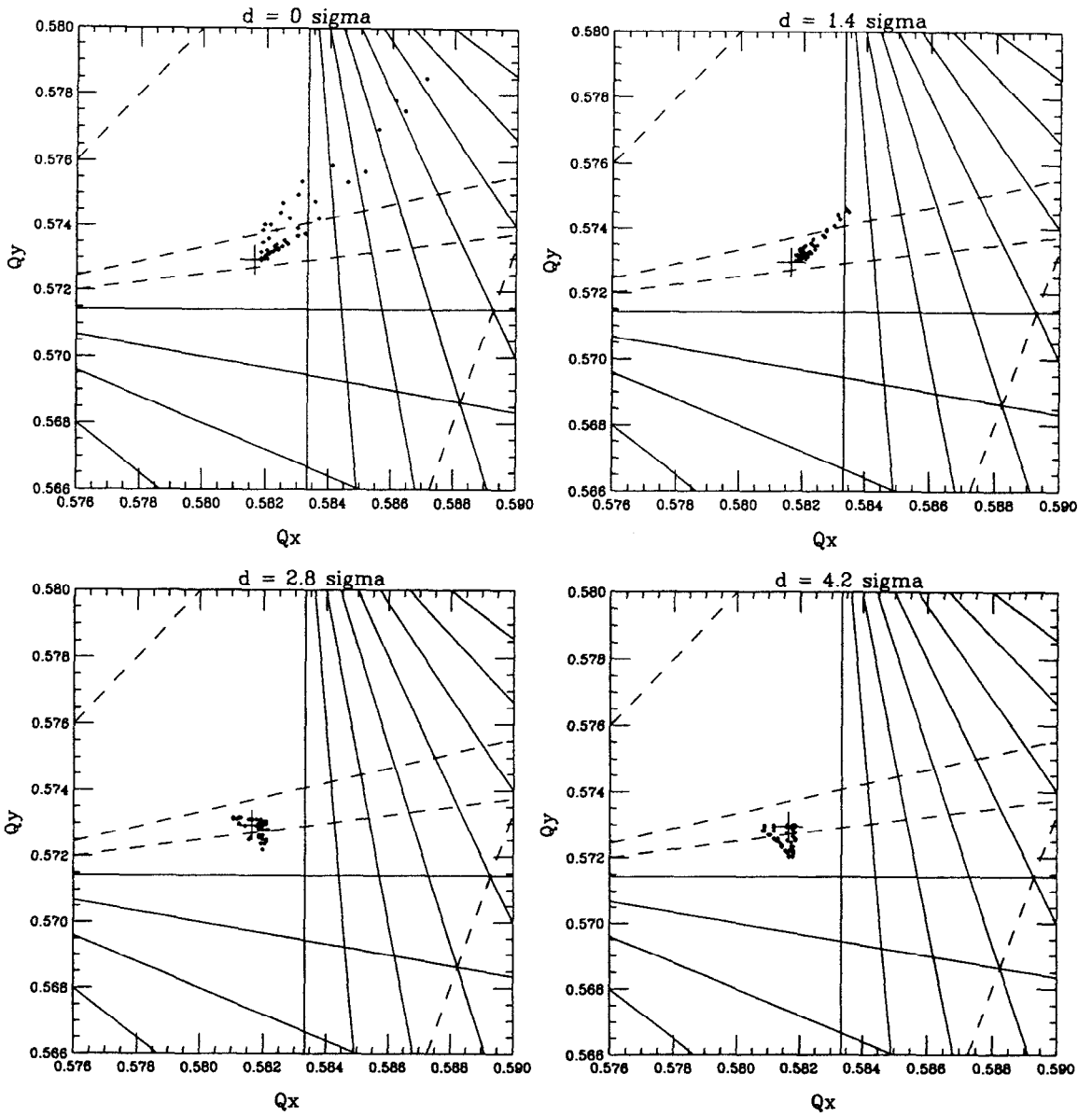

Figure 5.28: Antiproton beam-beam tune shift due to beam-beam detuning overlayed on base tune of Measurement 1. Tune shifts due to resonant effects are not shown. The proton intensity is 120×10^9. Beam-beam footprints represent collision points at both B0 and E0. Each plot represents a different beam separation at B0.

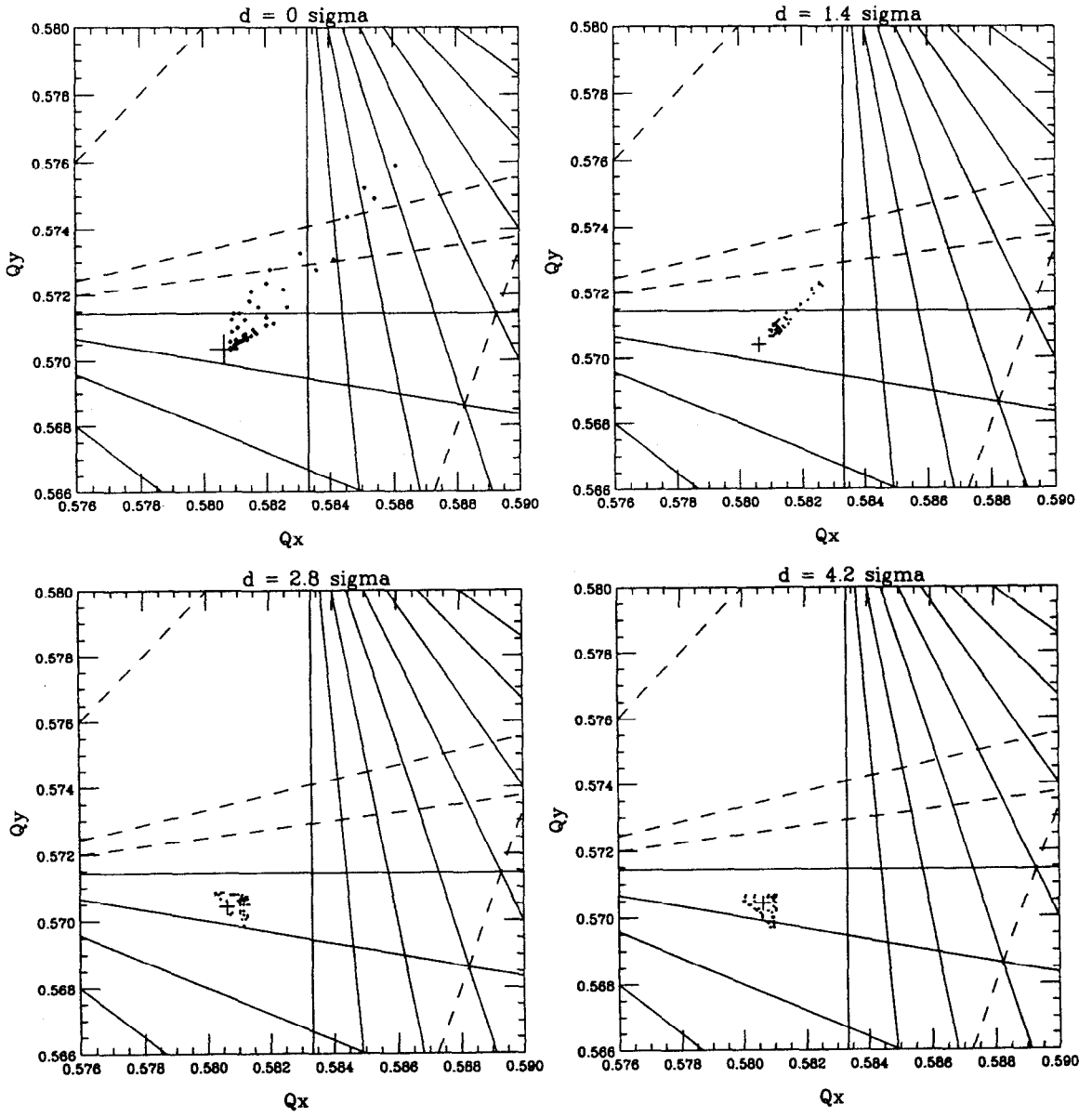

Figure 5.29: Antiproton beam-beam tune shift due to beam-beam detuning overlayed on base tune of Measurement 2. Tune shifts due to resonant effects are not shown. The proton intensity is 120×10^9. Beam-beam footprints represent collision points at both B0 and E0. Each plot represents a different beam separation at B0.

Figure 5.30 displays particle losses in a simulated vertical tune scan across these resonances. Particle losses in the top and bottom figures are measured with an imposed horizontal and vertical amplitude constraint, respectively. Each symbol in the plots represents a different transverse beam separation at B0. For completeness, simulations were also run for a beam separation of 5.7σ at B0, which corresponds to a 4σ beam separation in both the horizontal and vertical planes. No measurements were done in the Tevatron at this beam separation.

It is now necessary to account for the discrepency in the horizontal base tune between the simulation and the actual experiment. At a horizontal base tune of 20.5854, the vertical base tunes of the resonances of interest are listed in Table 5.5.

Measured particle losses at the tune setting of Measurement 1 (vertical base tune = 0.5733 ± 0.0003) are driven by $(-2Q_x + 9Q_y)$ and $(-1Q_x + 8Q_y)$ resonances. As Table 5.5 indicates, the vertical base tunes which satisfies these 7th order resonances are 20.5745 and 20.5732, respectively. Increased particle losses are observed near these vertical tune settings.

Resonant Tunes in Tune Scan Simulation

Resonance	Vertical Tune
$-2Q_x + 9Q_y$	20.5745
$-1Q_x + 8Q_y$	20.5732
$7Q_y$	20.5714
$1Q_x + 6Q_y$	20.5691

Table 5.5: Vertical tunes which satisfy the relation
$n_xQ_x \pm n_yQ_y = 144$ when $Q_x = 20.5854$.

Measured particle losses at the tune setting of Measurement 2 (vertical base tune = 0.5707 ± 0.0003) are driven by $7Q_y$ and $(1Q_x + 6Q_y)$ resonances. As Table 5.5 indicates, these resonances satisfy the 7th order resonant condition at vertical base tunes of 20.5714 and 20.5691,respectively. Peak losses which are due to these resonances are observed at vertical tunes which are shifted down from these calculated tune settings by approximately 0.0005 tune units. This effect is most likely due to particle tune spreads which spread over a region of tune space near the unperturbed base tune.

In the horizontal plane, a qualitative agreement between the simulation and Tevatron loss measurements is observed for both Measurement 1 and 2. As is the case in the beam-beam experiment, simulated particle losses are low in the case of head-on collisions and for

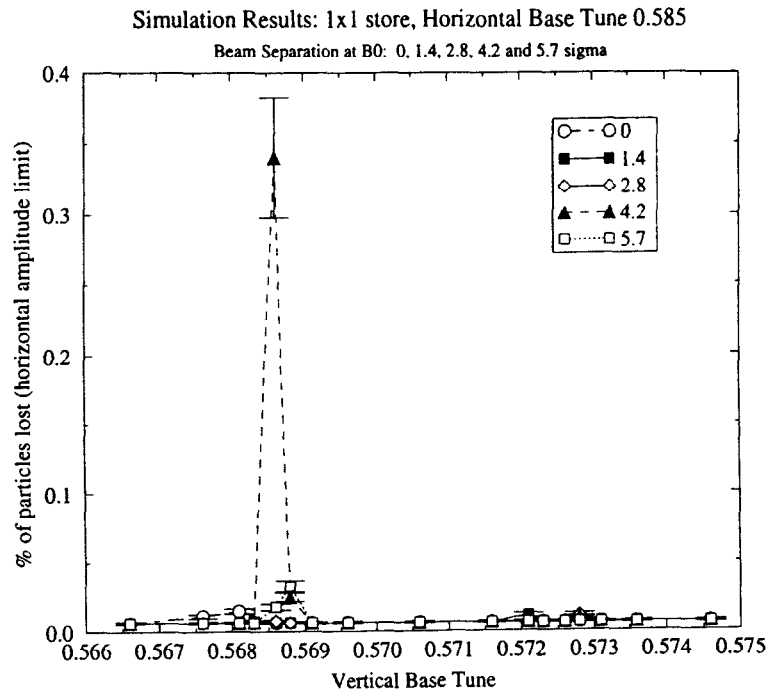

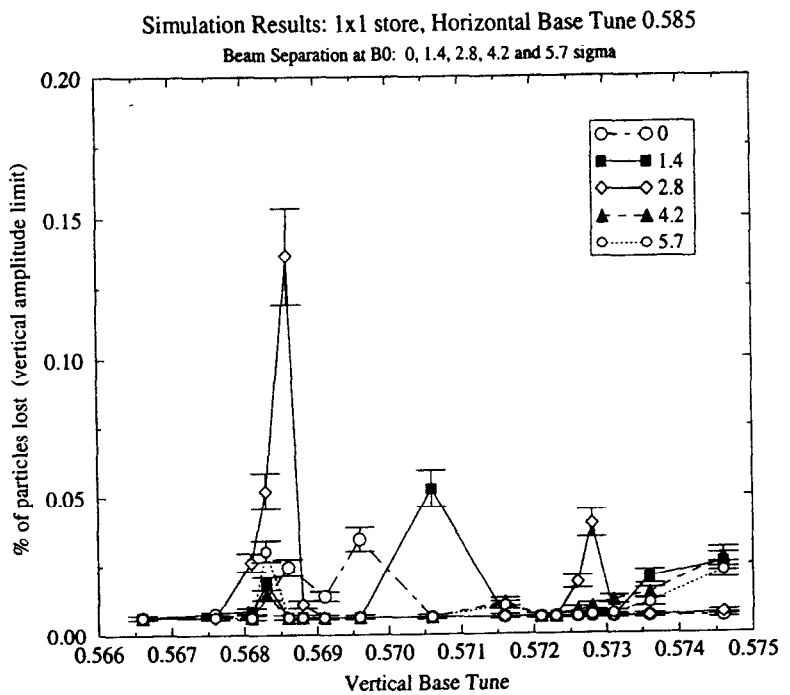

Figure 5.30: Simulation of 1x1 store measuring lost particles in a vertical tune scan. Lost particles in the top and bottom figure are defined with a horizontal and vertical amplitude limit, respectively.

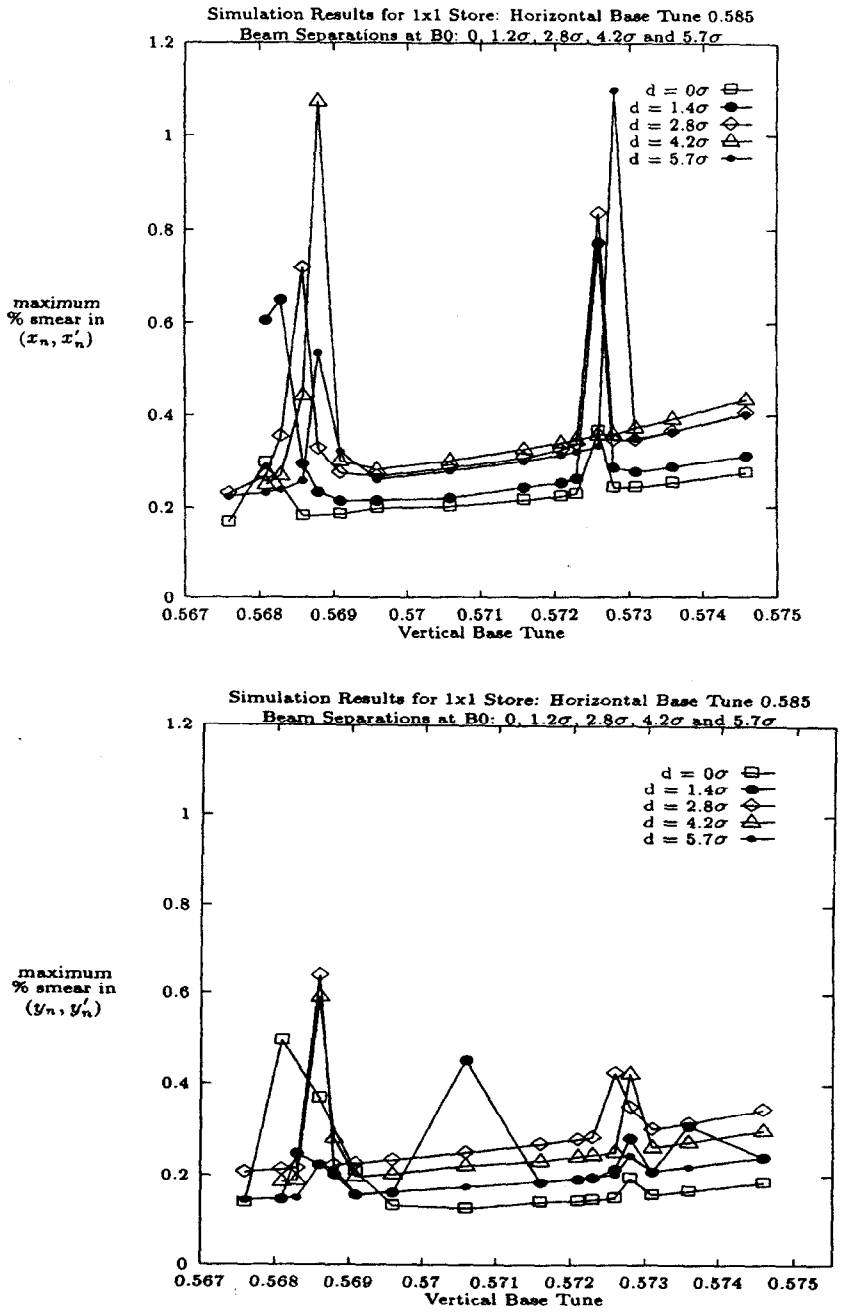

Figure 5.31: Simulation of 1x1 store measuring maximum % smear in a vertical tune scan. Maximum % smear in the horizontal and vertical planes are plotted in the top and bottom figures, respectively.

a 1.4σ beam separation. Simulated particle losses are comparatively low for all beam separations at the tune setting of Measurement 1, which agrees with the minimal losses measured in the Tevatron. Losses are predicted to be largest at a beam separation of 4.2σ due to the $(1Q_x + 6Q_y)$ resonance. The next largest particle loss is predicted at a beam separation of 2.8σ. As seen in Figure 5.19, this is indeed what is observed in Measurement 2. Simulated particle losses are predicted to decrease if the beam separation at B0 is increased to 5.7σ.

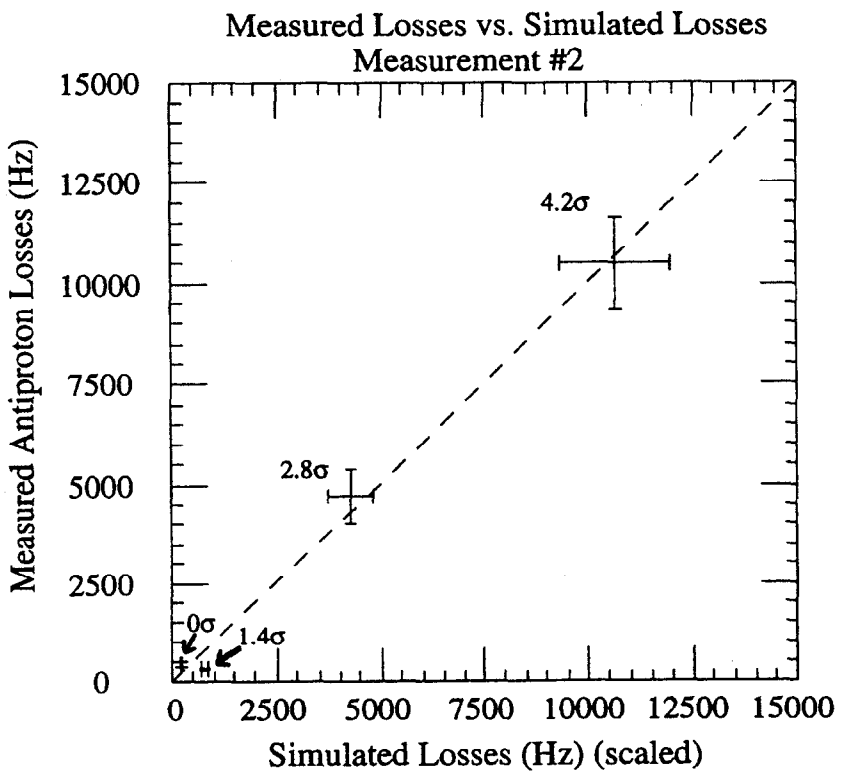

Figure 5.32: A comparison of measured particle losses to simulated particle losses for Measurement 2 of Figure 5.21. Each data point represents a different transverse beam separation at B0.

Figure 5.32 summarizes a qualitative comparison of particle losses measured at the tune setting of Measurement 2 in the Tevatron to the peak particle losses observed at a vertical base tune of 20.5686. At this base tune, resonant effects are largest in both the horizontal and vertical planes.

The conversion of particle losses from % of total particles lost to a loss rate is obtained as follows:

$$Simulated\ Losses\ (Hz) = \left(\frac{\%\,lost}{100}\,N_t\right)\left(\frac{1}{\Delta t}\right) \times SF. \tag{5.11}$$

The total number of particles in the simulation is given by N_t. The time of tracking is Δt, where Δt = (number of turns)$/f_{rev}$. The parameter SF is a constant scale factor which enables the comparison of loss measurements to be made on a unit slope. In Figure 5.32, SF is equal to 400.

It is observed in Figure 5.32 that, in a qualitative sense, simulation results compare agreeably with measured losses. In order to make a more quantitative comparison, knowledge of the parameters defining the scale factor SF would be necessary.

Figure 5.31 displays maximum horizontal and vertical % smear in the simulated tune scan. As in the beam-beam experiment in the Tevatron, maximum % smear for Measurement 2 (across the $(1Q_x + 6Q_y)$ resonance) is largest for a 4.2σ beam separation . At the same tune setting, the second largest peak occurs at a beam separation of 2.8σ, also in agreement with Measurement 2. Smear peaks of comparable magnitude, though, are observed across the $(-1Q_x + 8Q_y)$ resonance. This does not compare agreeably with the low particle losses of Measurement 1. It is therefore difficult to make a case that a measure of maximum % smear will accurately predict particle losses which will occur at at different transverse beam separations.

MEASUREMENT 3

Simulated particle losses and % maximum smear are compared to antiproton losses observed during Measurement 3 in the Tevatron (see Figure 5.19). Measured particle losses at the base tune setting of Measurement 3 (vertical base tune = 20.5684 ± 0.0003 and horizontal base tune = 20.5808 ± 0.0003) are driven by the $(2Q_x + 5Q_y)$ resonance. Beam-beam simulations of Measurement 3 of Figure 5.21 thus consist of simulated vertical tune scans across the $(2Q_x + 5Q_y)$ resonance. The horizontal base tune in the simulation remains constant at 20.5828 and is shifted by 0.002 from the horizontal base tune of Measurement 3. As in the previous section, this discrepency in the horizontal tune shift between the simulations and Measurement 3 will be accounted for.

A proton intensity of 95×10^9 is used for all of the simulation runs at this tune setting. Figure 5.33 displays the antiproton beam-beam tune footprints for a 1x1 store at this proton intensity. The base tune setting of the footprint calculation is overlayed on the base tune setting of Measurement 3 in tune space.

Figure 5.34 displays particle losses in a simulated vertical tune scan at different beam

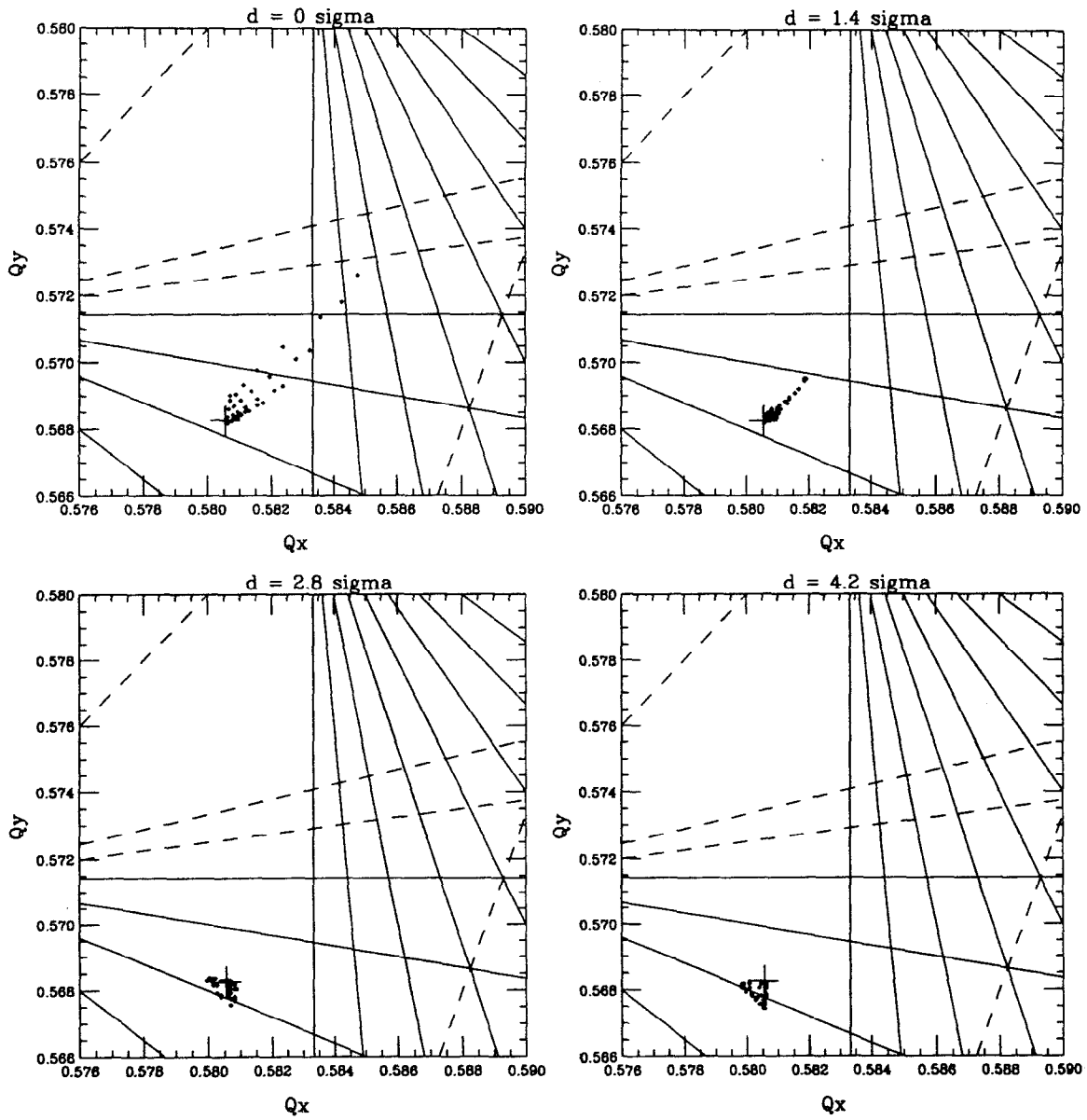

Figure 5.33: Antiproton beam-beam tune shift due to beam-beam detuning overlayed on base tune of Measurement 3. Tune shifts due to resonant effects are not shown. The proton intensity is 95×10^9. Beam-beam footprints represent collision points at both B0 and E0. Each plot represents a different beam separation at B0.

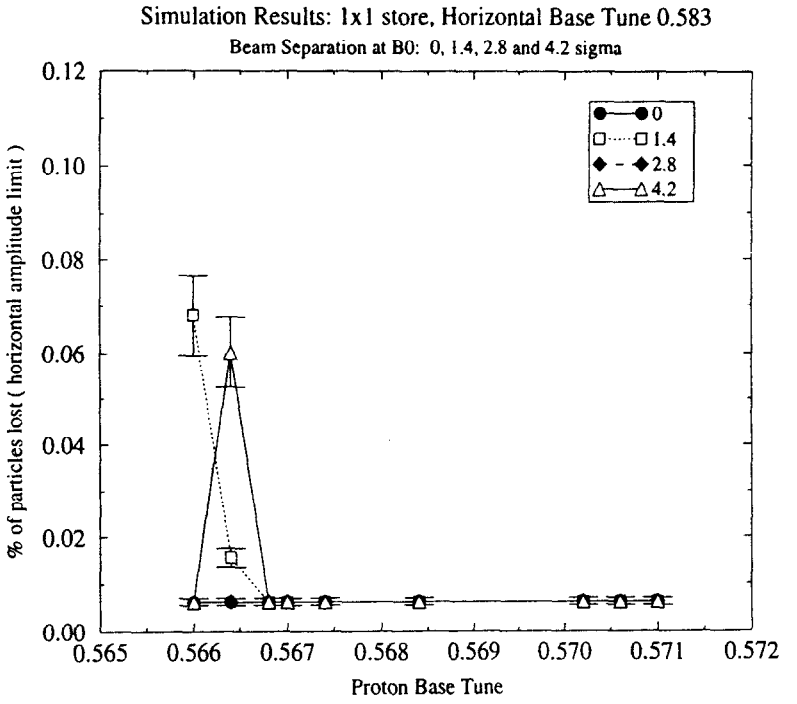

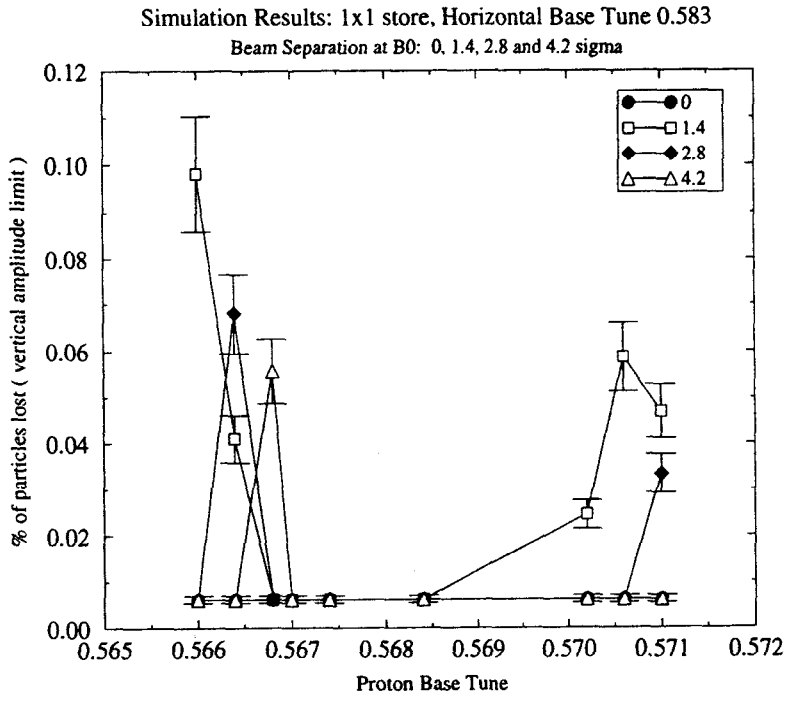

Figure 5.34: Simulation results displaying lost particles across a $(2Q_x + 5Q_y)$ resonance. Lost particles are defined as those particles reaching a horizontal and vertical amplitude of 3.5σ, respectively.

separations. At a horizontal base tune of 20.5828, the $(2Q_x + 5Q_y)$ resonance is observed in the simulated tune scan near the vertical base tune of 20.5669.

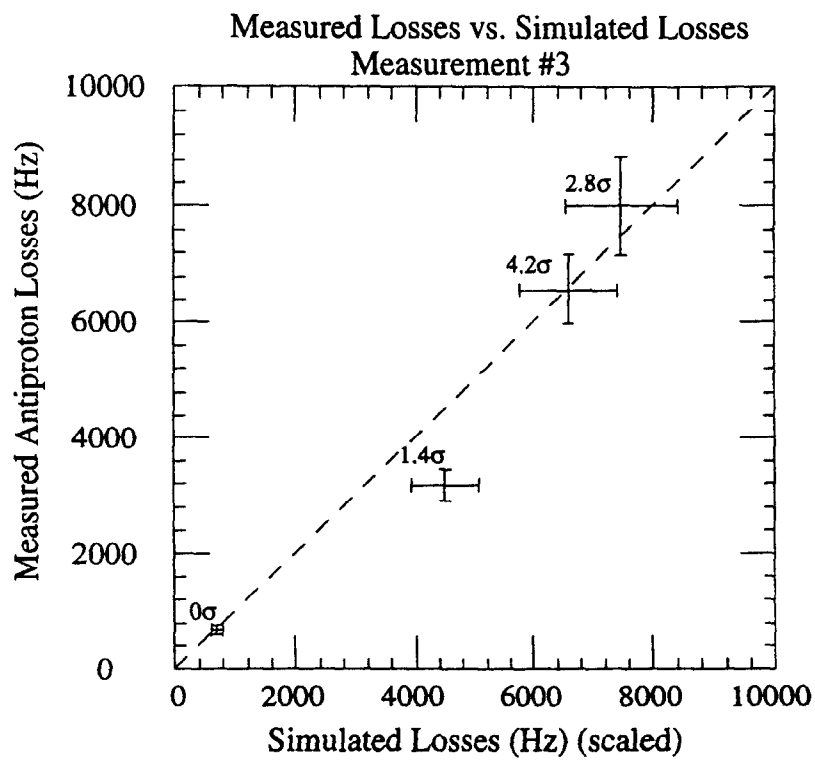

Figure 5.35: A comparison of measured particle losses to simulated particle losses for Measurement 3 of Figure 5.21. Each data point represents a different transverse beam separation at B0.

Figure 5.35 summarizes a comparison of particle losses measured at the tune setting of Measurement 3 in the Tevatron to simulated particle losses at a vertical base tune of 20.5664. This vertical base tune is shifted by 0.0005 tune units from the calculated tune setting which satisfies the relation $(2Q_x + 5Q_y = 144)$. An equivalent vertical base tune shift was used in the comparison of simulated particle losses to Measurement 2. The scale factor, SF, used for the conversion of simulated particle losses to a loss rate in Equation 5.11 is equal to 1400.

As in the case of Measurement 2, a qualitative comparison of measured losses of Measurement 3 and simulated losses is agreeable. Particle losses peak at a beam separation of 2.8σ and then begin to decrease at a beam separation of 4.2σ. Increased particle losses at a beam separation of 1.4σ are observed in both the simulation and in the measurement.

Figure 5.36 gives the maximum horizontal and vertical % smear in the simulated tune scan. At a simulated vertical base tune of 20.5664, simulation results agree qualitatively

with measured particles losses of Measurement 3.

MEASUREMENT 4

Measured particle losses in the Tevatron at the base tune setting of Measurement 4 of Figure 5.21 were very low for head-on collisions and for separated beams at B0. The average proton bunch intensity during the measurements was 57e9. Figure 5.37 displays the antiproton beam-beam tune footprints for a 1x1 store at this proton bunch intensity. As seen in the four plots, large amplitude particles remain in a resonance free region of tune space except in the case of head-on collisions. Since head-on collisions are not driven by odd-ordered resonances, it is not surprising to observe minimal particle losses at this tune setting. When a non-zero beam separation at B0 exists, large amplitude particles are far enough from 7th order resonances that no losses are observed. The antiproton beam-beam footprints give sufficient information to make a prediction that antiproton losses will be minimal at the base tune setting of Measurement 4.

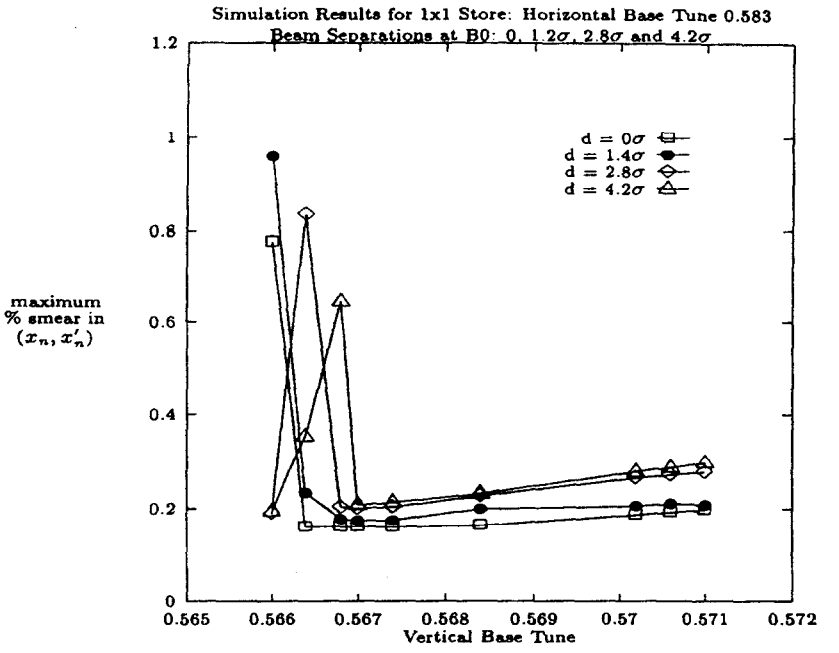

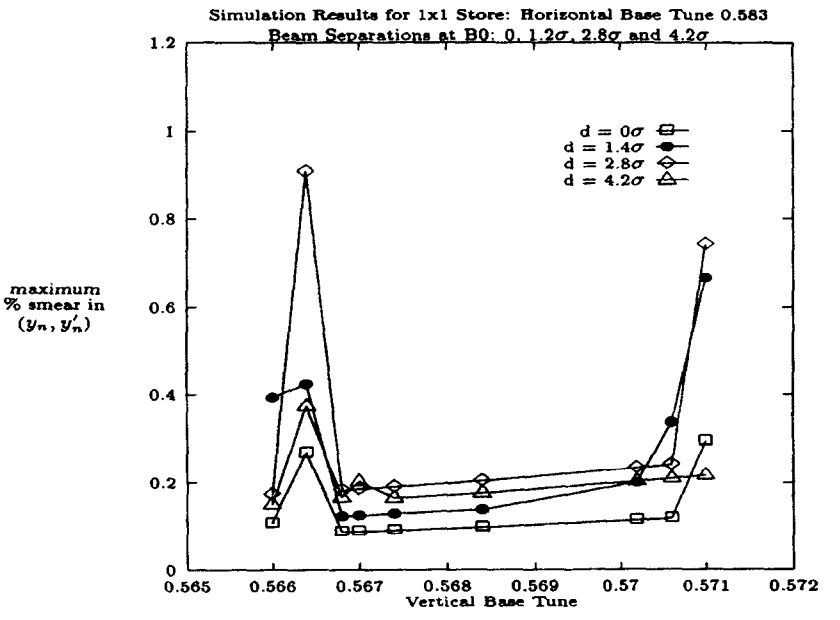

Figure 5.36: Simulation of 1x1 store measuring % smear across a $(2Q_x + 5Q_y)$ resonance. Maximum horizontal and vertical % smear are plotted in the top and bottom figures, respectively.

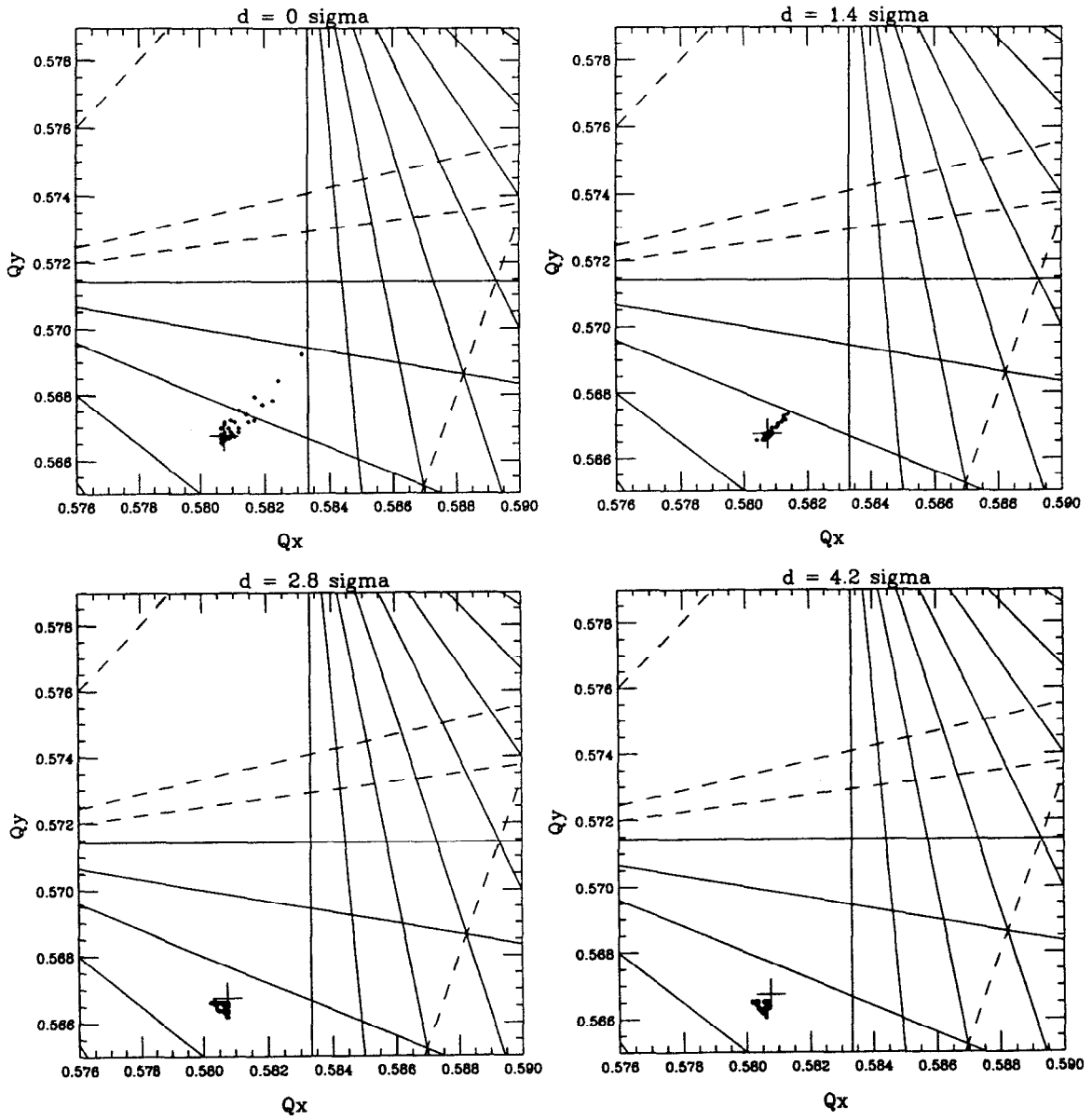

Figure 5.37: Antiproton beam-beam tune shift due to beam-beam detuning overlayed on base tune of Measurement 4. Tune shifts due to resonant effects are not shown. The proton intensity is 57×10^9. Beam-beam footprints represent collision points at both B0 and E0. Each plot represents a different beam separation at B0.

Chapter 6

CONCLUSIONS

A comparison of beam-beam experiments with simulations has led to a deeper understanding of the beam-beam interaction in the Tevatron Collider. Experimental work determined that the beam-beam interaction is the predominant nonlinear driving term which drives 7th order sum resonances in the Tevatron. Odd-ordered resonances were found to be driven in the presence of a transverse beam separation or when a crossing angle at an interaction point was present.

Since 7th order resonances define a border in tune space in which stable Collider operation occurs, a beam-beam experimental study was done to obtain a better understanding of beam-beam limits which exist in the Collider. Particle behavior in the presence of 7th order resonance driving terms was investigated. Resonant excitation due to the beam-beam interaction was investigated as a function of transverse beam separation. Using a single resonance model in a Hamiltonian formalism, theoretical calculations of beam-beam resonant excitation terms as a function of beam separation was also investigated. It is shown, in both the theoretical calculations and in actual beam-beam experiments, that it is difficult to predict a clear pattern of resonant excitation as a function of beam separation.

Simulated particle losses using a beam-beam model are shown to accurately predict relative magnitudes of beam-beam resonant excitation at different transverse beam separations. At various tune settings, each representing a different resonant excitation, particle losses as a function of beam separation were found to compare closely in simulations and loss measurements. A model of the beam-beam interaction is also shown to be capable of discovering dangerous resonances which will cause particle losses.

With such a strong correlation between experiments and beam-beam simulations there exist many possibilities for future studies. An investigation of how well particle loss measurements in a beam-beam simulation predict particle lifetimes is a suggested extension for

the beam-beam simulation model. A study of the predictive power of a beam-beam simulation in defining minimum beam separation criteria would be useful for understanding the operation of the Collider in different bunch configurations.

Chapter 7

APPENDICES

Appendix A

Orbit Control of Beam Separation and Crossing Angle at an Interaction Point

An algorithm used to provide simultaneous control of the transverse separation and crossing angle of colliding beams at an interaction point is presented.

Controlling both the beam separation and crossing angle at an interaction point s_P requires a closed orbit distortion using four separators; two on each side of the interaction region. A four-bump algorithm specifies the angular deflections, $\Delta\theta_i$, applied to the separators to produce a closed orbit deflection of a specified orbit displacement, x_p, and specified phase, $x_p^{'}$, at an interaction point. The four-bump is localized in that it produces an orbit distortion only in the region bounded by the first and last separator bump elements.

A four-bump is necessary because of the number of constraints and variables in the bump calculation. A local three-bump has three variables ($\Delta\theta$'s of the three-bump elements) and three constraints. One of the constraints is the magnitude of the bump at a given location and the other two constraints ensure that the bump is local; the outgoing position and phase at the two endpoints of the bump are constrained to zero. It is of interest to constrain both the separation and crossing angle at an interaction point s_P, along with keeping the bump local. Thus a second three-bump is needed to provide the additional constraint. The four-bump algorithm results from the addition of two localized three-bumps.

Consider the schematic of Figure A.1. Angular deflections representing two three-bumps (dashed and dotted lines) are added to create a four-bump (solid line). The effect an angular deflection of magnitude $\Delta\theta_0$ at s_0 has on a particle's orbit at s_1 is found using Equation 2.9, which is reproduced here for convenience:

$$x(s) = A\sqrt{\beta(s)}\sin(\psi(s) + \delta). \tag{A.1}$$

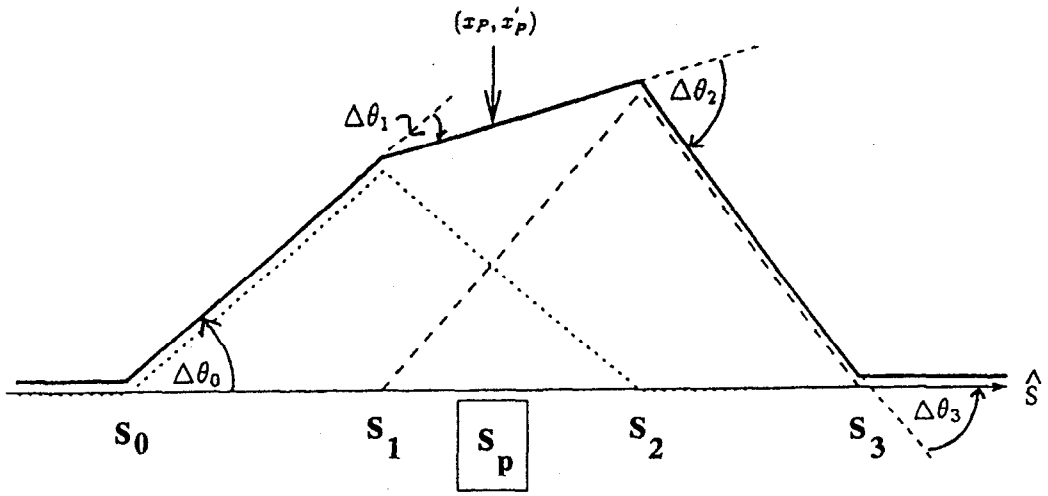

Figure A.1: Schematic of a four-bump which controls the position and phase at point s_P. The four-bump (solid line) is the result of the addition of two three-bumps (dotted and dashed lines). Angular deflections occur at longitudinal locations s_0,s_1,s_2 and s_3.

The constants A and δ are determined from initial conditions. Let $x_0 = 0$ at a location in which $\psi = 0$ and let $x_0' = \Delta\theta_0$ at that point. The solutions for the initial conditions are then found to be $\delta = 0$ and $A = \sqrt{\beta_0}\ \Delta\theta_0$. An orbit displacement x_1 at s_1 due to an angular deflection at s_0 is thus given by

$$x_1 = \Delta\theta_0\sqrt{\beta_1\beta_0}\sin\Delta\psi_{10}, \tag{A.2}$$

where $\Delta\psi_{10} = \psi_1 - \psi_0$ is the phase advance from s_0 to s_1. The lattice functions β_0 and β_1 are the beta functions at s_0 and s_1, respectively. The derivative of x_1 with respect to s gives x_1' in terms of $\Delta\theta_0$ as

$$x_1' = \Delta\theta_0\sqrt{\frac{\beta_0}{\beta_1}}\left[\cos\Delta\psi_{10} - \alpha_1\sin\Delta\psi_{10}\right]. \tag{A.3}$$

Both x_1 and x_1' depend on $\Delta\theta_0$ and on the lattice functions at s_0 and s_1. It is assumed that the lattice functions are known. As a result, the above expressions may be rewritten as

$$\begin{aligned} x_1 &= A\ \Delta\theta_0 \\ x_1' &= B\ \Delta\theta_0 \end{aligned} \tag{A.4}$$

where A and B are constants expressed in terms of lattice functions in Equations A.2 and A.3, respectively.

From Chapter 2 (Equation 2.13), a particle's traversal in one plane from s_P to s_1 is described by

$$\begin{pmatrix} x_1 \\ x_1' \end{pmatrix} = M_{P\to 1} \begin{pmatrix} x_P \\ x_P' \end{pmatrix}. \tag{A.5}$$

The elements of the transfer matrix depend entirely on the lattice functions at s_P and s_1. The orbit displacement and phase at s_1 is thus expressed in terms of the orbit displacement and phase at s_P multiplied by the constant matrix elements of $M_{P\to 1}$:

$$\begin{aligned} x_1 &= [(m_{11})_{P\to 1}]\, x_P + [(m_{12})_{P\to 1}]\, x_P' \\ x_1' &= [(m_{21})_{P\to 1}]\, x_P + [(m_{22})_{P\to 1}]\, x_P', \end{aligned} \tag{A.6}$$

where $(m_{ij})_{P\to 1}$ is the matrix element in the ith row and jth column of $M_{P\to 1}$. Solving for $\Delta\theta_0$ in terms of x_p and x_p' using Equations A.4 and A.6 yields two equations which must be simultaneously satisfied:

$$\begin{aligned} \Delta\theta_0 &= \frac{x_1}{A} = \frac{[(m_{11})_{P\to 1}]\, x_P + [(m_{12})_{P\to 1}]\, x_P'}{A} \\ \Delta\theta_0 &= \frac{x_1'}{B} = \frac{[(m_{21})_{P\to 1}]\, x_P + [(m_{22})_{P\to 1}]\, x_P'}{B}. \end{aligned} \tag{A.7}$$

If x_P is specified as a constraint, the two equations yield solutions for x_P' and x_1. A phase contribution at an interaction point, therefore, is introduced once an orbit displacement is specified. Similarly, specifying a particle's phase will introduce an orbit displacement. Once x_1 is known, the angular deflections for a localized three bump at s_0, s_1 and s_2 are found using the familiar three-bump algorithm.[9] The additional phase contribution which is introduced at the interaction point must then be cancelled by subtracting a second three-bump constrained to the same phase.

The angular deflections for the first three-bump at s_0,s_1 and s_2 are calculated using a local three-bump algorithm:[9]

$$\begin{aligned} \Delta\theta_{0a} &= \frac{x_{1a}}{\sqrt{\beta_0\beta_1}\sin(\psi_1-\psi_0)}, \\ \Delta\theta_{1a} &= \Delta\theta_{0a}\sqrt{\frac{\beta_0}{\beta_1}}\frac{\sin(\psi_2-\psi_0)}{\sin(\psi_2-\psi_1)}, \\ \Delta\theta_{2a} &= \Delta\theta_{0a}\sqrt{\frac{\beta_0}{\beta_2}}\frac{\sin(\psi_1-\psi_0)}{\sin(\psi_2-\psi_1)}. \end{aligned} \tag{A.8}$$

Note that $x_{1a} \equiv x_1$ in Equation A.6 above. The index a is added to the subscript of x_1 and $\Delta\theta_i$ in order to make a distinction between the two three-bump calculations.

Similarly, the angular deflections due to a second three-bump at s_1, s_2 and s_3 are calculated as follows. An angular deflection at s_1, $\Delta\theta_{1b}$, translates into an orbit displacement at s_2 of magnitude

$$x_{2b} = \Delta\theta_{1b}\sqrt{\beta_2\beta_1}\sin\Delta\psi_{21}. \tag{A.9}$$

The subscript b designates the second three bump. In terms of x_P and $x_P^{'}$, the orbit displacement and phase at s_2 is given by

$$\begin{aligned} x_{2b} &= [(m_{11})_{P\to 2}]\, x_P + [(m_{12})_{P\to 2}]\, x_P^{'}, \\ x_{2b}^{'} &= [(m_{21})_{P\to 2}]\, x_P + [(m_{22})_{P\to 2}]\, x_P^{'}. \end{aligned} \tag{A.10}$$

The angular deflections for the second three bump are given by

$$\begin{aligned} \Delta\theta_{1b} &= \frac{x_{2b}}{\sqrt{\beta_1\beta_2}\sin(\psi_2-\psi_1)}, \\ \Delta\theta_{2b} &= \Delta\theta_{1b}\sqrt{\frac{\beta_1}{\beta_2}}\frac{\sin(\psi_3-\psi_1)}{\sin(\psi_3-\psi_2)}, \\ \Delta\theta_{3b} &= \Delta\theta_{1b}\sqrt{\frac{\beta_1}{\beta_3}}\frac{\sin(\psi_2-\psi_1)}{\sin(\psi_3-\psi_2)}. \end{aligned} \tag{A.11}$$

By subtracting the angular deflections of the second three-bump from the first three-bump, the undesired phase or orbit distortion introduced by the first three-bump is eliminated. The final four-bump angular deflections are expressed as

$$\begin{aligned} \Delta\theta_0 &= \Delta\theta_{0a}, \\ \Delta\theta_1 &= \Delta\theta_{1a} - \Delta\theta_{1b}, \\ \Delta\theta_2 &= \Delta\theta_{2a} - \Delta\theta_{2b}, \\ \Delta\theta_3 &= -\Delta\theta_{3b}, \end{aligned} \tag{A.12}$$

where $\Delta\theta_a$ and $\Delta\theta_b$ are listed in Equations A.8 and A.11, respectively.

Since the bump elements in this case are separators, a conversion from the μrad settings calculated above to kV settings is necessary. The kV to μrad conversion is given by

$$V[kV] = \frac{\Delta\theta[\mu rad] * p[GeV/c] * g[cm]}{l[cm] * n_{modules}}, \tag{A.13}$$

where V is the voltage across opposing separator plates and p is the momentum of the beam. The gap across the plates is denoted as g. The length of the plate is l and the number of modules which compose one separator is $n_{modules}$. In the Tevatron, the separator gap is 5 cm. A module length is 257 cm. The number of modules at each location is shown in Figure 5.1.

Separator Lattice Parameters

Location	F17	A17	A49	B11	B17	B17	C49	D11
# horizontal modules	1	0	1	2	4	0	1	2
# vertical modules	0	1	2	1	0	4	2	1
β_x (m)	52.9	-	832.8	298.4	68.1	-	774.2	278.6
β_y (m)	-	40.8	251.2	711.8	-	26.8	247.7	686.7
ψ_x (rads)	24.5	-	60.2	63.3	68.9	-	104.6	107.8
ψ_y (rads)	-	44.5	61.9	65.0	-	89.1	106.3	109.4

Table A.1: Separator lattice parameters in Collider Run IA. A phase advance of zero is defined at the E0 straight section. Lattice values are averaged over the number of modules.

Table A.1 lists the lattice functions of the separators in Collider Run IA. The lattice functions listed are values averaged over the number of modules.

Appendix B

LUMINOSITY AS A FUNCTION OF SEPARATION AND CROSSING ANGLE

This appendix presents a calculation of luminosity as a function of transverse separation and crossing angle of two colliding particle distributions. It closely follows the luminosity calculation for head-on collisions as described by Month.[63] Note that this is an alternative derivation of luminosity as compared with Equation 1.1, which is a definition of luminosity.

The luminosity, L, is a relativistic invariant. It is described by

$$L = c\sqrt{|\vec{\beta}_1 - \vec{\beta}_2|^2 - |\vec{\beta}_1 \times \vec{\beta}_2|^2}\, I(x,y,z,t) \tag{B.1}$$

where the parameter c is the speed of light and $\vec{\beta}$ is the particle velocities in units of the speed of light. The subscripts 1 and 2 denote bunches 1 and 2, respectively. The overlap integral, $I(x,y,z,t)$, is the overlap of the colliding particle distributions integrated over three-dimensional space and time.

$$I(x,y,z,t) = \int_{-\infty}^{\infty} dV \int_{-\infty}^{\infty} dt\; \rho_1(x,y,z,t)\, \rho_2(x,y,z,t) \tag{B.2}$$

where $dV \equiv dx\, dy\, dz$ represents an integration over space and t represents an integration over time.

The particle distributions, assumed Gaussian, colliding with a transverse separation of magnitude d_x and d_y in the horizontal and vertical planes, respectively, are given by

$$\rho_1(x,y,z,t) = \frac{N_1}{(2\pi)^{3/2}\sigma_{1x}\sigma_{1y}\sigma_{1z}} \exp\left(-\frac{1}{2}\left[\frac{x^2}{\sigma_{1x}^2} + \frac{y^2}{\sigma_{1y}^2} + \frac{(z-\delta_1)^2}{\sigma_{1z}^2}\right]\right) \tag{B.3}$$

$$\rho_2(x,y,z,t) = \frac{N_2}{(2\pi)^{3/2}\sigma_{2x}\sigma_{2y}\sigma_{2z}} \exp\left(-\frac{1}{2}\left[\frac{(x-d_x)^2}{\sigma_{2x}^2} + \frac{(y-d_y)^2}{\sigma_{2y}^2} + \frac{(z-\delta_2)^2}{\sigma_{2z}^2}\right]\right). \tag{B.4}$$

The number of particles per bunch is given by N. The longitudinal offset of the centroids of the colliding bunches is given by δ. If one of the bunches, for example, is centered at the collison point at $t = 0$ and the other bunch is offset from the collision point by an amount z_0 at $t = 0$, the longitudinal offset parameters satisfy $\delta_1 = ct$ and $\delta_2 = -ct + z_0$. The rms bunch size is parameterized by σ in both the transverse and longitudinal planes.

Recall from Equation 2.28 that σ is itself a function of z:

$$\sigma(z) = \sqrt{\beta(z)\epsilon + \left(\eta(z)\frac{\sigma_p}{p}\right)^2}, \tag{B.5}$$

where $\beta(z)$ is described by Equation 2.44 and the dispersion $\eta(z)$ is linear through a drift space: $\eta(z) = \eta_{z=0} + \eta' z$. In terms of accelerator parameters, the rms momentum spread of a bunch is given by[66]

$$\left(\frac{\sigma_p}{p}\right) = \frac{1}{\beta_{rel}}\sqrt{\frac{2(eV)}{\pi h \mid \eta \mid E_s}} \sin\left(\frac{\sigma_z h}{2R}\right). \tag{B.6}$$

The peak accelerating voltage per turn is given by (eV). Relativistic beta is explicitely written as β_{rel}. The harmonic number is denoted by h. The radius of the accelerating ring is given by R and the total synchronous energy is E_s. The frequency dispersion parameter, η, is dependent upon both the transition gamma, γ_t, and relativistic gamma, γ_{rel}:

$$\eta = \left|\frac{1}{\gamma_t^2} - \frac{1}{\gamma_{rel}^2}\right|. \tag{B.7}$$

The instantaneous luminosity, $L(t)$, is in units of $cm^{-2}\ sec^{-1}$. The luminosity per bunch collision, $\mathcal{L}$, is found by integrating over time and is in units of cm^{-2}.

The integration of the overlap integral over transverse space is solved analytically:

$$\int_{-\infty}^{\infty} dk\ \exp\left(-\frac{1}{2}\left[\frac{k^2}{\sigma_{1k}^2} + \frac{(k-d_k)^2}{\sigma_{1k}^2}\right]\right) = \sqrt{\frac{2\pi\sigma_{1k}^2\sigma_{1k}^2}{(\sigma_{1k}^2+\sigma_{2k}^2)}}\ \exp\left[\frac{-d_k^2}{(\sigma_{1k}^2+\sigma_{2k}^2)}\right] \tag{B.8}$$

where $k \equiv x, y$ represents either transverse dimension.

The integral over time is also analytically solved:

$$\int_{-\infty}^{\infty} dt\ \exp\left(-\frac{1}{2}\left[\frac{(z-ct)^2}{\sigma_{1z}^2} + \frac{(z+ct-z_0)^2}{\sigma_{2z}^2}\right]\right) = \frac{1}{c}\sqrt{\frac{2\pi\sigma_{1z}^2\sigma_{2z}^2}{(\sigma_{1z}^2+\sigma_{2z}^2)}}\ \exp\left[\frac{(2z-z_0)^2}{(\sigma_{1z}^2+\sigma_{2z}^2)}\right] \tag{B.9}$$

For convenience, define the new parameters:

$$\begin{aligned} \sigma_x^2(z) &= \sigma_{1x}^2(z) + \sigma_{2x}^2(z), \\ \sigma_y^2(z) &= \sigma_{1y}^2(z) + \sigma_{2y}^2(z), \\ \sigma_z^2 &= \sigma_{1z}^2 + \sigma_{2z}^2. \end{aligned} \tag{B.10}$$

Upon combining the results of the integrations of Equations B.8 and B.9, the overlap integral becomes a function of longitudinal space only.

$$I = \frac{N_1 N_2}{(2\pi)^{3/2}\sigma_z\, c} \int_{-\infty}^{\infty} dz \frac{1}{\sigma_x(z)\,\sigma_y(z)} \exp\left[-\frac{d_x^2}{2\sigma_x^2(z)} - \frac{d_y^2}{2\sigma_y^2(z)} - \frac{(2z - z_0)^2}{2\sigma_z^2}\right] \tag{B.11}$$

At high energy, the relativistic factor of Equation B.1 for two colliding bunches is very nearly equal to 2, since $\mid \vec{\beta}_1 - \vec{\beta}_2 \mid \simeq 2$ and $\mid \vec{\beta}_1 \times \vec{\beta}_2 \mid \simeq 0$. Thus the luminosity per bunch crossing is given by

$$\mathcal{L} = \frac{N_1 N_2}{(2\pi)^{3/2}\sigma_z\, c} \int_{-\infty}^{\infty} dz \frac{1}{\sigma_x(z)\,\sigma_y(z)} \exp\left[-\frac{d_x^2}{2\sigma_x^2(z)} - \frac{d_y^2}{2\sigma_y^2(z)} - \frac{(2z - z_0)^2}{2\sigma_z^2}\right], \tag{B.12}$$

where only one numerical integration remains.

By making an assumption that the transverse beam size is independent of z, the above expression for the luminosity is analytically expressed as

$$\mathcal{L}(\sigma \neq \sigma(z)) = \frac{N_1 N_2}{2\pi\sigma_x\sigma_y} \exp\left[-\frac{d_x^2}{2\sigma_x^2} - \frac{d_y^2}{2\sigma_y^2}\right]. \tag{B.13}$$

If there is no beam separation and a round beam assumption is made such that $\sigma_{1x} = \sigma_{2x} = \sigma_{1y} = \sigma_{2y} = \sigma$, the familiar expression for the luminosity is obtained:

$$\mathcal{L} = \frac{N_1 N_2}{4\pi\sigma^2}. \tag{B.14}$$

If a crossing angle is present, the transverse separation d is replaced by

$$d_i = d_{i_0} + 2z \tan\frac{\alpha_i}{2}, \tag{B.15}$$

where the subscript $i \equiv x, y$ denotes a transverse plane. The existence of a beam separation is included in the term d_0. The crossing angle α is the full crossing angle as depicted in Figure B.1. Upon substituting the above expression into Equation B.12 and making the assumption that transverse sigma are independent of z, one obtains a luminosity expression

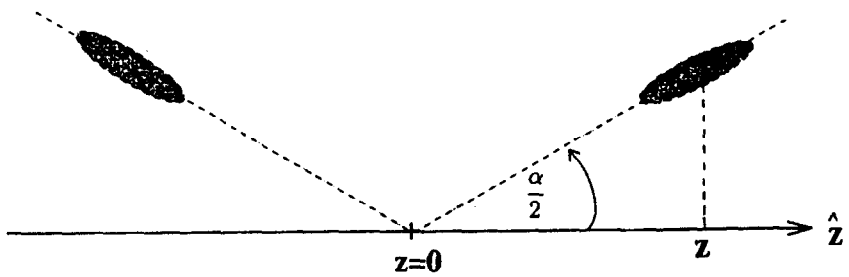

Figure B.1: A schematic of two bunches colliding with a full crossing angle α.

dependent upon a crossing angle. For a crossing angle in the horizontal plane, the luminosity is

$$\mathcal{L} = \frac{N_1 N_2}{2\pi\sigma_y\sigma_{xz}}, \tag{B.16}$$

where $\sigma_{xz} = \sqrt{\sigma_x^2 + \sigma_z^2 \tan^2\frac{\alpha_x}{2}}$. This expression assumes that $d_0 = 0$ in both transverse planes and that $z_0 = 0$. If a round beam is assumed, the familiar dependence of luminosity on a crossing angle in one dimension is obtained:

$$\mathcal{L} = \frac{N_1 N_2}{2\pi\sigma_i^2\sqrt{1 + \frac{\sigma_z^2}{\sigma_i^2}\tan^2\frac{\alpha_i}{2}}}, \tag{B.17}$$

where the subscript $i \equiv x, y$ denotes a given transverse plane.[15]

Appendix C

A Historical Review of the Use of Electrostatic Separators in Colliders [1]

Coinciding with efforts to reduce observed luminosity limitations, electrostatic separators were used at a very early stage in the development of colliders.

Beam-beam interaction effects were observed to be a luminosity limitation in the VEPP-2 electron-positron collider in Novosibirsk in 1965. "Effects of electromagnetic interaction between colliding beams ('Beam-beam phenomena') seem to place rather principle restrictions on the achievable luminosity."[69] Beam-beam luminosity limitations seem to have led quite naturally to an implementation of electrostatic separators in colliders in order to separate particles of opposite charge in the same storage ring and decrease beam-beam interaction effects.

There were several early uses of electrostatic separators in a variety of storage rings. The VEPP-2 storage ring was colliding electrons and positrons in 1967 at a center-of-mass energy of 400 MeV. An "orbit splitting" technique with the help of an electric field was used at that time. Beam separation enabled stored electrons to reach currents of 100 mA without large positron losses.[1] Two years later, the Orsay collaboration in France was also faced with a beam-beam luminosity limitation in the ACO electron-positron collider. A current limit of 20 mA per bunch existed for two colliding bunches at a center of mass energy of 1070 MeV. In order to "fight the effect", electrostatic separation was used.[70] The collider at Laboratori Nazionali di Frascati (ADONE), colliding electrons and positrons at a center-of-mass energy of 3.0 GeV, used separators for beam stability at injection.[71]

[1] This appendix is not part of the dissertation submitted to the University of New Mexico. It is included only in the Fermilab internal note.

The Cambridge Electron Facility (CEA) extended the use of separators for multibunch operation.[72] Electron and positron bunches were accelerated in the CEA in 1969 to energies of approximately 4 GeV. The bunches filled approximately one-third of the synchrotron. Vertical separation was used to separate bunches at parasitic crossing points.[73] "Physical separation with electrostatic fields....is necessary to avoid short lifetimes of the weaker of the two beams due to the incoherent space charge interaction."[74] Separated orbits of the electrons and positrons in the storage ring were kicked onto the same closed orbit in the bypass interaction region and collided head-on at the interaction region.[75]

Electrostatic separators continued to be utilized as higher energy electron-positron colliders were constructed, such as the 6.0 GeV (center-of-mass) SPEAR electron-positron collider at Stanford Linear Accelerator Complex (SLAC).[76]

A major technical difficulty in operation of electrostatic separators is in maintaining a spark rate of zero. One spark often proves disasterous for a colliding beam store. The first electrostatic separators operated at voltages of approximately 10 kV/cm. As particles were accelerated to higher energies, voltage requirements on electrostatic separators increased to approximately 50 kV/cm. These high voltage separators were built almost simultaneously and independantly for the SPS proton-antiproton collider at CERN and for the CESR electron-positron collider at Cornell University. Both accelerator collaborations presented experimental results on their newly deviced "pretzel orbit schemes" at the 1985 IEEE Particle Accelerator Conference (Vancouver) with no reference to each other![77],[78] CESR began using electrostatic separators in the horizontal plane to allow for multi-bunch operation and raise the luminosity.[79] The SPS implemented a horizontal orbit separation in order to decrease the beam-beam tune shift of the antiprotons and accomodate collisions of six antiproton and six proton bunches.[80]

Electrostatic separators remain an integral part of many high-energy colliders which were constructed in recent years. The Tevatron Collider at Fermilab collides protons and antiprotons at a center of mass energy of 1800 GeV. The Collider had reached a luminosity limit due to the beam-beam interaction in its first Collider Run in 1988. One could not increase the luminosity by decreasing the transverse size of the proton bunch or by increasing the number of protons per bunch. In fact, it was necessary to dilute phase space density of the protons in order to maintain stability of the antiprotons.[81] Taking advantage of the equal transverse size of the bunch distributions (round beams), the Tevatron implemented a helical orbit scheme by separating the orbits of the protons and antiprotons in both the horizontal and vertical planes. The opposing particle distributions are separated everywhere

in the ring except at the locations of the two high energy physics detectors.[82] The achievable luminosity of $1.6 \times 10^{30}\text{cm}^{-2}\text{sec}^{-1}$ without beam separation increased to luminosities of $5.4 \times 10^{30}\text{cm}^{-2}\text{sec}^{-1}$ in routine operations with helical orbits in the following Collider Run.[3]

In CERN's electron-positron collider at LEP, consideration of different operational configurations of electrostatic separators has continually led to increases in the luminosity. In 1990, the LEP ring began to collide four bunches of electrons and positrons at a center-of-mass energy of 90 GeV at four high energy physics detector locations. Vertical separators were used to separate the beam at the four parasitic locations in the accelerating ring. Following the multi-bunch scheme developed at CESR, more separators were installed at LEP and more bunches were accelerated (up to eight) shortly afterwards.[83],[84] To further increase the luminosity, a recent proposal for a "bunch-train" scheme has been approved which consists of accelerating four equidistant trains of bunches in each beam instead of four to eight single bunches.[85] Previous problems with sparking of electrostatic separators in LEP have been essentially eliminated by always operating one electrostatic plate at ground potential and the other at positive potential.[86]

Plans for future accelerators continue to include electrostatic separators as a tool in avoiding luminosity limitations due to the beam-beam interaction. Recent studies of expected beam-beam effects in CERN's Large Hadron Collider (LHC) have determined that the main limit to the luminosity will be the beam-beam effect.[87] Planned operation with closely spaced bunches in an interaction region add another level of complexity to beam-beam luminosity limitations as long-range beam-beam effects become much more significant.[88]

Bibliography

[1] V.L.Auslander, et.al., *Experimental Investigations of Beam-Beam Interaction in Storage Rings*, Proceedings of the 6th International Conference on Particle Accelerators, pp. 126-129, (1967).

[2] Dugan, G. *Tevatron Status*, Proceedings of the 1989 IEEE Particle Accelerator Conference, pp. 427-428, (1989).

[3] Private communication with Steve Holmes, Fermilab, August (1994).

[4] E.D. Courant and H.S. Snyder, *Theory of the Alternate Gradient Synchrotron*, Annals of Physics, Vol. 3, pp. 1-48, (1958).

[5] Fermi National Accelerator Laboratory, *Design Report - Tevatron 1 Project*, September (1984).

[6] F.T.Cole and R. Donaldson, *Proceedings of the 12th International Conference on High Energy Accelerators*, Fermilab National Accelerator Laboratory, August (1983).

[7] F.T.Cole, R. Donaldson et. al., *A Report on the Design of the Fermi National Accelerator Laboratory Superconducting Accelerator* ,Fermilab National Accelerator Laboratory, May (1979).

[8] G. Floquet, Ann. Ecole Normale (2) 12 (1883) 47.

[9] D.A.Edwards and M.J.Syphers, *An Introduction to the Physics of High Energy Accelerators*, Wiley Series in Beam Physics and Accelerator Technology, (1993).

[10] S. Holmes, *A Practical Guide to Modern High Energy Accelerators*, Fermilab-Conf-87/160, October (1987).

[11] E. Wilson, *Transverse Beam Dynamics*, Proceedings of the CERN Accelerator School in General Accelerator Physics, CERN 85-19, pp. 64-95, (1984).

[12] E. Wilson, *Proton Synchrotron Accelerator Theory*, CERN 77-07, March (1984).

[13] W.G. Clark, *Introduction to Magnetic Resonance and its Application to Dipole Magnet Testing*, CERN Accelerator School on Magnetic Measurement and Misalignment, March (1992).

[14] Satogata, T. *Nonlinear Resonance Islands and Modulational Effects in a Proton Synchrotron*, Dissertation, Northwestern University (1993).

[15] Sands, M. *The Physics of Electron Storage Rings: An Introduction*, SLAC-121, November (1970).

[16] Ohnuma, S. *The Beam Emittance*, EXP-111, November (1983).

[17] Based on calculations done by Norman Gelfand, Fermilab, February (1993).

[18] Calculations were based on a Tevatron model *Tevconfig* developed by Glenn Goderre, Fermilab.

[19] Calculations and plots done by Glenn Goderre, Fermilab, October (1994).

[20] Private communication with Glenn Goderre, Fermilab, October (1994).

[21] L. Michelotti, *Intermediate Classical Dynamics*, John-Wiley Press, (1995).

[22] A.W.Chao, *Nonlinear Beam-Beam Resonances*, Joint US/CERN School on Particle Accelerators, Italy, SLAC-PUB-3545, January (1985).

[23] L.R. Evans,*The Beam-Beam Interaction*, CERN SPS/83- 38 (DI-MST) (1983).

[24] S.G. Peggs and R.M. Talman, *Nonlinear Problems in Accelerator Physics*, Ann. Rev. Nucl. Part. Sci., 36, p. 287 (1986).

[25] K. Cornelius, M. Meddahi, R. Schmidt, *Experiments on the Beam-Beam effect in the CERN-SPS 1989 collider run*, SPS/AMS/Note 89-13.

[26] K. Cornelius, M. Meddahi, R. Schmidt, *The beam-beam effect in the SPS proton antiproton collider for beams with unequal emittances*, CERN SL/90-73 (AP).

[27] S. Saritepe, L. Michelotti, S. Peggs, *Long-Range Beam-Beam Interactions in the Tevatron: Comparing Simulation to Tune Shift Data*, FERMILAB-Conf-90/134.

[28] Bambade, Ph. D. thesis, *Effets faisceau-faisceau dans les anneaux de stockage e+ e- á haute énergie: grossissement résonant des dimensions verticales dans le cas de faisceaux plats.*, LAL84/21, June 1984, Universite de Paris Sud, Centre d'Orsay.

[29] Meddahi, M., Ph. D. thesis, *Effets faisceau-faisceau dans le Collisionneur Protons-Antiprotons du SPS*, CERN SL/91-30(BI), July 1991, Universite de Paris Sud, Centre d'Orsay.

[30] Goldstein, H., *Classical Mechanics*, Addison-Wesley (1980).

[31] Ruth, R., *Single Particle Dynamics and Nonlinear Resonances in a Circular Accelerator*, Lecture Notes in Physics No. 247: Proceedings of the Joint US-CERN School on Particle Accelerators, Springer-Verlag (1985).

[32] L.R. Evans and J. Gareyte,*Beam-Beam Effects*, CERN Accelerator School, Sept. 1985, CERN 87-03, Vol. I, p. 159.

[33] A.W.Chao, *Nonlinear Dynamics and the Beam-Beam Interaction*, AIP Conference Proceedings, No. 57. pg. 42-68 (1979).

[34] Herr, W., *Tune Shifts and Spreads Due to Short and Long Range Beam-Beam Interactions in the LHC*, CERN SL/90-06, March (1990).

[35] Herr, W., *Tracking studies on the beam-beam effect in the Cern - SPS p pbar Collider*, CERN SL/91-05 (AP), September (1991).

[36] Private communication with Werner Herr, CERN, October (1994).

[37] Myers, S., *Nonlinear Dynamics Aspects of Particle Accelerators*, Lecture Notes in Physics No. 247: Proceedings of the Joint US-CERN School on Particle Accelerators, Springer-Verlag (1985), pp. 176-237.

[38] Bassetti, M. and Erskine, G., CERN ISR-TH/80-06, March (1980).

[39] Y. Okamoto and R. Talman, *Rational Approximation of the Complex Error Function and the Electric Field of a Two-Dimensional Gaussian Charge Distribution*, CBN80-13, September (1980).

[40] S. Saritepe, G. Goderre, S. Peggs, *Observations of the Beam-Beam Interaction in Hadron Colliders*, FERMILAB-FN-573 (1991).

[41] S. Peggs, *Hamiltonian Theory of the E778 Nonlinear Dynamics Experiment*, SSC-175, April (1988).

[42] S. Peggs, *Iteration and Accelerator Dynamics*, SSC-144, October 1987.

[43] S. Peggs, *Hadron Collider Behaviour in the Nonlinear Numerical Model EVOL*, Particle Accelerators, Vol. 17, p:11-50 (1987).

[44] Private communication with Werner Herr, CERN, February (1995).

[45] R. Siemann, *Summary of Measurements of Betatron Line Amplitudes, RF Phase Noise and Emittance Growth*, Fermilab Internal Experimental Note, EXP-155, August (1987).

[46] D. Boussard, *Schottky Noise and Beam Transfer Diagnostics*, Proceedings of the CERN Accelerator School for General Accelerator Physics, CERN 87-03 (1987).

[47] G. Jackson, *Tune Spectra in the Tevatron Collider*, Proceedings of the IEEE Particle Accelerator Conference, pp. 860-862 (1989).

[48] D. Martin, et al, *A Resonant Beam Detector for Tevatron Tune Monitoring*, Proceedings of the IEEE Particle Accelerator Conference, pp. 1486-1488 (1989).

[49] Figures 4.2 and 4.3 contributed by Milciades Contreras, University of Chicago collaboration at CDF.

[50] C. Grosso-Pilcher and S. White, *CDF Luminosity Calibration*, Fermilab Note FN-550, October (1990).

[51] P. Michals, *Precision in SBD Measurement*, Fermilab Internal Experimental Note, Fermilab Note, EXP-163, March (1989).

[52] Measurement and plot done by E. Barsotti, Fermilab, October (1994).

[53] E. Barsotti, *The Sampled Bunch Display (SBD) Upgrade*, Fermilab Operations Bulletin, no. 1257, March (1994).

[54] Private communication with Ed Barsotti, Fermilab, July (1994).

[55] J. Gannon, et al, *Flying Wires at Fermilab*, Proceedings of the IEEE Particle Accelerator Conference, pp. 68-70 (1989).

[56] J. Zagel, et al, *Upgrades to the Fermilab Flying Wire Systems*, Proceedings of the IEEE Particle Accelerator Conference, pp. 1174-1176 (1991).

[57] Private communication with Glenn Goderre, Fermilab, February (1995).

[58] Private communication with Greg Vogel, Fermilab, July (1994).

[59] W.C. Carithers et al, *The CDF SVX: A Silicon Vertex Detector for a Hadron Collider*, Nuclear Instruments and Methods in Physics Research A289, pp. 388-399 (1990).

[60] Private communication with Mike Martens, Fermilab, March (1995).

[61] R. Dubois, et al, *Beam Separation Experiments at the SPS Collider*, CERN SPS/85-5, January (1985).

[62] S. van der Meer, *Calibration of the Effective Beam Height in the ISR*, ISR-PO/68-31, June (1968).

[63] M. Month, *Collider Performance with Ideal Collisions*, Internal Fermilab D0 Note 201, (1985).

[64] Calculations and plots using SVX data were done by Paul Derwent, University of Michigan collaboration at CDF, December (1994).

[65] Private communication with R. Schmidt, K. Cornelius, M. Meddahi and W. Herr of CERN, February (1994).

[66] S. Ohnuma, *The Beam and the Bucket*, Fermilab Internal Note TM-1381, (1986).

[67] B. Hanna, *Turning on the Separators*, Fermilab Operations Bulletin 1207, November (1990).

[68] H. Grote and C. Iselin, *The MAD Program*, CERN/SL/90-13, rev. 3, January (1993).

[69] V.L. Auslander, et.al., *Experimental Results on Beam-beam Interaction*, Proceedings of the 5th International Conference on Particle Accelerators, pp. 335-339, (1965).

[70] J.E. Augustin, et. al., *Development and Beam Studies on ACO*, Proceedings of the 7th International Conference on Particle Accelerators, pp. 19-24, (1969).

[71] F. Amman, et. al., *Single and Two Beam Operation in Adone*, Proceedings of the 7th International Conference on Particle Accelerators, pp. 9-18, (1969).

[72] A. Hofmann, et. al., *The Colliding Beam Project at the Cambridge Electron Accelerator*, Proc. of the Sixth International Conference on High Energy Accelelerators, pp. 113-118, (1967).

[73] T. Dickinson, *Electrostatic Separation of Stored Beams at CEA*, IEEE Transactions on Nuclear Science, pp. 196-198, (1971).

[74] R. Averill, et. al., *Colliding Electron and Positron Beams in the CEA Bypass*, Proc. of the Eighth International Conference on High-Energy Accelerators, pp. 140-144, (1971).

[75] C. Mieras and G.A. Voss, *A Design of the CEA Colliding Beam Bypass*, Proc. of the Sixth International Conference on High Energy Accelelerators, pp. 119-122, (1967).

[76] B. Richter, *Colliding Beams: Present Status; and the SLAC Project*, IEEE Transactions on Nuclear Science, Vol. NS-18, No. 3, pp. 193-195, June (1971).

[77] R. Littauer, *Multibunch Operation of CESR*, Proceedings of the IEEE Transactions on Nuclear SCience, Vol. NS-32, No. 5, pp 1610-1613, October (1985).

[78] L. Evans, et.al., *Beam Separation at the CERN SPS Collider*, Proceedings of the IEEE Transactions on Nuclear SCience, Vol. NS-32, No. 5, pp 2209-2211, October (1985).

[79] S. Herb, CESR: Projects and Prospects, Proceedings of the 13th International Conference On High Energy Accelerators, pp. 58-62, August (1986).

[80] K. Cornelis, *Beam-beam Effects and High Luminosity Operation in the SPS Proton Antiproton Collider*, CERN SPS/86-14, September (1994).

[81] S.D. Holmes, *The Fermilab Upgrade*, Proceedings of the IEEE Particle Accelerator Conference, pp. 436-438, March (1989).

[82] G. Annala, *Operational Experience with the Tevatron Collider using Separated Orbits*, Proceedings of the IEEE Particle Accelerator Conference, pp. 3808-3810, May (1993).

[83] J.M. Jowett, *More Bunches in LEP*, CERN LEP-TH/89-17, Proceedings of the IEEE Particle Accelerator Conference (Chicago, IL), p.1806, March (1989).

[84] Cern Courier: International Journal of High Energy Physics, *The Best of the Bunch*, Edited by G. Frasier, pp. 18-20, October (1992).

[85] C. Bovet, et.al., *Final Report of the 1994 Bunch Train Study Group*, CERN SL/94-95-(AP), December (1994).

[86] E. Keil, *Review of High Energy e^+e^- Colliders*, Proceedings of the European Particle Accelerator Conference EPAC92 (Berlin, Germany), pg. 22-26, March (1992).

[87] W. Herr, *Beam-beam Effects in the LHC*, CERN SL/94-92-(AP), November (1994).

[88] W. Herr, *Tune Shifts and Spreads due to Long Range Beam-beam Effects in the LHC*, CERN SL/90-06-(AP), March (1990).